ELENA MORA SERRANO | Applicability of a Dynamic Recrystallization Model for an Open Die Forging Process for the As-Cast Superaustenitic Stainless Steel Alloy 28

Mondragon
Unibertsitatea

DOCTORAL THESIS

APPLICABILITY OF A DYNAMIC RECRYSTALLIZATION MODEL FOR AN OPEN DIE FORGING PROCESS FOR THE AS-CAST SUPERAUSTENITIC STAINLESS STEEL ALLOY 28

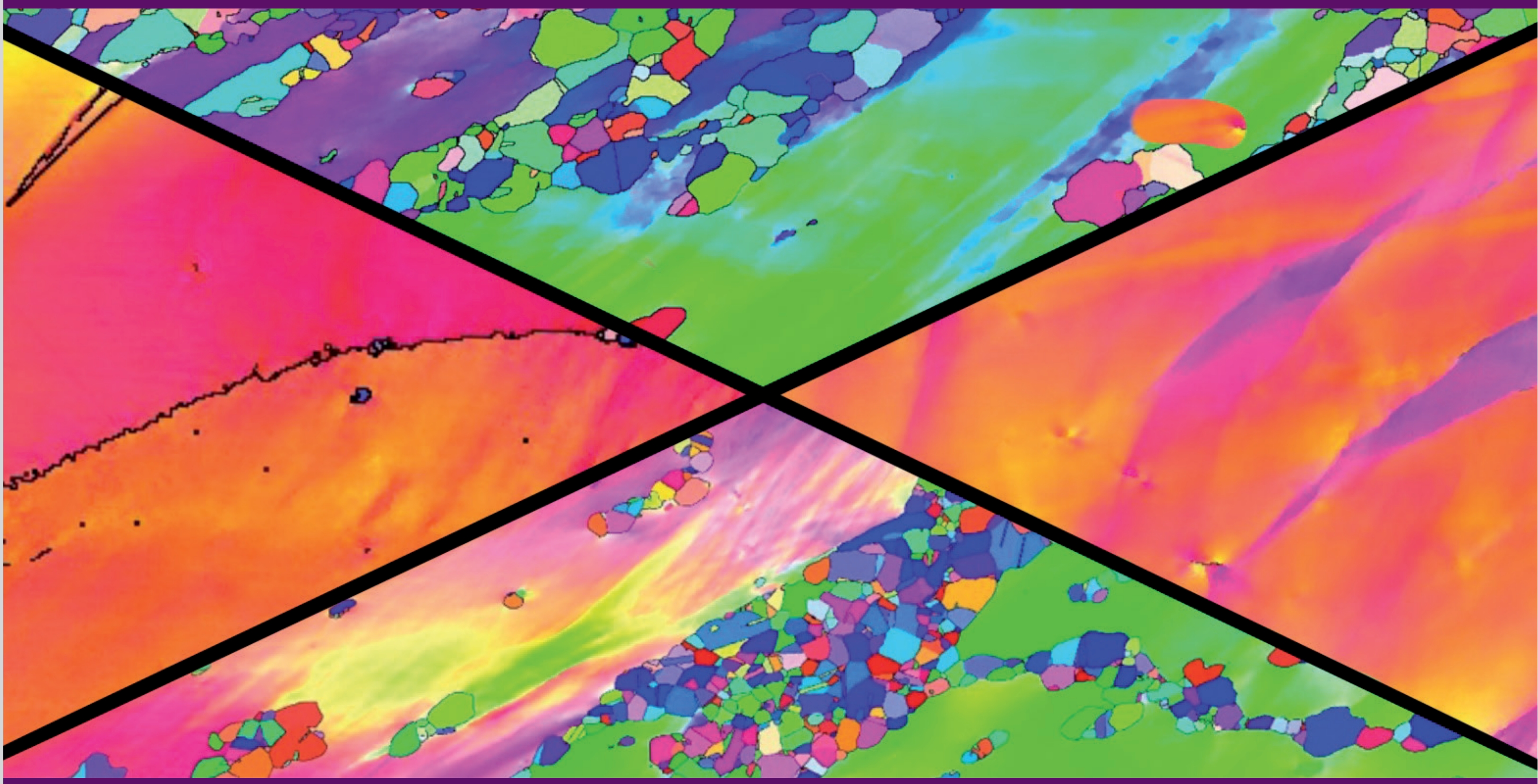

ELENA MORA SERRANO | **Arrasate-Mondragón, 2022**

Mondragon
Unibertsitatea
Goi Eskola
Politeknikoa
Faculty of
Engineering

Applicability of a Dynamic Recrystallization Model for an open die forging process for the As-Cast Superaustenitic Stainless Steel Alloy 28

- Elena Mora Serrano-

Supervised by:

Dr Joseba Mendiguren
Mondragon Goi Eskola Politeknikoa
Mechanical and Manufacturing Department

Dr Iñaki Hurtado
Mondragon Goi Eskola Politeknikoa
Mechanical and Manufacturing Department

Thesis presented at
Mondragon Goi Eskola Politeknikoa
Mechanical and Manufacturing Department

February 3st, 2022

DEDICATORIA

Me gustaría dedicar este pequeño espacio a toda la gente gracias a la cual he conseguido llegar hasta aquí, gente que ha pasado y me ha ayudado en una u otra parte del camino, gracias.

A mis padres que me han apoyado incondicionalmente hasta cuando les dije que me iba a pleno Euskadi a hacer mi tesis y a mi hermano, que no llevo a cabo los planes de renovación de mi cuarto cuando me fui y a mi abuela que siempre me echa de menos y hemos hecho nuestros viajes al revés, ella de norte a sur y yo de sur a norte. A toda mi familia, por estar ahí y sentiros orgullosos.

A mis incondicionales pradopinilleros, Marta y Alicia que no se que haría sin vosotras, Jorge, Hector, Mario, Koki e Isabel sufidores también de tesis, y todos los que haceis esos veranos y la vida un poquito más fácil.

A Maqueda por ser mi referente y animadora, por ponerme siempre de vuelta al camino cuando parece que me pierdo como la medio mele de la vida que eres. A Yanaisa por sus visitas y llamadas de animo y a Materia por nuestras charlas. A todas mis Jabatas porque sois de donde vengo.

A mi Komando, mi familia Eibarresa fuera de casa que me acogisteis enseguida y me ayudasteis a gestionar la vida, a Tximeno, Malen, Mery, Edurne, Lu, Soni, Jone, Iur y nuestra amatxu Eli por cuidar de mi, eskerrik asko. A Patri, que fuiste una parte muy importante de que me gustara todo esto. A Mikel, por enseñarme una gran lección: “Nunca hay que perder la maravillosa libertad de equivocarse”.

A Ana, mi becaria favorita por animarme las tardes aburridas y a Erika, por nuestras charlas de EBSD. A todos mis compañeros de tesis, todos, por el grupo tan maravilloso, por aceptar a una madrileña y por estos 4 años tan geniales, Unai, Nora, Iribe, Juanjo, Asier, Raquel, Xuban, Eli, Zarketa, Mendikute, David y Ane. Especialmente a Julen, te debo muchísimo y me has ayudado increíble, estoy en deuda, eskerrik asko.

Y en este último año, una gran gran dedicatoria a ti, Jorge, que has aguantado mis agobios, me has ayudado y has estado conmigo dándome todo el apoyo que necesitaba y más, gracias.

STATEMENT OF ORIGINALITY

I hereby declare that this submission is my own work, and to the best of my knowledge, it contains no previously published material or written by another person neither substantial proportions accepted to earn any other degree of diploma at Mondragon Goi Eskola Politeknikoa or any other educational institution, except where acknowledgement is done.

ACKNOWLEDGEMENTS

I would like to thank some people and institutions in the following lines because this thesis would not have been possible without them.

To Joseba Mendiguren and Iñaki Hurtado, to give me the opportunity and the trust to be part of this project and work in a field that I love, and the support they give me along the journey. Also, a big thank you to the Mechanical and Industrial production department, which is pleased to work in it.

A special mention to the workers on the workhouse, Gotzon, Arkaitz, Iñaki to help me with the materials, and Ainara, Wilson, Erika and Laraitz for their work and help in the elaboratory, especially with the EBSD, and to Joseba. Peio and Ana for also lent me a hand from time to time.

To all my fellow PhD students because without them, I would not have been able to achieve this goal, thank you for the welcome, for making me feel at home and for all the support: Julen, Unai, David, Nora, Ane, Zarketa, Eli, Xuban, Asier, Iribe, Dani, Juanjo, Julen and all those came new and left.

To Tubacex to be the partner of this project, providing us the material, and a huge thank you to Aitor, who had helped when I needed it and from whom I learned a lot. Also, big thanks to Raquel, Alejandra, Asier, Pilar, Victoria and Beatriz, that have helped me a lot.

To Proff. Cecilia Poletti, for allowing me to work with her at the IMAT at TU Graz for her guidance in the field. Thank Ricardo and his help on some EBSD issues and everybody who made those two months (+1) really enjoyable.

ABSTRACT

In the petrochemical industry, extreme conditions require materials that can withstand high fatigue pressures and highly corrosive environments. In the last decade, the use of super austenitic steels (SASS) has increased due to their excellent properties in these environments. Alloy 28 high nickel super austenitic steel has a resistance to corrosion and high fatigue cycles, becoming one of the main options for manufacturing pipes for the petrochemical industry.

SASS has a purely austenitic structure due to its high nickel content, an alloy that gives the material high toughness and good forging behaviour. However, it also makes it susceptible to variations in the process factors, and controlling these conditions is essential. One of the most critical parameters determining a material's mechanical behaviour is the microstructure, so it is crucial to predict it.

Simulation software is used to reproduce the manufacturing process and obtain the mechanical properties to predict the state of the material. Therefore, it is necessary to determine a mathematical model that predicts the material's behaviour and calculates the material parameters for a specific model.

In this project, the microstructural evolution of Alloy 28 has been studied for an open die forging process. Furthermore, the file will be used to reproduce, through the FORGE® forming process analysis software, the industrial process of obtaining forged round bars from TUBACEX, manufacturer of pipes for Oil & Oil&Gas applications.

An exhaustive bibliographic search was carried out to understand and identify all the phenomena that occur during the transformation of the material subjected to hot deformation and how they can be studied at a laboratory scale. Furthermore, the conditions that perform hot compression tests were determined, and the results of the stress-strain curves and microstructures obtained after deformation were analysed. Finally, the model's parameters to be implemented in the simulation are determined with the results obtained.

Finally, the model obtained during this study is validated by comparing it with the one used by the manufacturer. Although this reference model is industrially validated, it does not precisely consider the physical phenomena involved in a hot process, allowing a more accurate material model.

RESUMEN

En la industria petroquímica, las condiciones extremas precisan de materiales que soporten altas presiones fatiga y la exposición a ambientes altamente corrosivos. En las últimas décadas, el uso de aceros super austenícos (SASS) se ha incrementado debido a sus excelentes propiedades frente a estos ambientes. El Alloy 28 acero superaustenítico de alto niquel, presenta una resistencia a la corrosión y a altos ciclos a fatiga, que lo convierte en una de las principales opciones para la fabricación de tuberías para la industria petroquímica.

Este tipo de aceros, presentan una estructura puramente austenítica debido a su alto contenido en niquel, un aleante que otorga al material de alta tenacidad y buen comportamiento en forja. Sin embargo, también lo hace susceptible a las variaciones que ocurren en los factores del proceso durante el mismo y controlar estas condiciones es esencial. Una de las propiedades más importantes a la hora de determinar el comportamiento mecanico del material es la microestructura del mismo y controlar la su durante el proceso será de suma importancia para optimizar el mismo.

Para predecir el estado del material, se recurre a los software de simulación que permiten reproducir el proceso de fabricación.y obtener las propiedades del material final. Para ello, es necesario determinar un modelo matemático que permita predecir el comportamiento del mismo, y calcular los parámetros del material para un modelo concreto.

En este proyecto, se ha realizado el estudio de la evolución microestructural del acero superaustenitico Alloy 28, para un proceso de forja abierta partiendo del material fundido con el objetivo de obtener el modelo fenomenológico del mismo. El archivo será utilizado para reproducir mediante el software de análisis de procesos de conformado FORGE®, el proceso real de obtención de barras redondas forjadas de TUBACEX, fabricante de tubos para aplicaciones de Oil&Gas.

Para ello, se ha estudiado el proceso real y las diferentes fases que presenta el material tras la colada y al finalizar la forja. Posteriormente se ha realizado una exhaustiva búsqueda bibliográfica para comprender e identificar todos los fenómenos que ocurren durante la transformación del material sometido a una deformación en caliente y como se pueden estudiar a escala laboratorio. Esto último ha permitido determinar las condiciones para realizar ensayos de compresión en caliente y posteriormente analizar los resultados de las curvas tensión-deformación y de las microestructuras obtenidas tras la deformación. Con los resultados obtenidos, se determinan los parámetros del modelo que será implementado en la simulación.

Finalmente, se valida el modelo obtenido durante este estudio comparándolo con el empleado por el fabricant. Si bien este modelo de referencia es validado industrialmente, no tiene en cuenta de manera precisa los fenómenos físicos implicados en un proceso en caliente, lo que permitirá obtener un modelo de material más precisa.

LABURPENA

Industria petrokimikoan, muturreko baldintzak direla-eta neke presio handiak eta giro oso korrosiboekiko esposizioa jasaten dituzten materialak behar dira. Azken hamarkadetan, altzairu super austenikoen (SASS) erabilera handitu egin da, ingurune horiei aurre egiteko propietate bikainak dituztelako. Alloy 28 nikel maila handiko altzairu superaustenitikoak korrosioarekiko eta neke ziklo handiekiko erresistentzia handia du, eta horrek egiten du industria petrokimikorako hodiak fabrikatzeko aukera nagusietako bat izatea.

Altzairu mota horiek egitura austenitiko hutsa dute, nikel asko baitute, eta aleatzaile horri esker materialak zailtasun handia du, eta forjan portaera ona. Hala ere, prozesuan zehar prozesuaren faktoreetan gertatzen diren aldaketekiko oso sentikorra da, eta baldintza horiek kontrolatzea funtsezkoa da. Materialaren mikroegitura da materialaren portaera mekanikoa zehazteko propietate garrantzitsuenetako bat, eta prozesuan zehar mikroegitura kontrolatzea oso garrantzitsua izango da materiala optimizatzeko.

Materialaren egoera aurreikusteko, fabrikazio prozesua erreproduzitzeko eta azken materialaren propietateak lortzeko simulazio softwareetara jotzen da. Horretarako, eredu matematiko bat zehaztu behar da, haren portaera aurreikusteko, eta eredu jakin baterako materialaren parametroak kalkulatu behar dira.

Proiektu honetan, Alloy 28 altzairu superaustenitikoaren bilakaera mikroestrukturalaren azterketa egin da, forjaketa irekiko prozesu baterako, galdatutako materialetik abiatuta, horren eredu fenomenologikoa lortzeko helburuarekin. Artxiboa FORGE® konformazio prozesuak aztertzeko softwarearen bidez erreproduzitzeko erabiliko da, Oil&Gas aplikazioetarako hodien fabrikatzailea den TUBACEX enpresaren barra biribil forjatuak lortzeko benetako prozesua erreproduzitzeko.

Horretarako, benetako prozesua eta materialak galdaren ondoren eta forja amaitzean dituen faseak aztertu dira. Ondoren, bilaketa bibliografiko sakon bat egin da beroan deformatutako materialaren eraldaketan gertatzen diren fenomeno guztiak ulertzeko eta identifikatzeko, eta laborategi eskalan aztertzeko moduak identifikatzeko. Azken horri esker, beroko konpresio saiakuntzak egiteko baldintzak zehaztu ahal izan dira, eta, ondoren, tentsio-deformazio kurben eta deformazioaren ondoren lortutako mikroegituren emaitzak aztertu ahal izan dira. Lortutako emaitzekin, simulazioan ezarriko den ereduaren parametroak zehazten dira.

Azkenik, azterlan honetan lortutako eredua baliozkotu da, fabrikatzaileak erabilitakoarekin alderatuta. Erreferentziako eredu hori industrialki baliozkotzen bada ere, ez ditu zehatz-mehatz kontuan hartzen beroko prozesu batean inplikatutako fenomeno fisikoak, eta, horri esker, material eredu zehatzagoa lortu ahal izango da.

ABREVIATIONS

SASS	Super austenitic Stainless Steel
LSFE	Low Stacking Fault Energy
HSFE	High Stacking Fault Energy
SIBM	Strain-Induced Boundary Migration
TPS	Thin Plane Spline
LAB	Low Angle Bouy
HAB	High Angle Boundary
WH	Work Hardening
DRX	Dynamic Recrystallization
DT	Dynamic Transformation
DRV	Dynamic Recovery
SRX	Static Recrystallizaiton
SRV	Static Recovery
PDRX	Post-Dynamic Recrystallization
MDRX	Metadynamic Recrystallization
cDRX	continuous Dynamic Recrystallization
dDRX	discontinuous Dynamic Recrystallization
GG	Grain Growth
FCC	Face Centered Cubic
FEM	Finite Element Method
SEM	Scanning Electron Microscope
EBSD	Electron Backscatter Diffraction
GOS	Grain Orientation Spread
OM	Optical Microscope
P-J	Poliak and Jonas method
SDC	Second Derivative Criterium
JC	Johnson-Cook Model
FB	Fields-Backofen model
ANN	Artificial Neural Network
H-S	Hansel-Spittel Model
JMAK	Johnson-Mehl-Avrami-Kolmogorov kinetic model

CONTENT LIST

FIGURE LIST

TABLE LIST

1. INTRODUCTION

The premature exhaustion of many conventional in earth petroleum fields is a direct consequence of population growth, the significant development of the industrial sector, and the unleashed in the last decades of several wars at global scales. Thus, the necessity to discover new oilfields and the high price of the oil barrel is the fundamental motivations for big companies to adventure in the search for hydrocarbons in the ocean.

The exploitation of new offshore petroleum fields has brought new technological challenges to the scientific society to construct safe oil-extraction and transport infrastructures respectful with the marine environment.

Moreover, even if global oil production predictions show a decreasing tendency, society and research trends drive towards cleaner and more environmentally friendly energetic resources in the following decades, the world petroleum demands are still on the rise, as shown in Figure 1-1. For this instance, petroleum producers are searching for new extraction reserves in more remote locations with critical conditions, increasing the difficulty of oil extraction and transport.

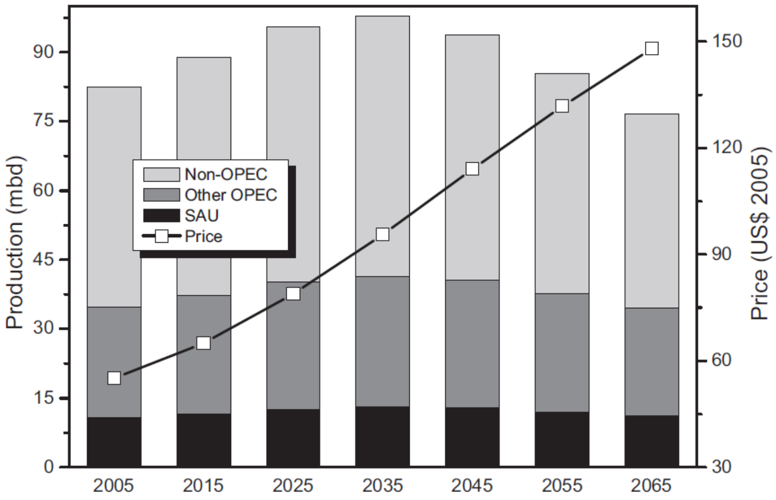

Figure 1-1. Oil production and price prediction in the following decade[1].

Therefore, oil and gas companies are developing advanced materials and technologies that provide extraordinary mechanical and corrosion properties due to extreme working conditions, such as highly corrosive environments and elevated temperatures.

Austenitic stainless steel is found in many applications due to its excellent mechanical and corrosion properties. In addition, the super austenitic grades of stainless steel, containing more than 20% nickel and a high amount of alloying elements such as Mo, provide an improved corrosion resistance associated with a high strength level [2], [3].

Alloy 28 (UNS N08028), widely used for the oil and gas industry, provides excellent anti-corrosion and mechanical properties [2]. Because the final microstructure directly influences the mechanical properties, the analysis of its evolution during forging processes and its modelling has become a critical research field for optimising the manufacturing process of oil and gas components.

1.1. Background of the project

1.1.1. The seamless tube manufacturing process

The seamless tube manufacturing process is usually divided into three main processes: Casting, Forging and Extrusion (Figure 1-2).

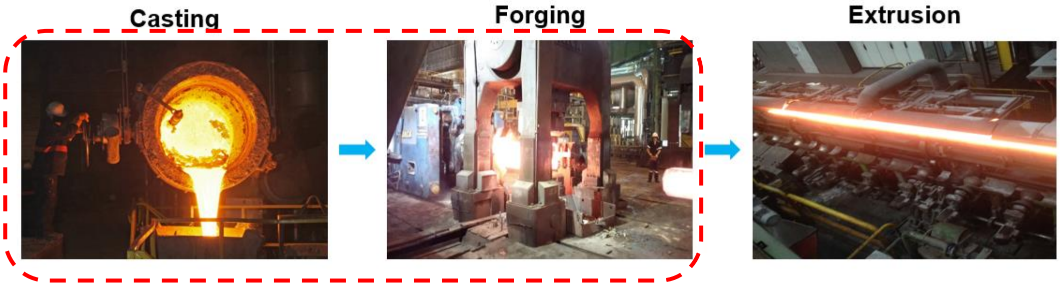

Figure 1-2. Seamless tube manufacturing process.

The as cast billet is obtained after the material is melted and cast. Next, the billet is heated to homogenise the as-cast structure and is forged on a press to refine the grain. Finally, the round bar is prepared for extrusion, and then the final tube will be obtained.

This work is focused on the casting and open die forging process (Figure 1-2), after which the round bar is manufactured. First, the studied ingot is obtained during the casting stage and is referred to as **AS CAST BILLET**. Then, the material is heat-treated and defined as **PRE-FORGED BILLET**. Then, the forging process begins, where the **SQUARE BAR** is obtained, which is heated again to carry out the forging and to obtain first the **OCTOGONAL BAR**, and finally the **ROUND BAR** (Figure 1-3).

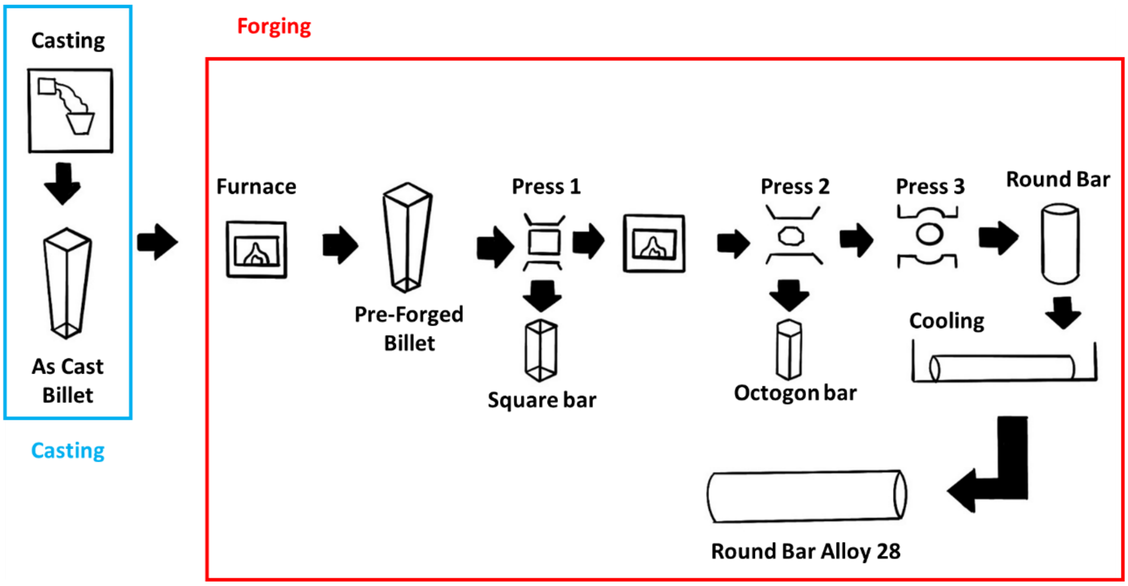

Figure 1-3. Alloy 28 seamless tube manufacturing process.

1.1.1.1. Casting process

Iron and alloying agents are melted and cast in the bottom moulds. Once the casting is finished, the billets are cooled until are removed from the moulds.

During cooling, the microstructure of the billet is usually formed as is shown in the following example Figure 1-4, where two types of grains can be distinguished: in Figure 1-4 a), columnar grains are oriented perpendicular to the longitudinal axis of the molten; on the other hand, Figure 1-4 b), equiaxial grains appear as a consequence of higher cooling time in the centre of the billet [4].

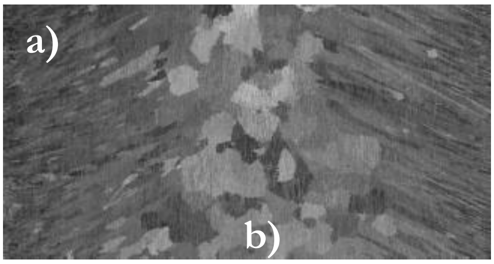

Figure 1-4: Microstructure of a homogenized alloy ingot [4].

Different variables interfered in the distribution of columnar and equiaxial grains during the solidification process, such as temperature, cooling, casting speed, and the mould's geometry. Controlling these aspects is critical to obtaining a homogeneous ingot, which will ensure a better initial microstructure distribution for the final product.

The as-cast ingot exhibit a compositional structure formed by dendrites, as is shown in Figure 1-5. In the interdendritic space, precipitates could appear, e.g. σ phase [5]. Homogenization consists of high-temperature heating used in the as cast ingot to reduce the precipitates and prepare the ingot for the forging process [4].

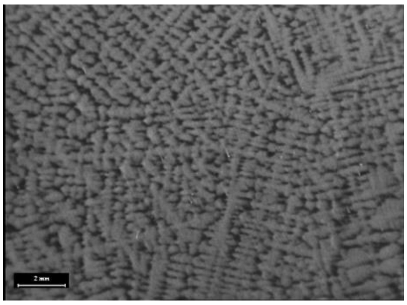

Figure 1-5: Dendrites in the as-cast Alloy 28.

1.1.1.2. The open die forging process

For the case of study, the forging method is open die forging, which allows, in one or multiple steps, to change the material section from the as cast billet to a round bar. Open-die forging is generally performed without special tooling and is usually used to cog ingots or drawdown billets from one size to a smaller one. It is employed when only a few parts are needed and when the part is too large to be produced in closed dies [6]. In Figure 1-6, the reduction of a billet by open-die forging is shown [7].

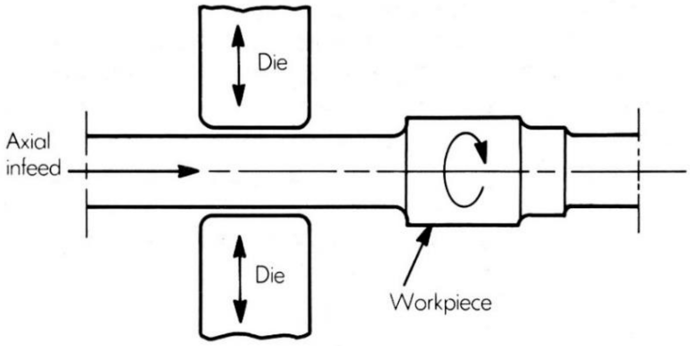

Figure 1-6: Open-die process for an ingot [7].

A manipulator performs the radial movement while the material moves through the dies in the axial direction holding the workpiece (billet) is exposed to ambient temperature during the process. As a result, the billet's surface temperatures decrease during forging while the centre remains at the working temperature. This heterogeneity in the billet's temperature directly affects the material forgeability and the final microstructure.

Forgeability is the material's capability to deform without failure and is based on metallurgical and mechanical factors [6]. The factors that affect the forgeability of material are:

- **Metallurgical factors:** Crystal structure, composition, purity, number of phases present and grain size. Materials that exhibit a face-centred cubic structure have the best forgeability. Alloys containing more than one phase are more difficult to forge than single-phase alloys. Fine-grained metals are more easily forged than coarse-grained metals due to their higher boundary mobility [6].

- **Mechanical factors:** The most significant temperature factors affecting forgeability are strain rate, temperature, and stress distribution. The strain rate is the deformation produced within a given time interval. During forging, the workpiece is exposed to compressive, shear, and tensile stresses. Ruptures are usually associated with tensile and shear stresses. Therefore, compressive support must be provided when these conditions occur [6].

1.1.2. Alloy 28

Super-austenitic stainless steels (SASS) has been widely used in high corrosive environments because of their high corrosion resistance and comprehensive mechanical properties [3], [2]. These high-performance characteristics result from a high alloy content, mainly Cr and Ni, and others such as Mn, N or Mb, which are present also in some of the widely used super austenitic steel S32654 [8] or 654 SMO [9].

Ni is considered one of the most important alloying elements in steel production. Depending on the amount of Nickel present in the alloy, different properties would appear [10]:

- Ni content until 5% provides hardenability for quenching and tempering.

- For percentages, over 8%, it provides fully austenitic structure and tough behaviour at sub-zero conditions.

- In solid solution, higher Ni and Cr percentages, up to 18 %, improve corrosion behaviour and mechanical characteristics.

A complete austenitic structure is present in SSAS due to the high Ni content (usually more than 20%). Austenite presents FCC (face-centred-cubic) crystalline structure, which provides material tenacity low stacking energy, and the recrystallized state presents polygonal grains with thermally generated twins [11]. Different operations manufacture SASS: forming, forging, extrusion, bending, machining and hot rolling [12]. Because of the high content of alloys, controlling precipitates is crucial to avoid problems such as hot cracking [8] or segregation [9] during hot working. To do so, the study of plastic deformation and microstructural development is critical to avoid these problems [12].

Super austenitic stainless steel Alloy 28 is widely used in the chemical and petrochemical industry. However, due to its higher flow stress, the high-temperature thermo-plasticity of the Alloy 28 is poor, and the corresponding hot working range is narrow [13]. The chemical composition is shown in Table 1-1 [14]:

Weight%	Ni	Fe	Cr	Mo	Cu	Ti	C	Mn	S	Si	Al
Alloy 28	30-32	22 min	26-28	3-4	0.60-1.40	-	0.02 max	2 max	0.03 max	0.70 max	-

Table 1-1: Alloy 28 chemical composition [14].

Previous works have measured the strain-stress curves under different deformation conditions to predict the behaviour of wrought Alloy 28, as is shown in Figure 1-7:

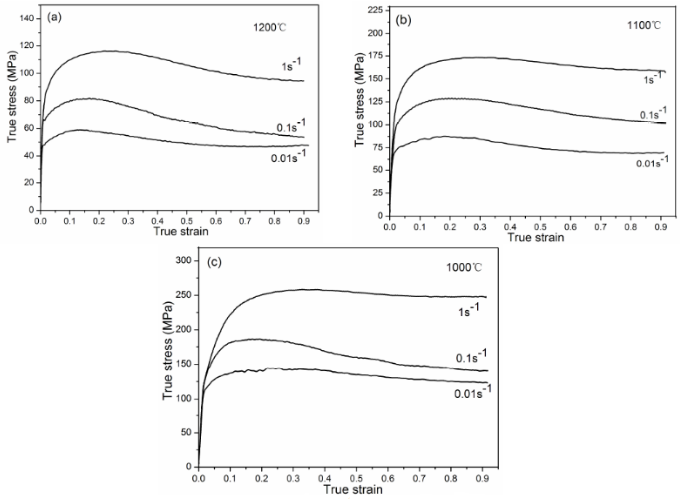

Figure 1-7: Stress-strain curves under different deformation conditions: a) T=1200 ºC; b) T=1100 ºC; c) T=1000 ºC [13].

It can be seen that the material true stress is highly dependent on temperature and strain rate. Therefore, as the strain decreases and temperature increases, the work hardening rate decrease.

1.2. Thesis outline

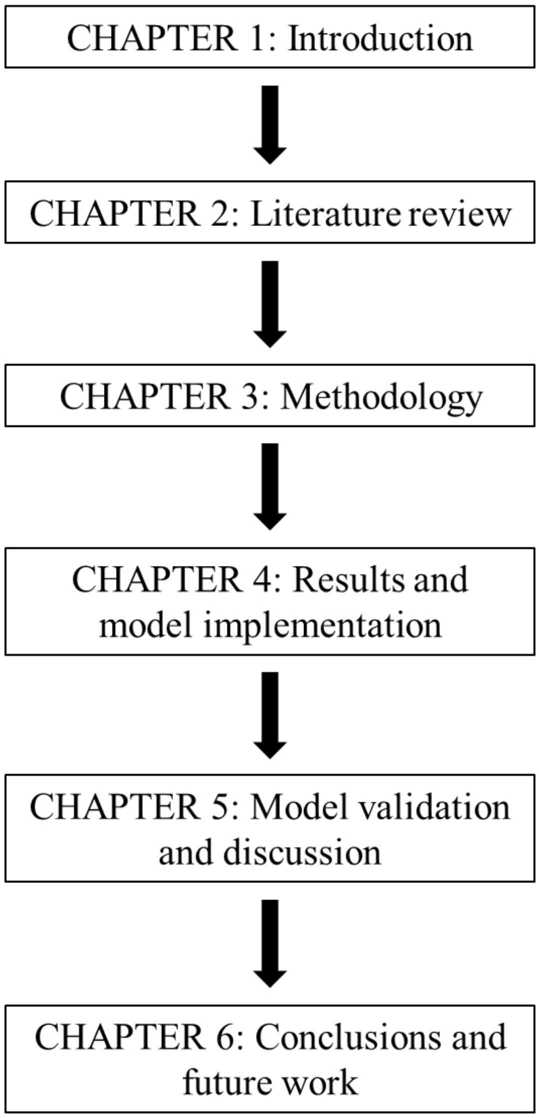

Figure 1-8. Thesis outline.

This work is focused on transformation phenomena during a multipass condition process, including work-hardening (WH) and dynamic recovery (DRV), grain boundary migration, nucleation and grain growth, which are related to dynamic recrystallization (DRX), static recrystallization (SRX) or post-dynamic recrystallization (PDRX). The material of choice is a low stacking fault energy (LSFE) material: Alloy 28, studied from As-cast state.

The thesis begins with a brief introduction (Chapter 1) on the project's background, clarifying the importance of the current oil and gas industry research and giving a brief understanding of the industrial process and the studied material.

In Chapter 2, a detailed literature review on recrystallization is presented. First, the physical transformation phenomena occurring during hot working of stainless steel is presented. Then, several recrystallization models are reviewed. After the literature presentation, a critical analysis summarized the review to clarify the model chosen for the study and the methodology followed. Finally, the focus of the thesis is presented.

Experimental methods and facilities for mechanical testing and microstructure characterization are described in Chapter 3.

In Chapter 4, the factors that impact hot deformation, such as deformation temperature, strain rate, and initial grain size on DRX, are all studied experimentally. A complete set of experimental data was collected, including DRX initialization parameters, recrystallized volume fraction and grain size for each deformation condition. The tentative value of parameters of the DRX model proposed and discussed in Chapter 2 are identified based on these experimental results.

In Chapter 5, a comparison between experimental results to validate the model is performed from the results obtained.

Finally, significant conclusions from all chapters and potential areas for further studies and future works are presented in Chapter 6.

2. LITERATURE REVIEW

In this section, bibliography sources are analysed to lay the foundations of the research understanding the mechanism present during hot working and the material evolution. A critical literature analysis is then given to define the experimental plan and the corresponding model based on previous works. Finally, the knowledge gap is set, and the focus of the thesis is presented.

2.1. Scope of the literature review

The research on recrystallization is considerable, and many aspects are not fully understood completely now at days [15]. Therefore, an extensive literature review is proposed from the classical approach to more recent ones.

Among the vast body of literature, this work is focused on transformation phenomena: WH, DRV and DRX of LSFE materials. The mechanisms of these recrystallization processes are collected, together with the influence of deformation temperature, strain rate, strain, and initial grain size.

An overview of the available numerical models of recrystallization is also presented in this chapter, focused on models of multi-pass conditions. Then, the model parameters are identified, and the corresponding experimental procedures that best fit our case are designed.

2.2. Work hardening and recovery

During hot working, controlling the microstructure is essential to predict the final properties of the material. From an industrial point of view, the final product is usually obtained, combining deformation sequences with intermediate heat treatments. The steels are deformed from casting products at high temperatures, where WH and DRV appear simultaneously in the early stages of deformation. WH is associated with generating dislocation density during the initial stages of hot working. In contrast, DRV proceeds slowly by rearrangement/realignment of generated dislocation density until the critical dislocation density is attained for triggering DRX [16].

2.2.1. Work Hardening

During a hot working process, from the initiation of deformation until DRX begins, WH takes place. The hardness acquired through WH typically needs an intermediate annealing process necessary to continue further working. This hardening behaviour makes it difficult for dislocations to move as the strain increases. The mechanical properties of metallic materials depend mainly on the dislocation content and structure, grain size and texture. The deformed state defines the subsequent microstructural evolution[17], and the kinetics of softening mechanisms are directly influenced by the Work-Hardening rate (θ) [16].

The SSAS, as Face Centered Cubic (FCC) crystals, can deform on more than one slip system. These metals usually show a solid work-hardening behaviour caused by the mutual interference of dislocations gliding on intersecting slip planes [18]. During the later stage of WH, recovery begins creating a transition between the deformation and the recrystallization state.

2.2.2. Recovery

The deformed state of a material, from which dislocation structure is formed during deformation by the glide and interaction of dislocations, is usually not in thermodynamic equilibrium. The deformed state is preserved at low temperatures after deformation because the structure is mechanically stable. However, this mechanical stability disappeared once the temperature increased and activated the process thermally.

During recovery, the stored energy decreases as a consequence of dislocation movement. Thus, there are two primary processes: the annihilation and the rearrangement of dislocations into lower-energy configurations. Glide, climb, and cross-slip dislocations achieve both processes. A schematic diagram of a crystal containing an array of edge dislocations is shown in Figure 2-1. Dislocations A and B are on the same glide plane. However, they may annihilate by gliding towards each other [19].

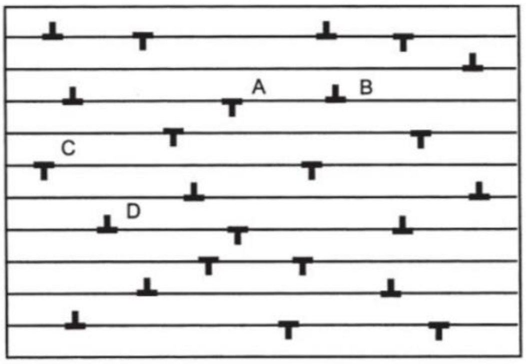

Figure 2-1. Schematic diagram of a crystal containing edge dislocations [19].

Another recovery process that decreases the lattice strain energy is the rearrangement of dislocations into cell walls. This process is illustrated schematically in Figure 2-2, whereby dislocations align themselves into walls to create small-angle or sub-grain boundaries. If a lattice region is curved during deformation (Figure 2-2 (a)), it is attributed to a sub-boundary formation annihilation and rearrangement. As is shown in Figure 2-2 (b), it can be seen that the excess dislocations remain after the annihilation process and align themselves into walls. As shown in Figure 2-3, the energy of a tilt boundary increases with increasing misorientation and vice versa. Therefore there is a driving force to form fewer, more highly misoriented boundaries as recovery proceeds [19].

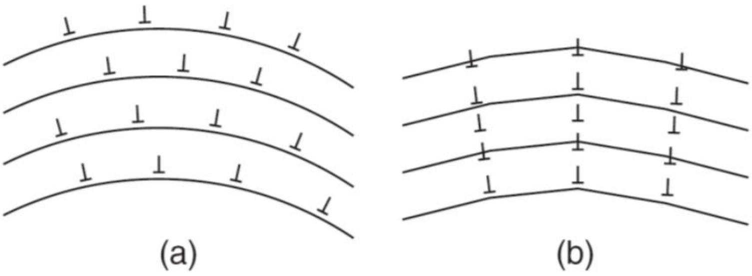

Figure 2-2. (a) Random arrangement of excess parallel edge dislocations. (b) Alignment into dislocation walls [19].

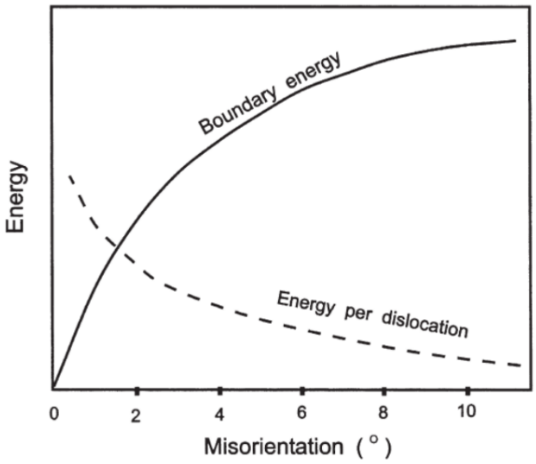

Figure 2-3. The energy of a tilt boundary and the energy per dislocation function of the crystal misorientation [19].

Recovery usually increases with strain (before recrystallization) and temperature. The stacking fault energy determines the dislocation climb and cross slip and controls the recovery rate. In metals with low stacking fault energy (Alloy 28), climbing is complex, and slight dislocation structure recovery typically occurs prior to recrystallization. In consequence, well-developed subgrain structures are not usually observed in these materials. This recovery is referred to as Dynamic Recovery.

DRV occurs during the early stages of deformation at elevated temperatures. The mechanism of climb and cross slip of dislocations leads to rearrangements of the remaining dislocations, creating subgrains [19] seen in Figure 2-4.

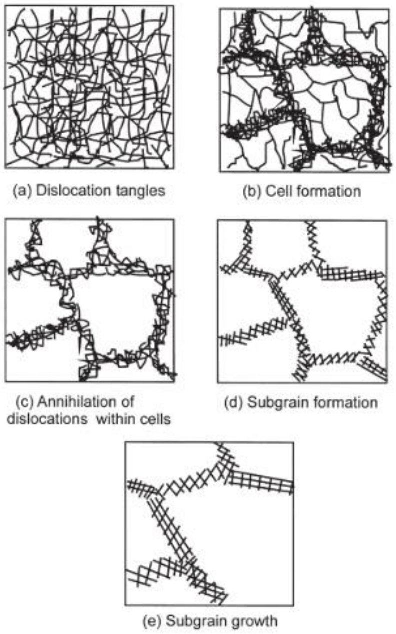

Figure 2-4: Stages in the recovery of a plastically deformed material [20].

During DRV, the material properties are partially restored to their original values, and no variation on grain geometry is appreciated. DRV is characterized by a continuous increase in flow stresses during plastic working, during which the rate of strain hardening gradually decreases with deformation and approaches zero at high strains [21].

2.3. Nucleation mechanism

When nucleation is introduced, our first difficulty lies in defining what we mean by a recrystallization nucleus. A working definition might be a crystallite of low internal energy growing into deformed or recovered material from which it is separated by a high angle grain boundary [22]. Nucleation is critical in determining the resulting grains size and orientation. Therefore, to control recrystallization effectively, it is necessary to understand the mechanisms of nucleation and the parameters that influence it.

The classical homogeneous nucleation theories associated with solidification or phase transformation do not require recrystallization due to its low driving force and high grain boundary energies. However, critical stored energy must be reached before the onset of recrystallization, and under most high-temperature deformation conditions, nuclei mainly originate at, or near, the pre-existing grain boundaries.

An extensive body of literature exists, resulting in a wide range of existing nucleation mechanisms (which may vary from one material to another). Therefore, the focus is on the principal accepted mechanisms summarized for the studied case.

2.3.1. Strain-induced boundary migration (SIBM)

This mechanism was first reported by Beck and Sperry (1950) and observed in a wide variety of metals. Strain Induced boundary migration (SIBM) considers the migration of a pre-existing grain boundary toward the interior of a more highly strained grain, leaving a dislocation-free region behind the migrating boundary, as shown schematically in Figure 2-5 [22]. A characteristic feature of this mechanism is that the new grains have similar orientations to the old grains from which they have grown.

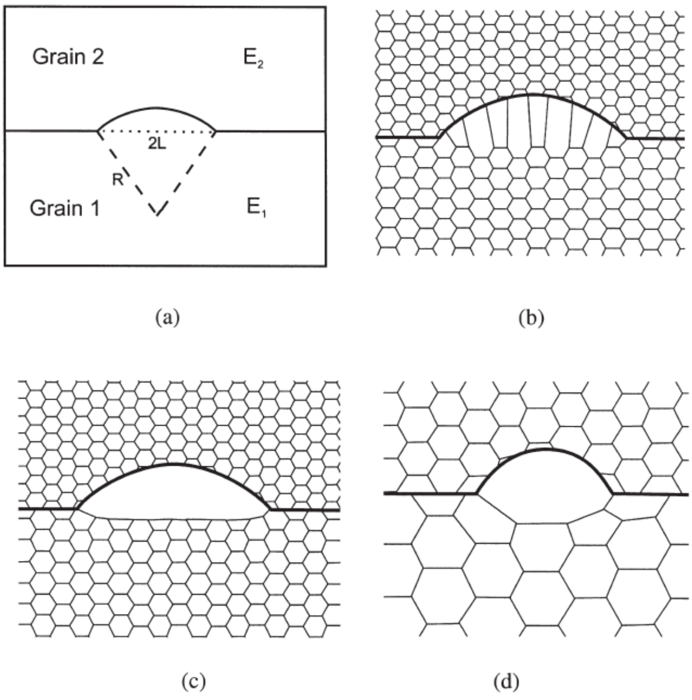

(a) (b)

(c) (d)

Figure 2-5. Strain-induced boundary migration (SIBM) of a boundary separating a grain of low stored energy (E) from one of higher energy (E), (b) dragging of the dislocation structure behind the migrating boundary, (c) the migrating boundary is free from the dislocation structure, (d) SIBM originating at a single large subgrain [22].

The conditions for the process should be favourable of energy balance between the decrease of stored energy due to the elimination of dislocations in the region behind the migrating boundary and the increase in total grain boundary surface due to bulging. The growth condition is given by Equation (1):

$$L > \frac{2\gamma_b}{\Delta E}, \tag{1}$$

where γ_b is the grain boundary surface energy per unit area and ΔE is the released energy associated with the decrease in defects, $2L$ is the initial length of the bulging boundary as shown in Figure 2-5 (a). Therefore, a critical stored energy difference is necessary for the initiation of nucleation [23].

2.3.2. Nucleation by low angle boundary migration

This model was presented by both Beck [24] and Cahn [25] in 1940. The dislocation density around the low angle boundaries may be relatively high, promoting their migration. The dislocations are continuously absorbed and increase the low angle boundaries (LAB) crystallographic orientation until it is finally transformed into a high angle boundary (HAB). The stored energy decreases during this process since the microstructural defects behind the moving sub grain boundaries are removed or rearranged as is showed in Figure 2-6.

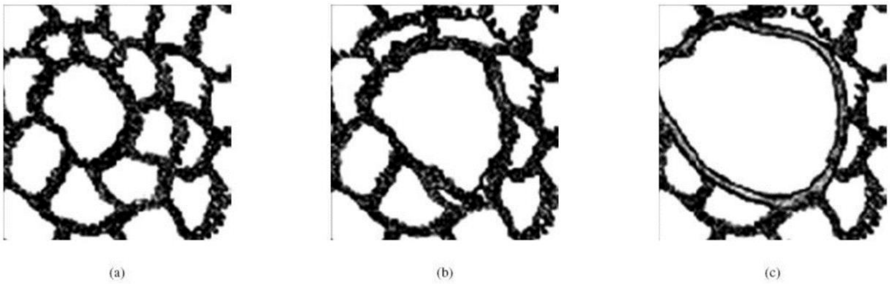

Figure 2-6. The sequence shows the nucleation of a recrystallized grain starting from a subgrain: a) initial substructure; b) the larger (middle) subgrain growth over the other (smaller) ones; and c) an area free of defects associated with a large angle boundary that is being formed [26].

Riots *et al.* [26] concluded that this mechanism usually occurs preferentially in LSFE materials under high annealing temperatures, at high strains and large spread in the subgrain size distribution.

2.3.3. Nucleation by subgrains coalescence

The coalescence mechanism of adjacent subgrains involves a rotation between the subgrains in which the respective crystal lattices match, as shown in Figure 2-7.

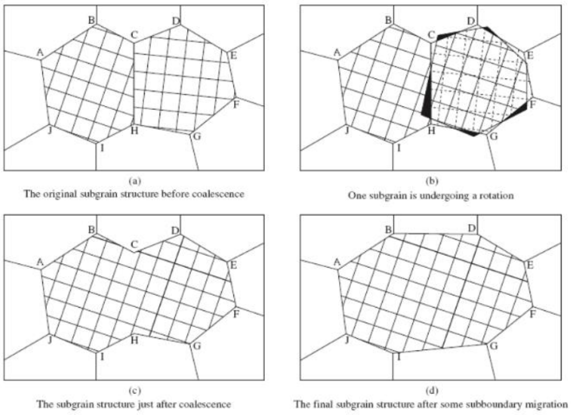
(a) The original subgrain structure before coalescence

(b) One subgrain is undergoing a rotation

(c) The subgrain structure just after coalescence

(d) The final subgrain structure after some subboundary migration

Figure 2-7. Coalescence of two subgrains by rotation of one of them: a) original structure prior to coalescence; b) rotation of the CDEFGH grain; c) subgrain structure after coalescence, and; d) final structure after sub-boundaries migration [27].

This mechanism is associated with transitions bands [22], a large spread in the distribution of subgrain angles, moderate strains, regions next to grain boundaries, relatively low annealing temperatures and metals with high SFE [22].

2.3.4. Nucleation by grain boundary sliding

Sakai *et al.* [21] proposed a new nucleation model for the DRX process, shown in Figure 2-8. First, grain boundary sliding occurs at appropriate boundaries during hot forming. As a result, dislocation is accumulated, and then, the subgrain boundaries (from close to the above) developed a grain boundary serration (Figure 2-8a). Next, the local concentration of strains is developed due to the continuous grain boundary shearing at these serrations (Figure 2-8b), which assist the operation of grain boundary bulging, so the bulging mechanism operate much easier than in cold deformed grain structures. Finally, the DRX nucleus is formed by bulging the serrated grain boundaries (Figure 2-8c).

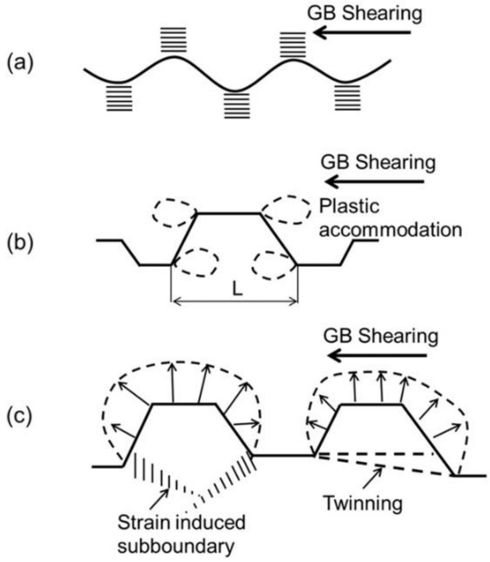

Figure 2-8. Schematic graph showing the nucleation of DRX grain at a grain boundary (a) The evolution of sub-boundaries accompanies boundary corrugation (b) Partial grain boundary sliding/shearing, leading to inhomogeneous local strains (c) Bulging of parts of a serrated grain boundary accompanied by the evolution of dislocation sub-boundaries or twinning, leading to a new DRX grain [23].

2.4. Dynamic recrystallization

To investigate DRX, understanding the flow stress behaviour is necessary to develop the conditions for the hot compression tests. The corresponding flow curves are then obtained and used to set the critical conditions for the onset of DRX. In addition, it is necessary to determine the hot working parameters, which directly affects the microstructure changes during DRX and, consequently, the model.

For microstructural studies, Electron Backscatter diffraction (EBSD) is a powerful tool to obtain detailed information about the development of the grain during plastic deformation. It is well suited for both qualitative and quantitative studies of deformation structures. EBSD allows obtaining highly detailed crystallographic information from large areas of a polished specimen by stepping an SEM beam across the sample and characterizing each point. Then, different maps can be obtained, like Orientation Image Microscopy (OIM), as shown in Figure 2-9, which allows establishing direct neighbourhood relationships between the different grains to identify deformed from recrystallized structures.

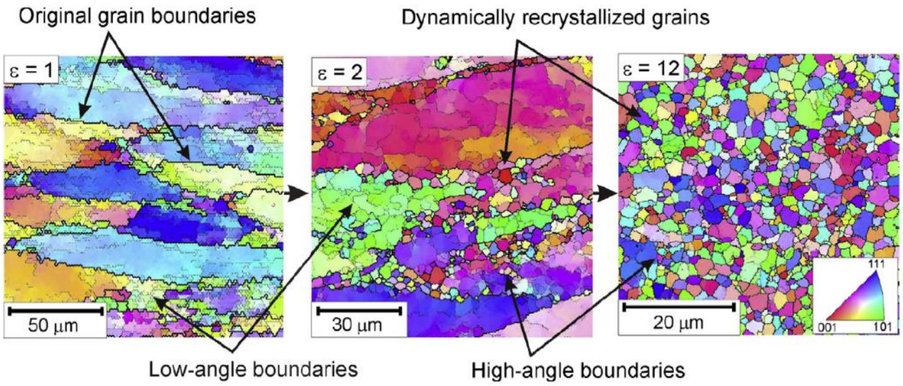

Figure 2-9. Development of new grains due to continuous dynamic recrystallization (cDRX) observed by Orientation Image Microscopy [21].

It has been recognized that the dynamic mechanism involves that the grains initially have wavy boundaries and contains dislocations substructures that vary from grain to grain. Therefore, even after DRX is fully developed, regions packed with substructures remain present. A typical substructure developed during continuous dynamic recrystallization (cDRX) is the necklace structure (Figure 2-9), where the new grains developed along the boundaries. Therefore, the onset of DRX depends sensitively on the deformation conditions [21].

2.4.1. Flow stress behaviour under the hot working conditions

Numerous metallic materials have displayed two types of deformation behaviour under hot working conditions, as shown in Figure 2-10. In the case of DRX, new grains appear during straining. The new grains produce softening, decreasing the work hardening rate until, eventually, there is a clear stress peak. Then, the flow stress decreases with increasing strain until the level associated with steady-state deformation is attained (Figure 2-10 (a)). The steady-state flow stress reflects the dynamic equilibrium between strain hardening and softening.

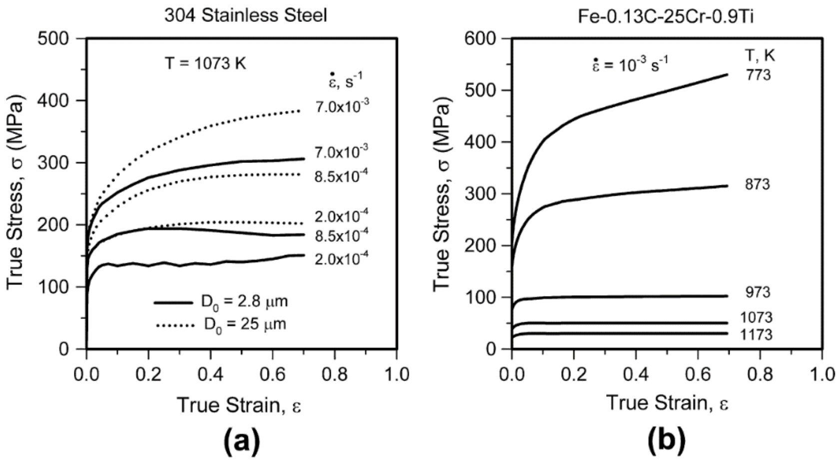

Figure 2-10. Typical stress-strain curves obtained during the hot compression of steels accompanied by (a) discontinuous dynamic recrystallization (dDRX) in austenite and (b) dynamic recovery (DRV) in ferrite [21].

A continuous increase in flow stresses characterizes the second type of high-temperature behaviour. The strain hardening rate gradually decreases with deformation and approaches zero at high strains, leading to a steady-state of flow. This behaviour is attributed to the operation of DRV as the primary restoration process. In this case, the steady-state flow is attained when the rate of DRV has increased sufficiently to balance the strain hardening rate. Such recovery-controlled steady-state flow is generally observed at modest strains (ε<1) during hot deformation at relatively low strain rates [21].

2.4.2. Investigation of DRX through flow curves

DRX is one of the most critical restoration mechanisms during the hot deformation of steels in their austenitic conditions. The occurrence of DRX usually results in a single peak in the flow curve of deformed material. The critical conditions for the transition from single to multiple peaks, the microstructural development, and grain size evaluation under multiple peaks behaviours are examples of issues that have not been wholly resolved [28].

Two of the most common criteria are reviewed to characterize the transition from single to multiple peak flow curves for this work. According to the first criterion, proposed by Luton and Sellars [29], the transition from multiple to single peak behaviour is associated with the peak strain (ε_p) and the strain close to recrystallization strain (ε_x). According to this model, when the peak strain is larger than the recrystallization strain (i.e. $\varepsilon_p > \varepsilon_x$), the flow curve will show multiple peaks. In contrast, the single peak behaviour appears when $\varepsilon_p < \varepsilon_x$, as it can be seen in Figure 2-11.

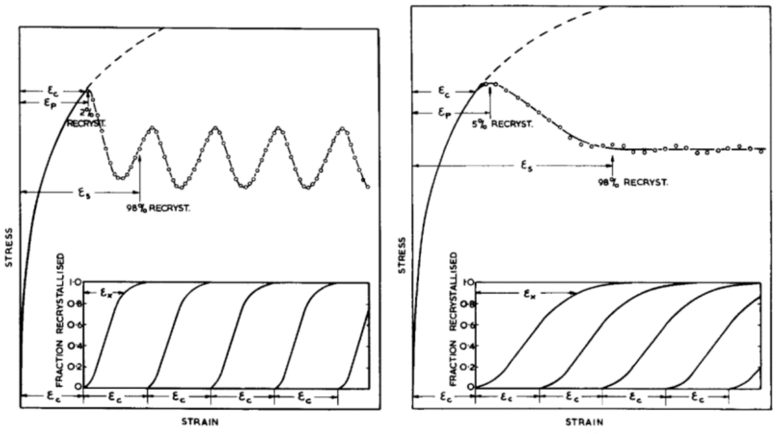

(a) (b)

Figure 2-11. Predicted stress-strain curves for dynamic recrystallization (a) critical strain to initiate recrystallization, $\varepsilon_c > \varepsilon_x$, the strain occuring in the time for a large fraction of recrystallization. (b) $\varepsilon_c < \varepsilon_x$ [29].

In the second criterion, proposed by Sakai *et al.* [30], each flow curve type represents a specific recrystallisation mechanism. According to this model, the single peak flow curve reflects a growth controlled mechanism (i.e. grain refinement) and usually the initial grain size (d_0) is greater than twice the steady-state DRX grain size (d_{ss}). In contrast, the multi-peak flow curve is associated with a nucleation control and impingement mechanism (i.e. grain coarsening) and also $d_0 < 2d_{ss}$. The single peak behaviour is usually associated with dynamic recrystallization based on the deformation of a necklace structure. However, the necklace mechanism cannot occur during grain coarsening, and the growth of each new grain is stopped by grain boundary impingement with other recrystallizing grains [30]. However, several studies have been shown that this criterion is not always valid for all materials, and the Luton and Sellars model can predict the flow curve behaviour more accurately [28].

Due to the importance of grain refinement in hot industrial processes, the critical conditions that cause a transition from single to multiple peaks have practical importance.

2.4.3. The critical condition for the onset of DRX

Recrystallization during hot working operations of metals and metallic alloys (temperature in the range of 0.5-0.9 T_m, where T_m is the absolute melting temperature [31]) is commonly caller discontinuous dynamic recrystallization (dDRX).

Frequently, the presence of DRX is indicated by a well-defined peak stress value (σ_p) on the experimental stress-strain ($\varepsilon - \sigma$) curves. However, DRX may be initiated at strain values lower than those corresponding to the peak stress [29] and could occur even though no apparent peak stress is observed. Not focusing on cases of recrystallization of the multiple peaks type, because of the short interest from an industrial point of view, the behaviour of low stacking fault energy (LSFE) materials differs from high stacking fault energy (HSFE) materials and generate two well-differentiated behaviours and DRX flow curves. In both cases, strain hardening and softening by dynamic recovery (DRV) are the controlling deformation mechanisms at low strains.

In HSFE, the strain hardening is balanced by DRV, and the steady-state is reached when DRV is the leading restoration process. This behaviour is characterised by a continuous increase in the flow stresses during plastic deformation. The presence of the DRV promotes equilibrium, and the rate of strain hardening (SH) progressively decreases with straining and is minimized at high strains, leading to steady-state stress. On the other hand, in low SFE materials, such as SASS, the DRV kinetics is slow, allowing DRX to occur because the large amount of dislocations generated during work hardening is not annihilated. Therefore, it can be assumed that once a particular critical dislocation density value ρ_c (associated with a critical strain) is reached, DRX is activated as an additional softening mechanism.

The critical dislocation density depends on the strain rate, temperature, chemical composition, and grain size for a given material. When this value is reached under low strain rate conditions, DRX is initiated by the growth of high angle boundaries (HAB) formed by dislocation accumulation. Consequently, the local dislocation density gradient differences over the grain boundary surrounding areas act as the driving force for the nucleation of new nuclei [15], followed by the long-range migration of HAB. Thus, conventional DRX is considered to be a two-step process governed by the following: (i) nucleation and (ii) grain growth [22].

The flow curve displays a peak in stress, after which stress values gradually decrease until they reach the steady-state (σ_{ssDRX}). The last state reflects the dynamic equilibrium between strain hardening and strain softening due to the formation of new grains and the associated grain boundary migration [21]. Consequently, the steady-state stress can be achieved via DRV (HSFEP materials) and DRX (moderate to LSFE materials). However, Gottstein et al. [32] point out that the strain is not a state variable of crystal plasticity. Therefore, to be precise is more appropriate to talk about critical conditions for microstructural instability than the critical strain. As a strain itself does not describe the current state of the material. However, some models formulated the critical strain for DRX in terms of a critical dislocation density or deformation resistance for a given grain size in the deformation history.

Nucleation mainly occurs along existing grain boundaries for a single peak behaviour, referred to as the so-called necklace microstructure [22],[33]. In this situation, grain growth is stopped by concurrent deformation. When all the grain boundary sites are occupied and exhausted, other new grains are nucleated within the primary grains at the recrystallized and un-recrystallised grains interface. On the other hand, for the multiple peak case, the growth of each new grain is terminated by boundary impingement and not by the concurrent deformation [15].

Wray [34] was the first author to highlight that the critical strain corresponds to applying a minimum amount of energy required to start the DRX. This critical value reflects the upper limit of energy stored in the material and is necessary (but insufficient) for starting DRX. The initiation of DRX further requires that any counterpart to the energy stored, for example, the energy dissipation rate, also reaches a critical value [35].

The onset of DRX cannot be easily extracted from the stress-strain curves. For simplicity, some authors state that the value of deformation needed to start DRX is proportional to the peak strain ε_p [36]:

$$\varepsilon_c = \alpha \varepsilon_p \, , \tag{2}$$

where α is a coefficient of proportionality. In this regard, the peak strain and the critical strain for dynamic recrystallization are usually related by a factor ranging between 0.5 and 0.90 [22]. Here, this factor is defined as the critical radio of strains:

$$R_c = \frac{\varepsilon_c}{\varepsilon_p}, \tag{3}$$

Several facts can explain the relative scatter observed in the literature for R_ε. Along with the dependence of this relationship on a given material, the test employed can significantly affect the measurement of ε_c [37].

Several evaluation methods have been proposed to obtain the strain associated with the initiation of DRX. Four ways to determine the critical strain for the onset of DRX are found in the literature, namely, (i) through metallographic determination, (ii) by using analytical expressions for ε_c or ε_p (iii) by applying methods to calculate the critical strain for DRX, and (iv) by directly calculating the critical strain ratio applying analysis of constitutive models and physically-based models to derive the DRX nucleation.

2.4.3.1. Metallographic determination

Determining the critical strain for initiation of DRX through metallography and metallographic observation techniques involves an apparent effort to implement extensive tests, sample preparation, and examination, which may be a very time-consuming task.

Several authors have shown the microstructure evolution from critical to steady-state conditions during hot deformation. Moreover, depending on the facilities, post-dynamic phenomena occasionally occur. Due to the instability of austenite at room temperature, the detection of the initiation of DRX can be inaccurate enough by employing classical metallography. Additionally, during the quenching phase, changes might occur and modify the deformed microstructure, which adds difficulty to the metallographic analysis. In the following, some examples are cited [15].

2.4.3.2. Analytical expressions for ε_c or ε_p

Perhaps the easiest way to determine the critical strain ε_c for a given material is through the assumption of a critical strain ratio and to derive the critical strain through an analytical expression for the peak stress as a function of testing conditions and microstructure. Equation (4), suggested by Sellars [38], represents one of the most common and widely reported empirical relationships for the determination of the peak strain as a function of the thermomechanical variables:

$$\varepsilon_\mathrm{p} = k d_0^\mathrm{n} Z^m, \tag{4}$$

where k, n and m are material dependent constants; d_0 is the initial grain size, and Z is the Zener-Hollomon parameter (s^{-1}) [39] defined as follows:

$$Z = \dot{\varepsilon} \exp\left(\frac{Q_\mathrm{hw}}{RT}\right), \tag{5}$$

where $\dot{\varepsilon}$ is the strain rate (s^{-1}), Q_hw is the activation energy for hot deformation (J mol^{-1}), R is the universal gas constant (J mol^{-1} K^{-1}), and T is the absolute temperature (K). When $k d_0^\mathrm{n} = K$, the initial grain size is constant, then, Equation (4) can be simplified into Equation (6) [40]:

$$\varepsilon_\mathrm{p} = K Z^\mathrm{m}. \tag{6}$$

These expressions have been developed empirically and consider the influence of the initial microstructure through the grain size prior to deformation d_0 and the deformation conditions through the Zener–Hollomon parameter Z.

Several authors have developed variations for Equation (4) to consider the effect of different factors during hot working, i.e. temperature, strain rate and initial grain size. These matters are discussed later on.

2.4.3.3. Methods to calculate ε_c

Several researchers have studied dynamic recrystallisation kinetics to predict the flow stress behaviour and associated microstructural changes.

Luton and Sellars [29] have suggested a critical strain approach to predict the flow stress behaviour in terms of the incubation strain ε_{c} for the onset of DRX and the strain required for a complete DRX cycle ε_{x}. This model, principally concerned with the mechanical aspects of dynamic recrystallisation, provided a significant advance in understanding the DRX phenomena. However, it does not involve the metallurgical principles of DRX, and some limitations are present [30].

One of the most recognized and realistic models that address the nucleation for the onset of DRX was proposed in 1978 by Roberts and Ahlblom [41]. The reduced driving force (i.e., the stored energy difference) modifies the average energy balance, defining the conditions for nucleation of new grains and the kinetics of nucleation, depending on the energy of the grain boundaries and the dislocation density difference, between the new recrystallised grains and the matrix [41]. Nucleation is usually promoted by localized strain-induced grain boundary migration. Once the critical dislocation density (associated with the critical strain) is attained, the balance between the driving force and surface energy is that the largest bulges grow with a continuous loss of free energy. The recrystallisation reaction begins and is developed until the sites at the initial grain boundaries are extinguished. Subsequently, the reaction proceeds via nucleation at the interface between unrecrystallised and recrystallised material up to the regions of the new DRX grains, originating from the surrounding grain boundaries, permeating the centres of the pre-existing grains. This condition corresponds to the attainment of the steady-state on the proper stress-strain curve [22].

This model considers the effect of grain size changes but is limited to the case of grain refinement and single peak flow behaviour. This approach is based upon classical nucleation theory [22], describing the strain hardening and dynamic recovery phenomena considering the evolution of the global dislocation density ρ, neglecting the sub-grain wall density, as follows:

$$\frac{d\rho}{dx} = \frac{\dot{\varepsilon}}{b\,l\,m_{\mathrm{HAB}}\,\tau\,\rho} - 2\frac{\rho^2(x)}{\rho}\frac{M}{m_{\mathrm{HAGB}}}, \tag{7}$$

where x represents the direction of mobility of the migration front; b is the Burgers vector; l is the mean free path of the dislocations; m_{HAB} is the mobility of a high angle grain boundary; M is the mobility of dislocations, and τ is the dislocation line energy.

While empirical relationships are recognized to determine the critical conditions for microstructural instability for the initiation of DRX, some authors have put effort into establishing more rigorous procedures to provide the critical strain for the onset of DRX. Initially proposed by Mecking and Kocks [41], a mathematical approach, and then continued by Yan and McQueen [42], was developed to derive the critical strain. As illustrated in Figure 2-12, the onset of DRX can be determined from slope changes in the θ–σ curves, which correspond to the inflection point. Ryan and McQueen [42] defined the critical strain as the strain value at which the experimental flow stress curves deviate from the theoretical σ–ε curves when DRV is the only active softening mechanism [43]. Figure 2-13 shows that extrapolation of the second linear segment of the $\theta-\sigma$ curve until $\theta=0$ determines the theoretical $\sigma-\varepsilon$ curve, corresponding to DRV acting as the main restoration mechanism operating (σ_{SDRV}) [22]. Nevertheless, in this case, the determination of the inflection points and the followed extrapolation procedure was not well defined.

Wray et al. [34] highlighted that the critical strain corresponds to the minimum energy required to start DRX. Poliak and Jonas [35], [44] have reported a theory about the initiation of DRX mainly based on previous works and energetic considerations [34], [45]. This approach is based on the thermodynamic laws governing irreversible processes, identifying the onset of DRX by an inflection point in the θ–σ curve, which is defined as the strain hardening rate corresponding to the appearance of an additional degree of freedom in the system. Nevertheless, further consideration of the stored energy threshold into the material proposed by Wray [34] is essential but may not be sufficient. Further, the kinetics of the process must be considered. The stored energy needs to attain a maximum value, while the latter condition demands that the energy dissipation rate reaches a minimum, and it can be quantified in terms of the appearance of a minimum in the variation of the hardening rate $(-\partial\theta/\partial\sigma\ |_{T,\dot{\varepsilon}})$ with the stress, as displayed in Figure 2-13. The approach involves multiple numerical differentiation and sometimes promotes a substantial experimental noise during the data treatment. It should be noted that, to precisely define the critical strain for dynamic recrystallization, it is necessary to determine the minimum in $(-\partial\theta/\partial\sigma|_{T,\dot{\varepsilon}})$ or the minima in $(-\partial \ln\theta/\partial \ln\sigma)$ and $\left(-\frac{\partial \ln\theta}{\partial\varepsilon}\right)$ [35], [44]. Moreover, this method applies to variable strain rate conditions and any testing technique [46]. Najafiezadeh and Jonas [47] proposed that the θ–σ curve can be fitted using a third-order polynomial equation applied to the normalized σ–ε curve.

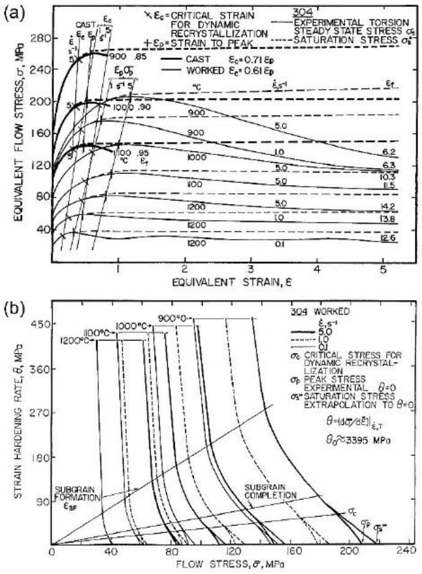

Figure 2-12. (a) Experimental flow curves of an AISI 304 steel and (b) corresponding experimental θ-σ curves and hypothetical strain hardening rate-stress curves (DRV) [42].

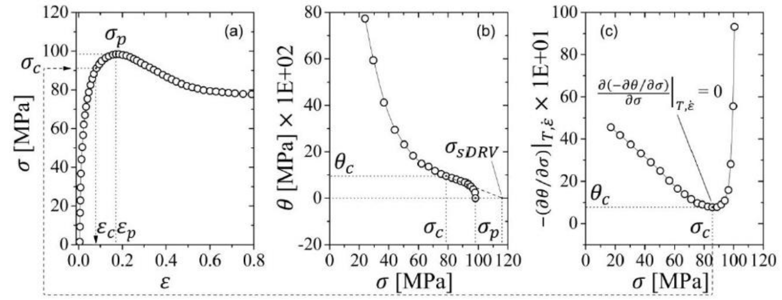

Figure 2-13. Schematic of the Poliak-Jonas procedure to determine ε_c (a) flow curve, (b) corresponding work hardening rate θ vs Stress and (c) first derivative of the work hardening rate θ vs stress [35],[44].

As a complement of the Poliak and Jonas approach [35], [44], Najafizadeh and Jonas [36] have proposed that the normalized true stress-strain curve (σ/σ_p vs. $\varepsilon/\varepsilon_\mathrm{p}$) is suitable to apply the second derivative criterion [44] and the normalized strain hardening rate versus the normalized stress curve, $\partial(\sigma/\sigma_\mathrm{p})/\partial(\varepsilon/\varepsilon_\mathrm{p})$ versus σ/σ_p, can be fitted using a third-order polynomial equation in order to determine the inflection points that identify the point of initiation of DRX in the range of temperature and strain rate of interest. Futhermore Najafizadeh and Jonas [47] showed that the critical stress and the critical strain ratio $R_\sigma = \frac{\sigma_c}{\sigma_p}$ and R_ε are approximately constant and independent of the Z parameter (Figure 2-14).

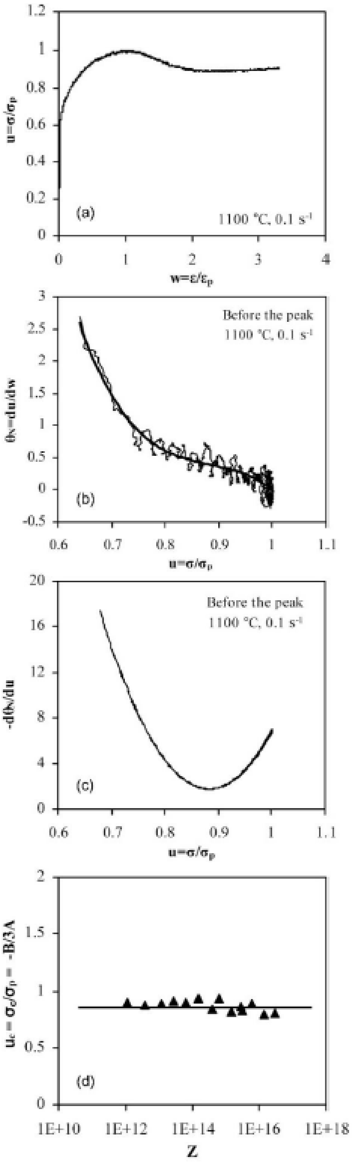

Figure 2-14. (a) Normalized stress-strain curve, (b) normalized strain hardening rate vs normalized stress curve, (c) differentiation of normalized strain hardening rate vs normalized stress curve, and (d) normalized critical stress ratio vs the Zener-Hollomon parameter Z [36].

According to Gottstein *et al.* [32], the second derivative criterion (SDC) approach reported by Poliak and Jonas does not offer enough details. For example, it lacks any information about the mechanisms that lead to an instability of the microstructure.

2.4.3.4. Calculation of the critical strain ratio by applying constitutive models

Typically, several flow stress models, taking into account DRX, comprise the following:

(i) A model for strain/work hardening and dynamic recovery.
(ii) A nucleation criterion for dynamic recrystallization.
(iii) A function describes the dynamically recrystallised volume fraction.
(iv) A rule of a mixture determines the macroscopic resulting flow stress.

The direct application of the Poliak and Jonas second derivative criterion (SDC) to determine the critical strain for the initiation of DRX ($\partial\left(-\frac{\partial\theta}{\partial\sigma}\right)/\partial\sigma\Big|_{T,\dot{\varepsilon}}$), in a given constitutive model describing the strain hardening and dynamic recovery stages, is a topic that has not received much attention. This task often does not always give satisfactory and precise results [44]. This approach is not applicable in many constitutive models and equations because it can give trivial, inaccurate, and incongruous solutions. An apparent violation of the SDC occurs when the model for strain hardening and dynamic recovery is incapable of showing an inflection point in the strain hardening rate as a function of the flow stress. Regarding this fact, some authors have developed mathematical approaches to determine the necessary conditions (consistency check) that the constitutive law, describing the strain hardening and the dynamic recovery, must meet to allow the applicability of the Poliak and Jonas criterion [15].

Bambach [41] shows three types of inconsistencies with the SDC when the effect of dynamic recrystallisation is included in the flow stress model when it is not sufficiently many times differentiable at the critical point, illustrated in Figure 2-15:

(i) The hardening model does not produce an inflection point in the strain-hardening rate.
(ii) The point at which the criterion identifies the location of the point of inflection does not match the actual point of inflection in the experimentally measured strain-hardening rate.
(iii) The derivates of the strain-hardening rate are discontinuous.

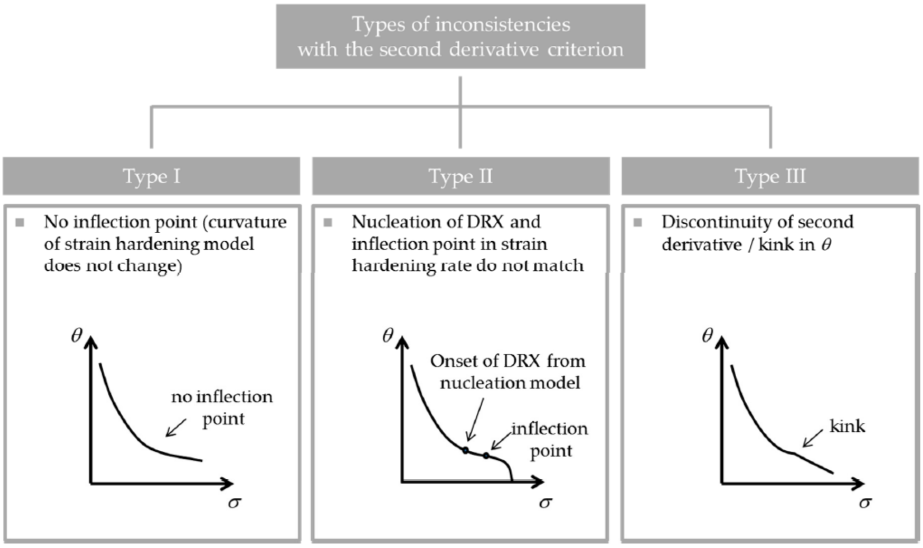

Figure 2-15. Schematic representation of three types of inconsistencies with the second derivative criterion (SDC) [48].

The SDC by Poliak and Jonas [44] was derived from principles of irreversible thermodynamics. Consequently, a flow stress model that takes DRX into account should adhere to this criterion to be consistent with the experimental data and ensure that the model is thermodynamically consistent. A prerequisite for a flow stress model to follow the SDC by Poliak and Jonas [44] is that the predicted flow stress is sufficiently smooth. Thus, a continuous strain-hardening rate, along with its first and second derivatives, are computed.

In a subsequent paper, Jonas *et al.* [49] analyzed previously published hot flow data [50] and contemplated the dynamic transformation (DT) as an additional softening mechanism that contributes to the microstructural and mechanical softening for a single-peak curve. Accordingly, the authors also considered and analyzed the effect of the polynomial order (2 to 15) on the sensitivity of the double differentiation method as well as on the actual values of the critical strain determined.

The double differentiation method usually requires at least an eight order polynomial for function fitting, and the use of polynomials of lower degrees can cause poor accuracy in the fitting process. Using the first part of the flow curve, Jonas *et al.* [49] stated that polynomial orders below three cannot detect any minima at all. In contrast, polynomial order between 4 and 7 can detect the DRX minima but not identify the minimum DT. On the other hand, both minima are distinguished for polynomials order above eight or higher. As a result, the critical strain values for DT show a small dependence on polynomial order. However, the critical strain values for DRX show some scatter, and these differences can be associated with the actual value of true strain and the slope of the flow curve after yielding. Finally, Jonas et al. [49] concluded that all the DT critical strains were within about ± 0.5% of the average value and the DRX critical strains were within about ± 2.0%.

The traditional way to determine the initiation of dynamic recrystallisation reported by Poliak and Jonas [44] comprises a relatively complex and time-consuming procedure of manipulation and processing data, including several steps, such as smooth and filtering the raw data, conversion to stress-strain data, compensate the stress drop owing to adiabatic heating or fiction (dissipation heating), second smoothing steps, determination of θ.

As mentioned above, and in some cases, the Poliak and Jonas method [44] involves multiple smoothing steps (e.g., using fast Fourier transform-based procedures, FFT). Accordingly, Jonas et al. [51] applied a seventh-order polynomial, and in some cases, a higher-order polynomial, to fit and smooth each $\sigma - \varepsilon$ curve and a third-order polynomial in the description of the strain hardening rate versus flow stress data, $\theta - \sigma$ [36].

Lohmar and Bambach [52] developed a Thin Plane Spline (TPS) method that requires additional flow strain–stress data preparation. In addition, this new approach interpolates multiple strain-stress flow curves. Finally, Lohmar and Bambach [52] remarked that the TPS approach seems to be a more robust determination of the critical strain for the onset of DRX than the polynomial interpolation proposed by Jonas *et al.* [51], which occasionally yields multiple candidates for critical points. However, some limitations are cited, namely, at lower temperatures, the compensation of dissipation heating might affect the determination of the critical conditions for the onset of DRX and cause the detection of relatively low critical strain ratios.

2.4.4. Influence of temperature, strain rate and initial grain size

As it was introduced previously in this chapter, Luton and Jonas [53] studied the influence of strain rate ($\dot{\varepsilon}$) and temperature in the shape of the stress-strain curves, as is showed in Figure 2-16 a), when the curve changes from multi-peak type to single peak when the strain rate is increased. The same transition can be observed when the temperature decreases (Figure 2-16 b)).

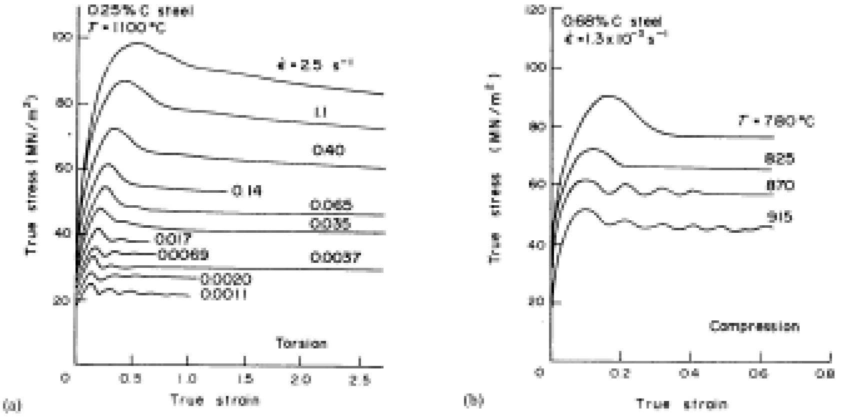

Figure 2-16. a) Influence of strain rate on the flow curves; b) Effect of temperature of gamma iron at $\dot{\varepsilon} = 10^{-3}$ s^{-1} [53].

According to the above experimental observations, there is an equivalence between increasing/decreasing temperature and decreasing/increasing strain rate. Therefore, the Zener-Hollomon parameter was introduced for this purpose, as is shown in Equation (8):

$$Z = \dot{\bar{\varepsilon}}\, e^{\left(\frac{Q}{RT}\right)}, \tag{8}$$

where $\dot{\bar{\varepsilon}}$ is the equivalent strain Q is the activation energy of deformation (J mol^{-1}), R is the ideal gas constant (J mol^{-1} K^{-1}) and T is the temperature (K). Accordingly, for the discontinuous DRX regime, flow stress curves of multiple peaks appear when T is high and $\dot{\varepsilon}$ is low (low Z), and single peak low-stress curves exhibit it low T and high $\dot{\varepsilon}$. Additionally, the steady-state flow stress decreases with deformation temperature while its variation with strain rate is unexploited primarily [23]. In general, recrystallization kinetics increases with increasing deformation temperature and decreasing strain rate. The recrystallized grain size increases with strain and approaches the steady-state value at ~10% of DRX. Also, it increases with increasing deformation temperature and decreasing strain rate [23].

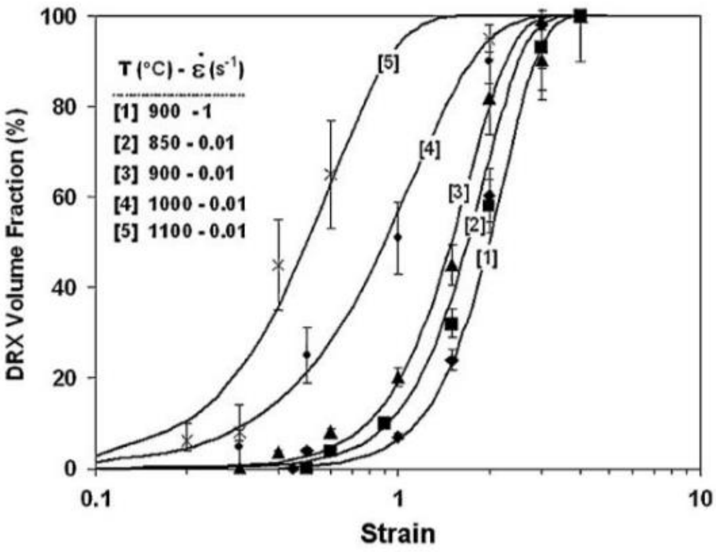

Figure 2-17. The effect of temperature and strain rate on the kinetics of 304 stainless steel [27].

It is also well known now that in a condition of hot deformation, a decrease in the initial grain size accelerate the onset of DRX and increase DRX kinetics. The effect of initial grain size on the hot torsion behaviour of nickel has been examined by Sah *et al.* [54] in the range of 800-1000 °C over a wide range of strain rates. In Figure 2-18, faster kinetics of DRX is observed when decreasing the initial grain size, which indicates that the onset of recrystallization also decreases with initial grain size. This affirmation was further confirmed by El Wahabi *et al.* [55] and Dehghan-Manshadi *et al.* [56], which observed that the recrystallized kinetics at two different strain rates were obtained from measurements made at two different depths within identical specimens. Thus, the strong influence of initial grain size on recrystallisation kinetics is due to the change in the grain-boundary surface area, the leading nucleation site.

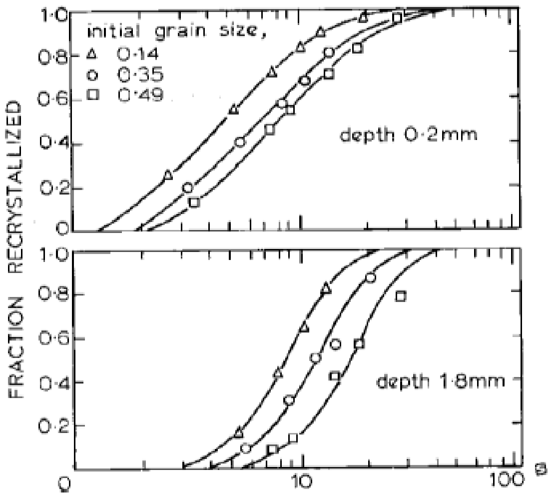

Figure 2-18. Relation between fraction recrystallized and angle of twist for different initial grain sizes in nickel at 1000 °C and 0.05 rev/min [54]**.**

Further studies developed by Sah *et al.* [54] showed a transition from single-to multiple-peak behaviour when the initial grain size decreases below a critical value, as is shown in Figure 2-19 a). On the other hand, for a given temperature and strain rate, the effect of initial grain size on DRX final grain size and steady-state stress is less pronounced, even negligible [54], [57], as shown in Figure 2-19:

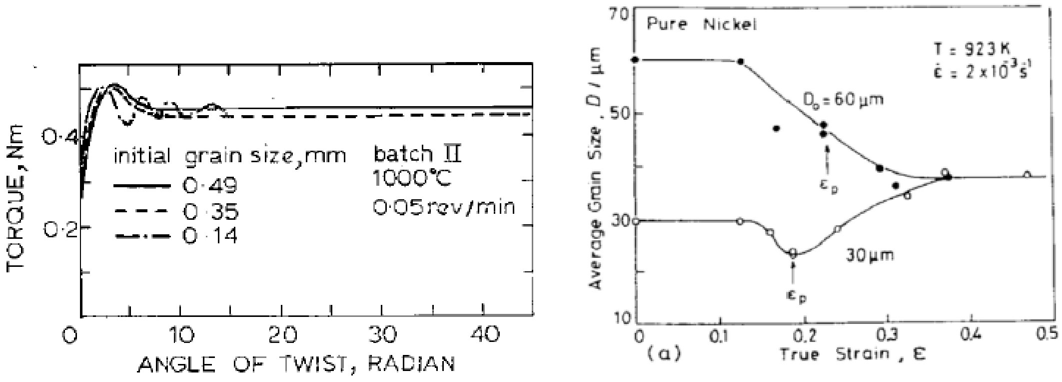

a) b)

Figure 2-19. a) Typical torque/twist curves for material with different starting grain sizes [54] **b) Effect of initial grain size D on the average grain size** [57]**.**

Dehghan-Manshadi [57] verified peak and critical strain behaviour, which observed a downward trend with initial grain size and followed a power-law function with the Zenner-Hollomon parameter. They found that both peak and critical strains of finer-grain size showed almost no slope change with increasing Z. Furthermore, there was no change in behaviour over the entire Z range for coarse-grain size, i.e. the peak and critical strains increase linearly with Z, as shown in Figure 2-20 a). Figure 2-20 b) suggests that the difference between the peak stress of fine and coarse grain materials is negligible at a very high Z value.

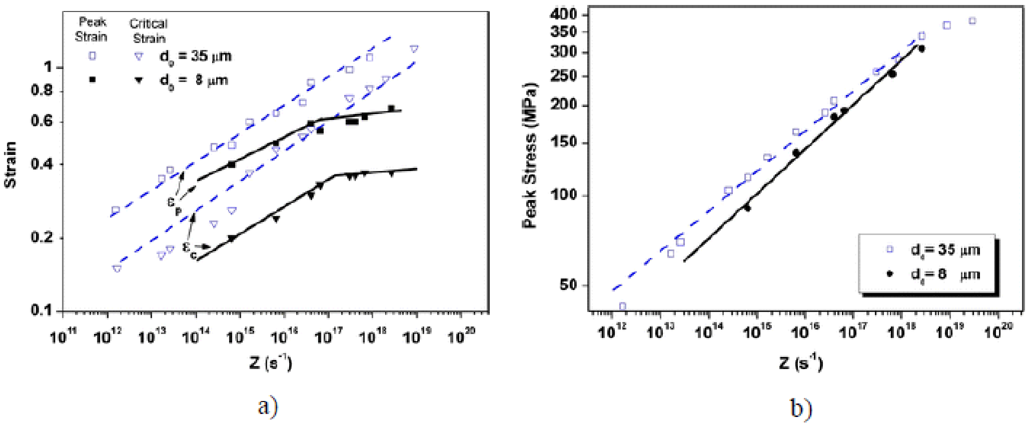

a) b)

Figure 2-20. a) Peak and critical strains as functions of Z for fine- and coarse-grain materials [56], **b) Peak stress as a function of Z for fine - and coarse-grain materials** [56].

Dehghan-Manshadi and Hodgson [56] confirmed a transition from discontinuous to continuous DRX (cDRX) with a decrease in the initial grain size [34]. It was proposed that the ratio of recrystallized grain size, d_{drx}, to the initial grain size, d_0 can be considered as an important factor determining the DRX mechanism. When d_{drx}/d_0 is close to 1, no noticeable change occurs in the initial microstructure during hot deformation, the operating DRX mechanism is through rearrangement of grain and subgrain boundaries, i.e. cDRX. If $d_{\mathrm{drx}} \ll d_0$On the other hand, DRX breaks down the initial grains into several smaller DRX grains by serration of initial grain boundaries and nucleation of new DRX grains on these boundaries.

Hot-working studies commonly use a wrought material as an initial microstructure. However, it is interesting to study the impact of grain size from as-cast initial microstructures. Mataya *et al.* [58], [59], studied the recrystallization for as-cast 316L [58] and 317L [59]. They found a difference in the recrystallization rate between the as-cast and the wrought 304L, associated with larger initial grain size. Later on, Mandal *et al.* studied the same case for the as-cast 304 [60] confirmed the influence on the initial microstructure on the critical values for the initiation of DRX. Huiquin *et al.* [61] went further and compared the behaviour for the Mn18Cr18N SASS with as-cast versus wrought starting microstructure. They found that the deformation activation energy of as-cast is higher than wrought material, which implies that DRX is more difficult due to as-cast coarse grains [61].

2.4.5. Microstructure changes associated with DRX

This section discusses that DRX generally starts at the pre-existing grain boundaries [22], as shown in Figure 2-21 a). New grains are subsequently nucleated at the boundaries of the growing grains, as is seen in Figure 2-21 b), and in this way, a thickening band of recrystallized grains is formed, as shown in Figure 2-21 c). If there is a significant difference between the initial grain size (D_0) and the recrystallized grain size (D_{rx}), the necklace structure formation starts by the successive appearance of next layers (Figure 2-21 b)-c)), Moreover, eventually, the material will become fully recrystallized (Figure 2-21 d)).

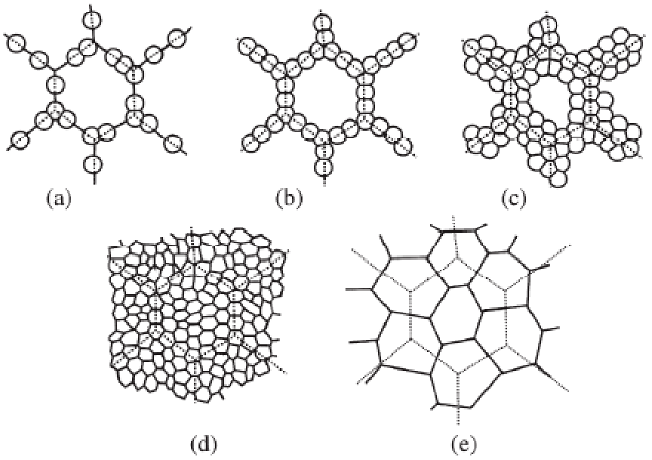

Figure 2-21. The development of microstructure during dynamic recrystallization. (a)-(d) Large initial grain size, (e) small initial grain size. The dotted lines show the prior grain boundaries [22].

During DRX, the original grains have irregular boundaries [62], which indicates localized bulging, and the formation of recrystallized grains near the grain boundaries usually remains nearly equiaxed. The inhomogeneous dynamic structures can be classified into three types of components: i) DRX nucleus (Figure 2-22 a)) with an initial value of dislocation density ρ_0Ii) growing DRX grain (Figure 2-22 b)), and iii) critically work-hardened DRX grain (Figure 2-22 b)).

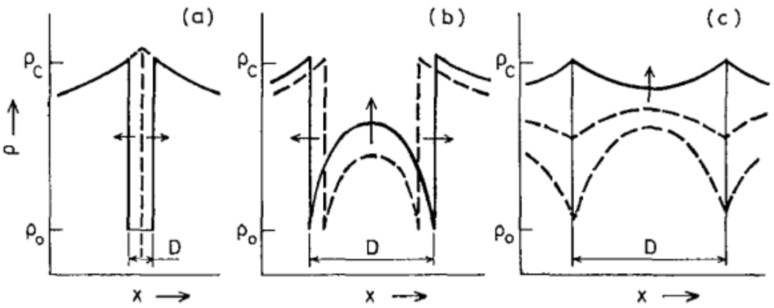

Figure 2-22. Three types of dislocation density distribution developed inside a crystallite of the DRX grain structure: (a) DRX grain nucleus, (b) growing DRX grain, and (c) DRX grain undergoing strain hardening. The present state is represented by the complete lines, followed by broken lines [63], [64]**.**

From metallographic and flow stress observations, Luton and Sellars [29] concluded that DRX occurs at strains greater than a critical value, and most importantly, the recrystallized grain size is determined entirely by the flow stress and follows a relationship with flow stress (σ) as is showed in Equation (9):

$$\sigma = \sigma_0 + kd_{\text{rex}}^{-m}, \tag{9}$$

where σ_0, k and m are constants.

In addition, experimental observations generally show that the steady-state grain size (D_{R}) during dynamic recrystallization is a strong function of the flow stress and is only weakly dependent on deformation temperature. Derby [65] proposed a relationship between the recrystallized grain size d_{rex} and σ, normalized by the shear stress G and subgrain size b respectively:

$$1 < \frac{\sigma}{G}\left(\frac{d_{\text{rex}}}{b}\right)^{2/3} < 10. \tag{10}$$

A statistical analysis of the average recrystallized grain size of data obtained from experiments and published literature was carried out by Mataya et al. [66]. They found that the average recrystallized grain size depends on the strain, initial grain size, and the Zener-Hollomon parameter as follows:

$$d_{\text{rex}} = 83.9e^{-0.537}d_0^{0.355}Z^{-0,0655}, \tag{11}$$

which shows that d_{rex} also depends on initial grain size and applied strain, which contradicts the fact that the mean size of recrystallized grain is usually considered independent of the initial grain size and does not change during DRX. The disagreement might come from slightly different chemical composition or testing procedures when taking data from published literature.

2.4.6. Modelling of dynamic recrystallization

Early attempts at modelling DRX focused on explaining the initial peak in flow-stress and the transition from multiple to single peak behaviour. In recent years, several constitutive models have been proposed or modified to describe metals and alloys' strain rate, strain, and temperature-dependent flow behaviour. Lin and Chen [67] did a critical review for metals and alloys in hot working, where the constitutive models were divided into the following three categories:

i) ***Phenomenological constitutive model***. It defines the flow stress based on empirical observations, consisting of mathematical functions. However, the phenomenological constitutive model lacks a physical background that fits experimental observations. On the other hand, its main advantage is that they use fewer material constants and can be easily calibrated. However, their empirical characteristics are usually used in limited application fields covering limited strain rate ranges and temperature and exhibit reduced flexibility.

ii) ***Physical-based constitutive model.*** Take into account the physical aspects of the material behaviours. Most of them are involved in thermodynamics, thermally activated dislocation movement and kinetics of slips. The phenomenological descriptions allow for an accurate definition of material behaviour under general loading conditions by physical assumptions and many constants.

iii) ***Artificial neural network (ANN).*** The deformation behaviours of the materials under elevated temperatures and strain rates are highly nonlinear, which makes the accuracy of the flow stress predicted by the regression methods low and the applicable range limited. Consequently, the attraction of artificial neural networks (ANN) has increased because they are best suited to solve the problems that are the most difficult to solve by traditional computational methods. Furthermore, neural networks can provide a fundamentally different approach to materials modelling and processing control techniques than statistical or numerical methods. One of the main advantages of this approach is that it is not necessary to postulate a mathematical model at first or identify its parameters using an artificial neural network.

Modelling a processing stage may need several constitutive functions depending on the complexity of the flow curves. Moreover, altered constants need multistep processes due to inter-pass softening, which indicates the need to incorporate microstructure into the models.

2.4.6.1. Phenomenological constitutive models

Phenomenological models are widely used to simulate the forming processes of metals or alloys at high-strain rates and temperatures. The most used models are the Johnson-Cook (JC) model [68], the Fields-Backofen (FB) model [69], the Arrhenius equation [39], and the well-known Johnson-Mehl-Avrami-Kolmogorov (JMAK) model.

2.4.6.1.1. Johnson-Cook (JC) model

The Johnson-Cook (JC) model [68] is most widely known as a forming temperature, strain and strain-rate-dependent phenomenological flow stress model and is successfully used for various materials with different ranges of deformation temperature and strain rate. In addition, it assumed the material to be isotropic, avoiding the traditional concept of yield surface in the constitutive equation. Therefore, the JC model has enjoyed much success because of its simplicity. The original Johnson-Cook model can be expressed as:

$$\sigma = (A + B\varepsilon^n)(1 + C \ln \dot{\varepsilon^*})(1 - T^{*m}), \tag{12}$$

where σ is the equivalent flow stress and ε is the equivalent plastic strain. A is the yield stress at the reference temperature and reference strain rate, B is the strain-hardening coefficient, and n is the strain-hardening exponent. C and m are the material constant representing the strain-rate hardening coefficient and thermal softening exponent. $\dot{\varepsilon^*} = \dot{\varepsilon}/\dot{\varepsilon_0}$ is the dimensionless strain rate ($\dot{\varepsilon}$ is the strain-rate, while $\dot{\varepsilon_0}$ reference the strain-rate), and T^* is the homologous temperature and expressed as:

$$T^* = \frac{T - T_r}{T_m - T_r}, \tag{13}$$

where T is the current absolute temperature, T_{m} is the melting temperature, and T_r is the reference temperature $(T \geq T_r)$. In Equation (12), the items $(A + B\varepsilon^n)$, $(1 + C \ln \dot{\varepsilon^*})$ and $(1 - T^{*m})$ are used for describing the work-hardening effect, the strain-rate effect and the temperature effect, respectively. The expression in the first brackets gives strain effects on the flow stress, and the second represents instantaneous strain-rate sensitivity. In contrast, the third term represents the temperature dependence of flow stress. The original JC model requires fewer material constants and few experiments to evaluate these constants. JC model assumes that thermal softening, strain rate and strain-hardening are three independent phenomena that can be isolated from each other. Therefore, a limited number of experiments is necessary to obtain the parameters. In general, the JC model represents a set of models that consider that the mechanical behaviours of material are the multiplication effects of strain, strain rate, and temperature [67]. This form is simple and has a clear physical interpretation. However, the coupling effects of strain, temperature and strain rate are omitted in the original JC model [70].

2.4.6.1.2. Fields-Backofen (FB) model

Fields and Bachofen [69] proposed the following typical formula for most metal materials:

$$\sigma = K\varepsilon^n \dot{\varepsilon}^m, \tag{14}$$

where K is the strength coefficient, n is the strain-hardening exponent, and m is the strain-rate sensitivity exponent. This equation is widely used to describe the stress-strain relationship. It fits well the work-hardening phenomenon by the strain-hardening exponent (n-value) and the strain-rate sensitivity exponent (m-value), which influenced the hot workability of metals or alloys the most.

Chang *et al.* [71] investigated the mechanical behaviour of AZ31 magnesium alloy sheets by uniaxial tensile test. Comparisons between the predicted and experimental results indicate that the predicted results only well agree with the experimental results before the peak stress, especially at high-strain-rate under low temperature. In other words, the FB model can only describe the flow stress curves at the strain-hardening stage under a higher strain rate, and the FB model is inaccurate to describe the softening behaviour. Figure 2-23 compares the calculated by the modified FB model and measure flow stress. The modified model containing softening items approaches better at the softening stage [72].

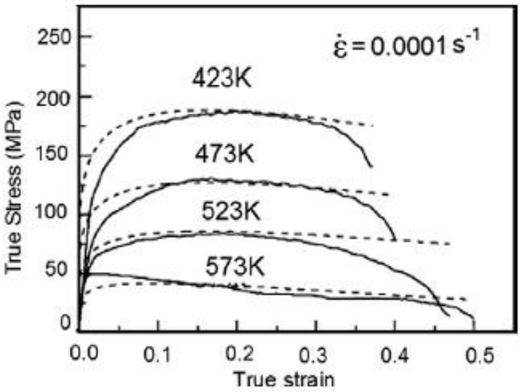

Figure 2-23. Comparison between calculated by the modified Fields-Backofen equations and measured flow curves (the dotted lines indicate the calculated values) [71]**.**

2.4.6.1.3. Arrhenius equation

The Arrhenius equation is the most widely model used to describe the relationship between the strain-rate, flow stress and temperature, especially at high temperatures. The effects of the temperatures and strain-rate on the deformation behaviour can be represented by Zener-Hollomon parameter and flow stress [39], [73]:

$$\dot{\varepsilon} = AF(\sigma)\exp\left(-\frac{Q}{RT}\right), \tag{15}$$

$$Z = \dot{\varepsilon}\exp\left(\frac{QR}{T}\right), \tag{16}$$

$$F(\sigma) = \begin{cases} \sigma^n & \alpha\sigma < 0.8 \\ \exp(\beta\sigma) & \alpha\sigma > 1.2, \\ [\sinh(\alpha\sigma)]^n & \text{for all } \sigma \end{cases} \tag{17}$$

in which, $\dot{\varepsilon}$ is the strain-rate (s^{-1}), R is the universal gas constant (8.31 $Jmol^{-1}\ K^{-1}$), T is the absolute temperature (K), Q is the activation energy of hot deformation (kJ mol^{-1}), σ is the flow stress (MPa) for a given strain, A, α and n are the material constants, $\alpha = \beta/n$.

For all the stress levels (including low and high-stress levels), Equation (15) can be represented as:

$$\dot{\varepsilon} = A[\sinh(\alpha\sigma)]^n \exp\left(-\frac{Q}{RT}\right), \tag{18}$$

then, the flow stress σ can be written as a function of Z parameter, considering the definition of the hyperbolic law given as;

$$\sigma = \frac{1}{\alpha}\ln\left\{\left(\frac{Z}{A}\right)^{1/n} + \left[\left[\frac{Z}{A}\right]^{2/n} + 1\right]^{1/2}\right\}, \tag{19}$$

consequently, the lower the Zener-Hollomon parameter is, the larger the extent of flow softening becomes. Moreover, the higher the Zener-Hollomon parameter, the lower the power dissipation rate is.

Many investigations [74]–[76] have established the Arrhenius equation's flow stress of different metals and alloys during hot deformation. However, it is found that the effects of strain on the flow stress are not considered in Equations (15) and (16). Lin *et al.* [74] revised the models to describe the flow behaviour of 42CrMo steel over a wide range of forming temperatures and strain rates by compensation of strain and strain rate. Consequently, the Zener-Hollomon parameter should be compensated by multiplying both sides of Equation (16) by $\dot{\varepsilon}^{\frac{1}{3}}$. Then, the modified Zener-Hollomon parameter, Z', can be expressed as,

$$Z' = \dot{\varepsilon}^{4/3} exp\left(\frac{QR}{T}\right). \tag{20}$$

The proposed modifications were verified by Mandal et al. [77] and Samantaray *et al.* [78]. Mandal *et al.* modified the material constants by incorporating the fourth-order polynomial function of strains to predict the high-temperature flow-stress of a modified austenitic stainless steel [77].

2.4.6.1.4. The Johnson –Mehl-Avrami-Kolmogorov (JMAK) model

The type of curve shown in Figure 2-24 is typical of many transformation reactions and may be described phenomenologically in the constituent nucleation and growth processes. The early work in this area is due to Kolmogorov (1937), Johnson and Mehl (1939) and Avrami (1939) and is commonly known as the Johnson-Mehl-Avrami-Kolmogorov (JMAK) model [22].

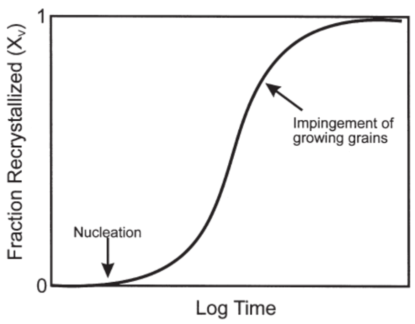

Figure 2-24. Typical recrystallization kinetics during isothermal annealing [22].

In this model, it is assumed that the nuclei are formed at a rate $\dot{N}$ and the grains growth into the deformed material at a linear rate $\dot{G}$. If grains are spherical, their volume varies as the cube of their diameter and the recrystallized fraction χ_v rises rapidly with time. However, the new grains eventually impinge on each other, and the rate of recrystallization will then decrease, tending to zero as χ_v approaches one. The number of nuclei dN appears in a time interval dt is less than $\dot{N}dt$ because nuclei cannot be formed where is already recrystallized. The number of nuclei which would have appeared in the recrystallized volume is $\dot{N}X_V dt$ and therefore the total number of nuclei dN' which would have formed, is given by:

$$dN' = \dot{N}dt = dN + \dot{N}X_v dt. \tag{21}$$

If the volume of a recrystallizing grain is V at time t, then the fraction of material, which would have recrystallized if the phantom nuclei were real, χ_{VEX} is known as the extended volume and is given by:

$$X_{\mathrm{VEX}} = \int_0^t V dN' \tag{22}$$

if the incubation time is much less than t, then

$$V = f\dot{G}t^3 \tag{23}$$

where f is a shape factor (4π/3 for spheres). Thus

$$X_{\mathrm{VEX}} = f\dot{G}\int_0^t \dot{N}t^3 dt \tag{24}$$

if $\dot{N}$ is constant then:

$$X_{\mathrm{VEX}} = \frac{f\dot{N}\dot{G}^3 t^4}{4} \tag{25}$$

During a time interval dt, the extended volume increases by and amount $d\chi_{\mathrm{VEX}}$. As the fraction of unrecrystallized material is $1 - X_{\mathrm{v}}$, it follows that $d\chi_{\mathrm{VEX}} = (1 - X_{\mathrm{v}})\, d\chi_{\mathrm{VEX}}$, or

$$dX_{\mathrm{VEX}} = \frac{dX_{\mathrm{V}}}{1 - X_{\mathrm{V}}} \tag{26}$$

$$X = \int_0^{\chi_{\mathrm{v}}} d\chi_{\mathrm{VEX}} = \int_0^{\chi_{\mathrm{v}}} \frac{d\chi_{\mathrm{v}}}{1 - \chi_v} = \ln\frac{1}{1 - \chi_{\mathrm{v}}} \tag{27}$$

$$X_{\mathrm{v}} = 1 - \exp(-\chi_{\mathrm{VEX}}), \tag{28}$$

combining Equations (25) and (28) for the particular case of three-dimensional growth:

$$X_{\mathrm{v}} = 1 - \exp\left(-\frac{f\dot{N}\dot{G}t^4}{4}\right), \tag{29}$$

where it can be written more generally in the form,

$$X_{\mathrm{v}} = 1 - \exp\left(-Bt^n\right), \tag{30}$$

where $B = \frac{f\dot{N}\dot{G}^3}{4}$ is often called the JMAK equation, and the exponent n in Equation (30), which we will refer to as the JMAK or Avrami exponent. The treatment assumed that the nucleation and growth rates remained constant during recrystallization. Avrami also considered the case in which the nucleation rate was not constant, but a decreasing function of time, $\dot{N}$ having a simple power law dependent on time. In this situation, n is dependending on the exact form of the function.

It should be noted that the essential feature of the JMAK approach is the assumption that the nucleation sites are randomly distributed. For this reason, the analytical modelling of recrystallization phenomena very often uses modified versions of the JMAK Equation (30). These models take into account different phenomena during hot working, such as Dynamic recrystallization (DRX), Meta-dynamic recrystallization (MDRX), Static recrystallization (SRX) and Grain Growth (GG) [79]. Furthermore, these models are often used for the processes simulation software and are discussed in the following sections.

2.4.6.2. Physical based models

The macro phenomenological models' material constants can be obtained by fitting and regressing experimental data. However, there is some potential deficiency in phenomenological models. Microstructure changes extensively during the hot and dynamic deformation process, and phenomenological models cannot accurately interpret, especially at high strain rate and temperature conditions. The focus in this section is to review the models considering dynamic recovery and dynamic recrystallization, which are described below.

2.4.6.2.1. Flow stress prediction: Hensel-Spittel constitutive model

Hensel and Spittel [80] proposed a constitutive equation to describe the rigid-plastic material flow stress. The Hensel-Spittel equation is defined as:

$$\sigma_{\mathrm{t}} = Ae^{m_1 T}\, \varepsilon^{m_2}\, \dot{\varepsilon}^{m_3}\, e^{\frac{m_4}{\varepsilon}}\, (1+\varepsilon)^{m_5 T}\, e^{m_7 \varepsilon}\, \dot{\varepsilon}^{m_8 T}\, T^{m_9}, \tag{31}$$

where T is the temperature given in Celsius, m_1 and m_9 define the material's sensitivity to temperature. m_5 term coupling temperature and strain and m_8 term coupling temperature and strain rate. m_2, m_4, and m_7 define the material's sensitivity to strain, and finally, m_3 depends on the material's sensitivity to the strain rate.

The Hensel-Spittel equation applies to viscoplastic behaviour to describe the relationship between strain, strain rates, temperatures, and stress bases. Moreover, it is temperature-dependent and takes strain hardening or softening phenomena into account. It also takes the strain rate of the material into account [81].

H-S model is highly used for theoretical and engineering analysis due to its higher prediction accuracy than the strain-compensated Arrhenius-Type equations [82].

2.4.6.2.2. A constitutive model considering dynamic recovery and dynamic recrystallization

Considering the two prominent coexisting phenomena during hot deformation: DRV and DRX, the model, considers each mechanism.

(1) Constitutive models considering dynamic recovery

According to the work hardening and dynamic recovery, the evolution of the dislocation density with strain (or time) during deformation is generally considered to depend on the following two components:

$$d\rho/_{d\varepsilon} = U - \Omega\rho, \tag{32}$$

where $d\rho/_{d\varepsilon}$ is the rate of increase of dislocation density with strain. U represents the work hardening, a multiplication term that can be regarded as constant concerning the strain; $\Omega\rho$ is the contribution to dynamic recovery through dislocation annihilation and rearrangement, and Ω is often called the coefficient of dynamic recovery [40], [83]. Integrating Equation (32) gives:

$$\rho = e^{-\Omega\varepsilon}\left(\frac{U}{\Omega e^{\Omega\varepsilon}} + \rho_0 - \frac{U}{\Omega}\right), \tag{33}$$

where ρ_0 is the initial dislocation density (when $\varepsilon=0$). Previous studies have shown that the effective stress is negligible compared to the internal stress at high temperature so that the applied stress can be related directly to the square root of the dislocation density, $\sigma = \alpha\mu b\sqrt{\rho}$ where α is the material constant, μ is the shear modulus; b is the distance between atoms in the slip direction [84]. In the steady-state condition, the dislocation can be obtained as:

$$\rho_{\mathrm{DRV}} = U/_{\Omega}. \tag{34}$$

Therefore, the flow stress during work hardening-dynamical recovery period under hot deformation can be given by the following expression in terms of the strain:

$$\sigma = \left[\sigma_{\mathrm{DRV}}^2 + \left(\sigma_0^2 - \sigma_{\mathrm{DRV}}^2\right) e^{-\Omega\varepsilon}\right]^{0.5}, \tag{35}$$

where σ is the flow stress, ε is the strain, σ_0 and σ_{DRV} are the yield stress and the steady-state stress due to dynamic recovery, respectively.

(2) Constitutive models considering dynamic recrystallization

The dynamic recrystallization phenomenon is more prominent at high temperatures and low strain rates. The volume fraction of dynamic recrystallization, χ_{D}, can be expressed as [85]:

$$\chi_{\mathrm{D}} = 1 - exp\left[-K_{\mathrm{d}}\left(\frac{\varepsilon-\varepsilon_{\mathrm{c}}}{\varepsilon_{\mathrm{p}}}\right)^{n_{\mathrm{d}}}\right] \qquad (\varepsilon \geq \varepsilon_{\mathrm{c}}), \tag{36}$$

where ε_{c} is the critical strain for occurring dynamic recrystallization. K_{d} and n_{d} are dynamic recrystallization parameters depending on chemical composition and hot deformation conditions.

Meanwhile, the progress of the dynamic recrystallization, X_{d}, can also be written as:

$$\chi_{\mathrm{D}} = \frac{\sigma_{\mathrm{DRV}} - \sigma}{\sigma_p - \sigma_{\mathrm{DRX}}} \qquad (\varepsilon \geq \varepsilon_{\mathrm{c}}), \tag{37}$$

where σ_{DRX} and σ_{p} are the steady-state flow stress due to dynamic recrystallization and peak stress, respectively.

Then, the flow stress during dynamical recrystallization period under hot deformation can be given by the following expression in terms of the strain and the steady-state flow stress:

$$\sigma = \sigma_{\mathrm{DRV}} - \left(\sigma_{\mathrm{p}} - \sigma_{\mathrm{DRX}}\right)\left\{1 - \exp\left[-k_{\mathrm{d}}\left(\frac{\varepsilon - \varepsilon_{\mathrm{c}}}{\varepsilon_{\mathrm{p}}}\right)^{n_{\mathrm{d}}}\right]\right\} \qquad (\varepsilon \geq \varepsilon_{c}). \tag{38}$$

This model was proposed by Lin *et al.* [86] for 42 Cr Mo Stainless steel. The proposed model combines work hardening with DRX in recrystallized volume fraction. However, independent parameters have to be determined through a material test. This feature results in complications for the application of the model. Theoretically, the atomic diffusibility and the driving force of dislocation migration are dependent on the temperature, and the dislocation density and the gradient of grain boundary energy are dependent on the strain rate. According to the creep equation, Liu et al. [85] thought peak stress is taken as the temperature and strain rate function. Since the DRX is a thermally activated process, the recrystallized volume fraction can be regarded as the function of strain through the Avrami equation. The recrystallized volume fraction mainly dominates the descending flow stress. So, the flow stress at different strains is regarded as the peak stress and the strain function. They proposed a new model to describe the dependence of the flow stress on various temperatures, strain rates and strains, and the new model is expressed as:

$$\sigma = \exp\left[\psi\left(\varepsilon - \varepsilon_{\mathrm{p}}\right)^{2} \ln \xi\varepsilon + \ln \sigma_{\mathrm{p}}\right]. \tag{39}$$

Accordingly, the peak stress σ_{p} can be written as a function of Zenner-Hollomon parameter, considering the definition of the hyperbolic law:

$$\sigma_{\mathrm{p}} = \frac{1}{\alpha} \ln\left\{\left(\frac{Z}{A}\right)^{1/n} + \left[\left(\frac{Z}{A}\right)^{2/n} + 1\right]^{1/2}\right\}, \tag{40}$$

therefore, the peak strain can be calculated from

$$\ln \varepsilon_{\mathrm{p}} = (\ln Z - B_1)/B_2. \tag{41}$$

This leads us to when the value of the strain is small, the accuracy of model prediction will decline if DRX does not occur.

2.4.6.3. Artificial neural network (ANN) model

The hot deformation behaviour of materials is usually described by the above-reviewed phenomenological or physical-based models. The deformation behaviours of the materials under elevated temperatures and strain rates are highly nonlinear, which makes the accuracy of the flow stress predicted by the regression methods low and the applicable range limited. However, neural networks can be related to artificial intelligence, machine learning, parallel processing, statistics, and other fields. The attraction to these models is that they are best suited to solve the most challenging problems by traditional computational methods. Artificial Neural networks can provide a fundamentally different approach to materials modelling and processing control techniques than statistical or numerical methods. One of the main advantages of this approach is that it is not necessary to postulate a mathematical model at first or identify its parameters.

Artificial neural networks (ANN) are a large class of parallel processing architectures that can mimic complex and nonlinear relationships by applying many nonlinear processing units called neurons. The relationship can be "learned" by a neural network through adequate training from the experimental data. However, it can only make decisions based on incomplete and disorderly information, generalize rules from those cases on which it was trained, and apply them to new cases.

The multilayer feed-forward network with back propagation (BP) learning is the most popular of all ANN models [40], [83]–[87]. The feed-forward back propagation neural network is composed of two neural network algorithms: (a) feed-forward and (b) back propagation. Of course, it is not necessary to always use 'feed forward' and 'back propagation' together, but this is usually the case.

For the predictions of flow stress of the hot deformed material, strain (ε), strain-rate ($\log \dot{\varepsilon}$) and temperature (T) are often used as the inputs of the model, while the flow stress (σ) is the output of the ANN model.

2.5. Recrystallization after deformation

The deformed structure contains a large amount of stored energy in the form of dislocations, making the deformed microstructure thermos-mechanically unstable. After or during deformation, softening processes like SRV, SRX or post-dynamic recrystallization (PDRX) is related to the level of accumulated strain. When dislocation densities have been reduced to the minimal value everywhere, no driving force exists anymore for these processes, and average grain growth proceeds to reduce the total surface energy.

2.5.1. Static recovery

Static recovery phenomenon competes with static recrystallization, as both are driven by the stored energy of the deformed state. Static recovery is defined as the decrease in density and change in the distribution of the dislocations and other defects during annealing. These changes do not involve sweeping the deformed material by moving high angle boundaries [88]. Interrupted strain, annealing temperature, and the nature of the material all influence static recovery. However, the material's stacking fault energy (SFE) is the most critical recovery factor. It determines the mechanisms that control the recovery rate: dislocation climb and cross slip [22]. The driving force for dislocation climb or cross slip is decreased stored energy. Moderate to low SFE metals polygonise with more effort than high SFE, and thus cell structure is less obvious. After deformation, mechanical and microstructural changes during recovery in SSAS are subtle and occur on a small scale, which is generally ignored [22].

2.5.2. Static recrystallization

SRX occurs when a material is deformed to a strain lower than the critical strain for DRX at the corresponding temperature but with sufficient stored energy to drive the recrystallization when subsequently annealed.

New SRX grains usually nucleate preferentially where the highest local deformation is, i.e. on pre-existing grain boundaries, deformation bands, and inclusions. The nucleation process is thermally activated, and detectable incubation time is required. Three nucleation mechanisms have been proposed for SRX: strain-induced grain boundary migration, subgrain growth and subgrain coalescence [22].

When a high-angle boundary is formed, it can move towards the deformed material. However, the migration speed is sensitive to impurities, the structure of the final grains and the orientation relationship between the growing grains and the deformation matrix [88].

Many experimental observations have shown that SRX kinetics be described approximately by the JMAK model, which often appears in the form of:

$$\chi = 1 - exp\left(-0.693\left(\frac{t}{t_{50}}\right)^{n}\right), \tag{42}$$

$$t_{50} = A\dot{\varepsilon}^{m}\varepsilon^{p}d_{0}^{q}exp\left(\frac{Q}{RT}\right), \tag{43}$$

where χ is the recrystallization fraction or softening fraction (%), t time (second), n is the Avrami exponent, t_{50} is the time for 50% softening (second), $\dot{\varepsilon}$ is the strain rate (s^{-1}), d_0 is the initial grain size (μm), Q is the apparent activation energy of SRX (J/mol), A, m, p, q are the material-dependent constant. According to Jonas *et al.* [89], the driving pressure and the recrystallization behaviour are dependent on Z. It should be noted that the expression for t_{50} can be rewritten to include Z, which leads to:

$$t_{50} = AZ^{-m}d_{0}^{q}exp\left(\frac{Q}{RT}\right). \tag{44}$$

The accumulated strain, initial grain size, strain rate, and temperature have a pronounced effect on the static recrystallization kinetics. On the other hand, the chemical composition of the material also significantly influences the kinetics of SRX.

2.5.3. Post-Dynamic recrystallization

Whenever the critical strain for DRX ($\varepsilon_{\mathrm{cr}}^{\mathrm{DRX}}$) is exceeded, recrystallization nuclei are present in the material. If the strain stop but the annealing continues, the nuclei growth with no incubation period into the heterogeneous, partly dynamically recrystallized matrix. This phenomenon is known as metadynamics recrystallization or post dynamic recrystallization [90].

Compared to the extensive literature available regarding the work on SRX, much fewer systematic studies have been conducted for the static restoration mechanisms operating after DRX at high strains. McGill *et al.* investigated the post-dynamic softening of austenite. They proposed a mechanism involving three restoration processes, including SRV, PDRX and SRX, based on further metallographic examination on polycrystalline copper [91]–[93]. The recrystallization nuclei formed during deformation, which grew during straining, continue when the deformation is interrupted. PDRX proceeds more quickly than classical SRX because no incubation time is needed. However, full softening cannot be obtained through sole PDRX, and subsequent classical SRX provides further softening until the softening is completed. The corresponding curve representing this process is characterized by a plateau caused by the incubation time of SRX.

Sakai *et al.* [92], [94] later researched the above subject using a nickel alloy and austenitic steel and provided a detailed description of the above restoration processes. A further softening mechanism, called post dynamic recovery (PDRV), occurs in the non-recrystallize grains either by PDRX or SRX because their density is too low at the onset of recrystallization.

The effects of the four softening mechanisms can be distinguished for the three different categories of grains in the dynamic recrystallization structure described above, which is summarized below in Figure 2-25, considering three stages. These dynamically formed nuclei grow as PDRX until other growing grains impinge on them in the first stage. At the same time, PDRV or SRV softens the moderate and fully work-hardened grains. Then, after a certain incubation time, classical SRX occurs in stage II in the fully work-hardened regions where the dislocation density is still above the critical value for SRX. This continues until the statically formed nuclei impinge with each other, as well as with PDRV and PDRX grains. Finally, classical grain growth further contributes to the softening process in stage III after recrystallisation.

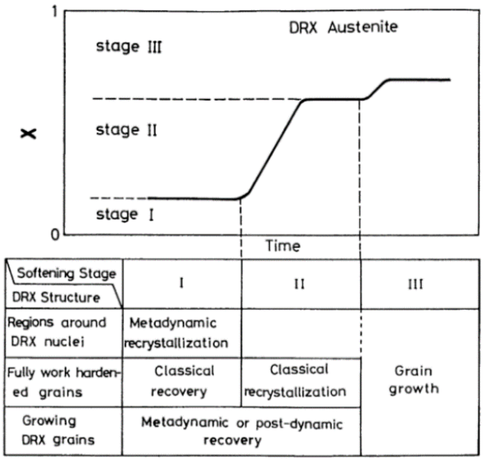

Softening Stage DRX Structure	I	II	III
Regions around DRX nuclei	Metadynamic recrystallization		Grain growth
Fully work harden-ed grains	Classical recovery	Classical recrystallization	
Growing DRX grains	Metadynamic or post-dynamic recovery		

Figure 2-25. Schematic illustration shows the relation between the softening stages and the restoration process operated mainly after DRX [94]**.**

Hodgson *et al.* [95]–[97] have studied in more detail the different mechanisms at work after hot deformation in particular and more recently investigated the mechanism of austenite softening after full DRX [98], [99] (Figure 2-26 a)). The initial softening observed at an early stage of post-deformation annealing is due to the rapid growth of the dynamically formed nuclei (MDRX or PDRX). According to Jonas *et al.* [90]–[93] and Sakai *et al.* [92], [94]), these have a high migration driving force because of their relatively low dislocation density compared to adjacent grains (Figure 2-26 a), b)). Which leads to the formation of dislocation-free regions behind the moving boundaries (Figure 2-26 b)). Furthermore, the progressive annihilation of sub-boundaries within DRX grains through the operation of dislocation climb ultimately leads to the formation of nearly dislocation-free grains and reduction of the migration rate of the grain boundaries (Figure 2-26 c and d).

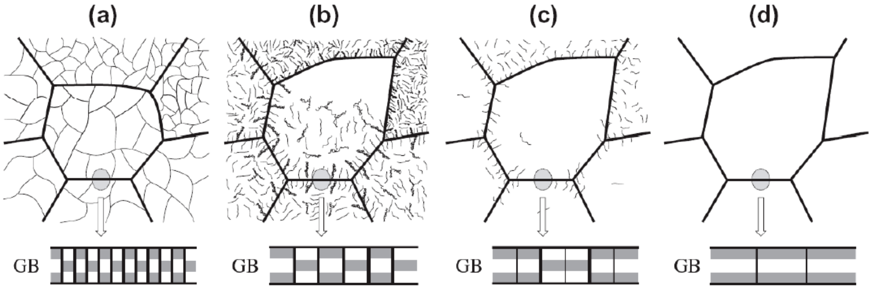

Figure 2-26. Schematic representation of the proposed post-dynamic softening mechanism: (a) the initial DRX state, (b) rapid grain boundary migration and disintegration of sub-boundaries, (c) removal of dislocations from the grain interiors, (d) formation of dislocation-free grains. The insets in (a-d) illustrate a progressive loss of visibility of extrinsic dislocations within the grain (GB) structure [99]**.**

Since the dislocation density decreases with annealing time, the driving force for the grain boundary migration also decreases. As a result, most of the pre-existing DRX grains were found to change in size and become dislocation-free rather than replaced by newly formed grains during post-deformation annealing [99].

The significant difference between SRX and PDRX lies in their kinetic dependencies. PDRX is strongly dependent on strain rate, slightly dependent on temperature and composition, and almost independent of strain. SRX, on the other hand, is primarily affected by temperature, strain and grain size and is a weak function of strain rate. Roucoules *et al.* [96] proposed that all the nuclei are present at the end of the peal strain, and further deformation does not lead to any nuclei, which explains why softening is strain independent at strain beyond the peak. However, a dispute still exists over this topic.

2.5.4. Factors affecting the recrystallization behaviour after hot deformation

The influence of temperature strain rate has been studied as an essential factor for the initiation of PDRX.

2.5.4.1. Effect of stop strain

Djaic and Jonas [90] studied the static softening by interrupted compression tests on 0.68% C steels at 780ºC. As illustrated in Figure 2-27, at the slightest accumulated strain (Figure 2-27 a)) in the work hardening region of the flow stress, static recovery is the sole mechanism that leads to about 30% of the softening. When deformation stops on the flow curve between peak and steady-state stress, DRX is followed by PDRX, static recovery, SRX, and the softening curve is characterized by two inflexion plateaus (Figure 2-27, b)). Static recovery and PDRX are the responsible mechanisms for softening the steady-state region if the stop strain goes further.

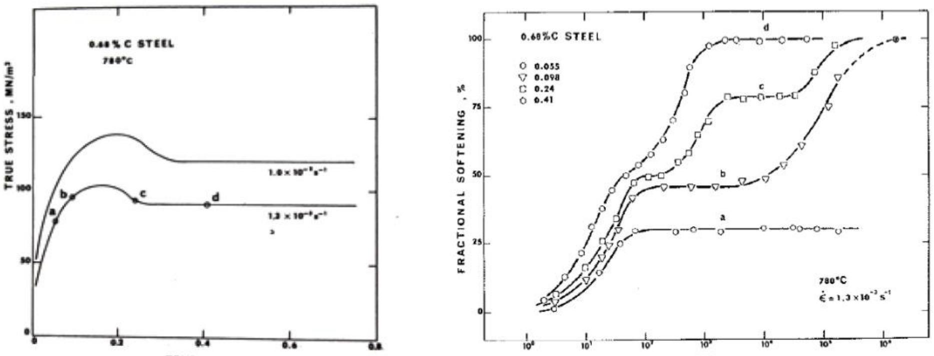

a) b)

Figure 2-27. a) Flow curves for AISI C1060 carbon steel compressed at 780 ºC, the one deformed at 1.3x10^{-3}s^{-1} was used to study softening in b), letters a, b, c, d in the represent the interruption strains, b) Effect of strain on the static softening of a 0.68%C steel [90].

The fractional softening was measured by Dehghan-Manshadi *et al.* [100] as a function of un-loading time for different applied strains (all of them are beyond the critical strain for DRX) and for a given deformation condition (same temperature and strain rate). Figure 2-29 a) shows that the softening follows a typical sigmoidal behaviour for all the applied strains. Di Schino and Kenny also obtained similar shapes for AISI 316 stainless steel [100], which contradicts the observation made by Djaic and Jonas [90]. Figure 2-29 b) shows that minor strains produce bigger grain sizes at the same heating time or softening fraction. The same tendency has also been reported by other research works [100], [101], [95]. The decrease and then increase in the average grain size with increasing un-loading time indicates the formation of new small SRX and PDRX grains and the growth of these grains, respectively.

For classic SRX, an increase in the applied strain can increase the SRX kinetics by increasing the number of nucleation sites and leading to a shorter incubation time to initiate SRX [92], [102].

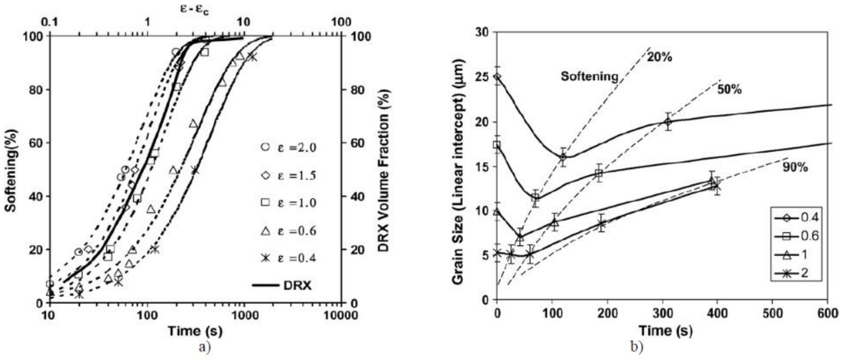

a) b)

Figure 2-28. a) The average grain size (linear intercepts) as a function of un-loading time at different strains, for deformation at 900 ºC and a strain rate of 0.01 s^{-1}, b) The effect of applied strain on the softening fraction at 900 ºC and a strain rate of 0.01 s^{-1} [90].

Therefore, the discussion regarding the recrystallization kinetics after hor deformation is still open. More experimental data are needed to clarify the softening fraction behaviour and further understand the mechanism.

2.5.4.2. Effect of temperature and strain rate

Temperature is found to profoundly influence SRX kinetics [103] by affecting the nucleation rate and the mobility of grain boundaries. Strain rate also promotes the kinetic of SRX due to the reduced extent of dynamic recovery at higher strain rates. However, the strain rate effect on SRX kinetics is usually less significant than temperature [104].

The weak dependence of the softening rate of PDRX on temperature was found for C-Mn steel [95], HSLA steels [96] and carbon steels [105]. However, a stronger relation between temperature and PDRX kinetics was found for 304 austenitic stainless steel [104] and carbon steel [53]. This effect is described as the increasing mobility of the grain boundaries during both SRX and SRV. Dehghan-Manshadi *et al.* [106] obtained the time for the 50% softening (t_{50}) using 304 austenitic stainless steel and showed that softening kinetics increased with temperature (Figure 2-29 a)).

The effect of temperature strain rate on the softening of PDRX was also analysed by Cho *et al.* [107] on 304 austenitic stainless steel, who obtained similar conclusions as mentioned above.

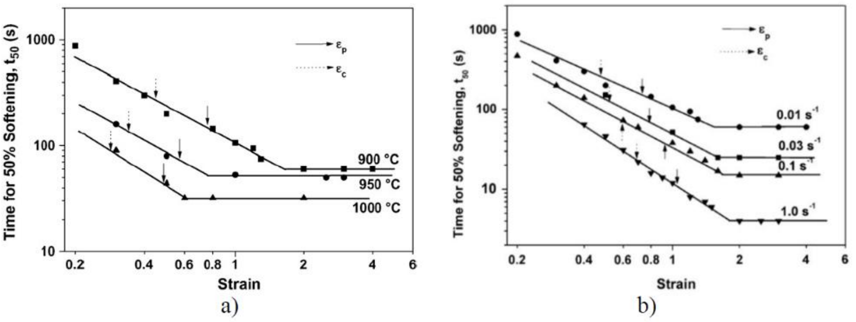

a) b)

Figure 2-29. a) The time for 50% softening after deformation at different temperatures and a constant strain rate of 0.01 s^{-1} b) The time for 50% softening after deformation at different strain rates as a function of applied strain [106]**.**

Besides the softening kinetics, grain size after hot deformation is also affected by temperature and strain rate. For example, it has been observed that the PDRX grain size decreases with decreasing temperature and increasing strain rate.

2.5.4.3. Effect of initial grain size

As new SRX grains usually nucleate on the pre-existing grain boundaries, initial grain size naturally affects the kinetics of SRX by changing the number of nucleation sites. It has been shown that initial grain size has a pronounced effect on the kinetics and microstructure of SRX [108], [109]. Sellars [110] obtained Equations (45) and (46) for the time to 50% recrystallization (t_{50}) and for recrystallized grain size (d_{rex}) based on the analysis of published data on C-Mn steels. The dependence of initial grain size is evident in the equations:

$$t_{50} = 2.5x10^{-19} d_0^2 \varepsilon^{-4} Z^0 exp\left(\frac{300000}{RT}\right), \tag{45}$$

$$d_{srx} = 0.5 d_0^{0.67} \varepsilon^{-1} Z^0, \tag{46}$$

for PDRX, which consists of the growth of DRX nuclei, the effect of initial grain size on its kinetics is expected to be lower.

Lin and Chen [111] found in 42CrMo steel that final grain sizes rapidly increases with increasing the initial grain sizes when they are below a critical value. If the initial grain size is higher than this value, no influence persists on the final grain size. The considerable effect of initial grain size on both the strain-dependent and independent strain regions was observed by Dehghan-Manshadi *et al.* [56].

To summarize, it is generally accepted that initial grain size will affect both the kinetics and microstructure of SRX. On the other hand, it is unclear whether or not it influences PDRX.

2.6. Critical analysis of literature review

This final section critically argues the information from the literature review and sets the knowledge gap for the forthcoming investigation.

2.6.1. Existing models for recrystallization

According to the literature, constitutive models are divided into three main categories: phenomenological, physical-based, and ANN. After an exhaustive overview of the pros and cons, this project focuses on the phenomenological models based on empirical observations, which use fewer material constants, are easily calibrated and modified depending on the process conditions. Some of the most widely used models are the Johnson-cook and Arrhenius equations which described the relationship between strain rate, flow stress and temperature. However, the effects of strain and flow stress are not considered in the Arrhenius, and coupling effects of strain, temperature, and strain rate are omitted in the original JC model.

Therefore, it is critical to determine the microstructure evolution based on state variables: strain, strain rate, and temperature to obtain an accurate model. To do so, the transformation kinetics were described by the Johnson-Mehl-Avrami-Kolmogorov (JMAK) phenomenological model since the 40s, and many researches [113] have contributed to extending the applicability range of the JMAK model. It has been widely used to predict the kinetics and grain size of DRX because it gives acceptable results compared with semi-empirical and mesoscopic models.

The adaptability and accuracy of the JMAK model for similar cases to the Alloy 28 make it the model of choice for the current investigation. In the following section, the experimental plan to obtain the material parameters for the model implementation is reviewed.

2.6.2. Experimental investigation on recrystallization of SASS.

Many studies have been carried out on mechanical and microstructural aspects of the DRX progression. In cubic materials, the two basic deformation methods are slip and twinning and the most significant material respecting the choice of method is the stacking fault energy [22]. When the SFE is high, the dissociation of a full dislocation into two partials is energetically unfavourable, and the material deform either by dislocation glide or cross-slip. On the other hand, lower SFE displays wider stacking fault energy and dislocations mobility decreases. The literature classifies the studied Alloy 28 as a SASS that presents a low value of SFE; consequently, its leading restoration mechanism is dDRX under a wide range of deformation conditions, so the focus will be on understanding the mechanism, starting with the critical conditions on the initiation of DRX.

To evaluate the onset of DRX, several methods have been developed and recently reviewed by Castro *et al.* [15]. Above all, the Poliak and Jonas method [35], [44], also named the second derivative criterion, is the most accurate in many cases and suitable for the current process. According to SDC, the onset of DRX can be detected from an inflection point in the strain-hardening rate as a function of flow stress. Therefore, the first step is to design hot compression tests whose deformation parameters suit the process, and then the stress-strain curves are obtained.

However, as shown by Bambach *et al.* [41], [52], a flow stress model that incorporates DRX suffers from inconsistencies with the SDC when it is not sufficiently many times differentiable at the critical point. Then, inconsistencies occur when JMAK kinetics are used to predict the DRX kinetics in the current work, as studied by Imran *et al.* [48]. Therefore, following Imran studies, the stress-strain curves should be treated to agree with the SDC; this methodology is explained in Section 4.

Several factors affect the recrystallization behaviour, and the most important are temperature, strain rate and initial grain size, whose influences affect the flow stress curves. When single peak flow stress curves are observed, the deformation occurs at low temperature and high strain rate. In contrast, multiple peaks appear for a very low strain rate, relatively high temperature, and small grain size. Therefore, when the conditions for the hot working process are set, the initial grains size plays a crucial role in the development of DRX.

As shown in Section 4, the Alloy 28 used is cast raw material after thermal treatment, which presents a coarse grain size. Therefore, the focus is to study the recrystallization using the coarse grain presented after casting. Several authors have been investigating this case for the cases of 306 and 307 [58], [59], but there is no extensive research on hot working using as cast as an initial state.

When it comes to Alloy 28, the information present in the literature mainly uses the wrought material as the initial material state and minimum research has been developed using coarse grain. Then, some aspects need further investigation:

a) Determine the critical condition for the onset of DRX since it has been reviewed that the initial grain size highly influences the recrystallisation development. Therefore, a compression test needs to be developed at different temperatures and strain rates.
b) Study the microstructural evolution during hot working and obtain its recrystallization parameters. Then, compare them to the exiting data from wrought material, and observe the influence of the initial structure.

c) Obtain a microstructural model's material parameters that consider a coarse initial microstructure.

The focus on the thesis related to the founded knowledge gap is in the following section.

2.7. Focus of the thesis

According to the above discussion, the literature lacks accurate models that predict microstructure evolution under multi-pass conditions using coarse grain as initial material for the Alloy 28 designed for industrial applications.

With these remarks in mind, a JMAK modified model is used to describe the material evolution by obtaining the material parameters and process variables using the experimental set-up described in Section 3, which results are presented in Chapter 4. Then, the model is implemented for the industrial process using FORGE® simulation software and validated with a reference model, as described in section 5. The conclusions and future work are then exposed in Section 6.

2.8. Summary

This literature review considers two aspects of the microstructural evolution during hot working: the kinetics that drives recrystallisation and the DRX available models.

The initial behaviour during a deformation process is explained in Section 2.2, and then the nucleation mechanisms that rule each phenomenon are summarized in Section 2.3. then WH, DRV, and DRX in Section 2.4 and Post-deformation recrystallization (PDRX) in Section 2.5. are reviewed to understand the process and condition for each phenomenon to occur.

In section 2.4.6. the three categories of models to describe the material evolution are summarized, focusing on the phenomenological model used in this work, the JMAK.

Finally, a critical review of the literature is done, where the knowledge gap was set, followed by the thesis's focus, where the work developed in forwarding sections is summarized.

3. METHODOLOGY

This chapter summarises the methodology used in this project, from the as-cast to the forged material through the pre-forge thermal treatment. The complete hot compression test is developed for model implementation, and the recrystallization measurements are explained in depth.

3.1. As-cast characterization

The ingot used for industrial processes is used for the as-cast characterisation. The billet is divided into five sections, as shown in Figure 3-1. Three areas are distinguished: Edge (E), Middle (M) and centre (C).

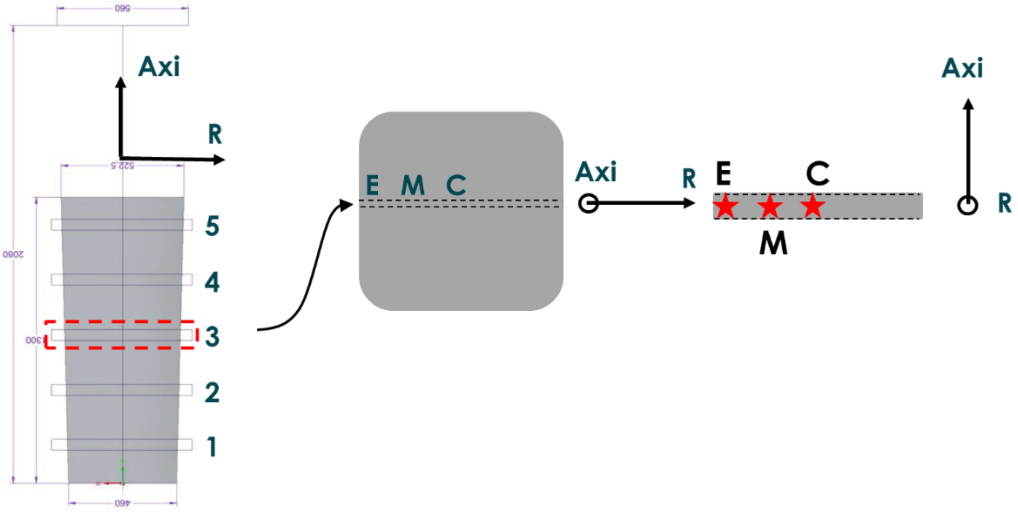

Figure 3-1. Schematic view of section 3 for the as-cast billet.

A round-up on the microstructure is made in the relative orientations axial and radial, as shown in Figure 3-2. The characterisation is focused on the radial axis, where the microstructure presents heterogeneity. On the other hand, in the axial direction, the microstructure is homogeneous, so, in the following sections, slice 3 (highlighted in red in Figure 3-1) is used as the initial material.

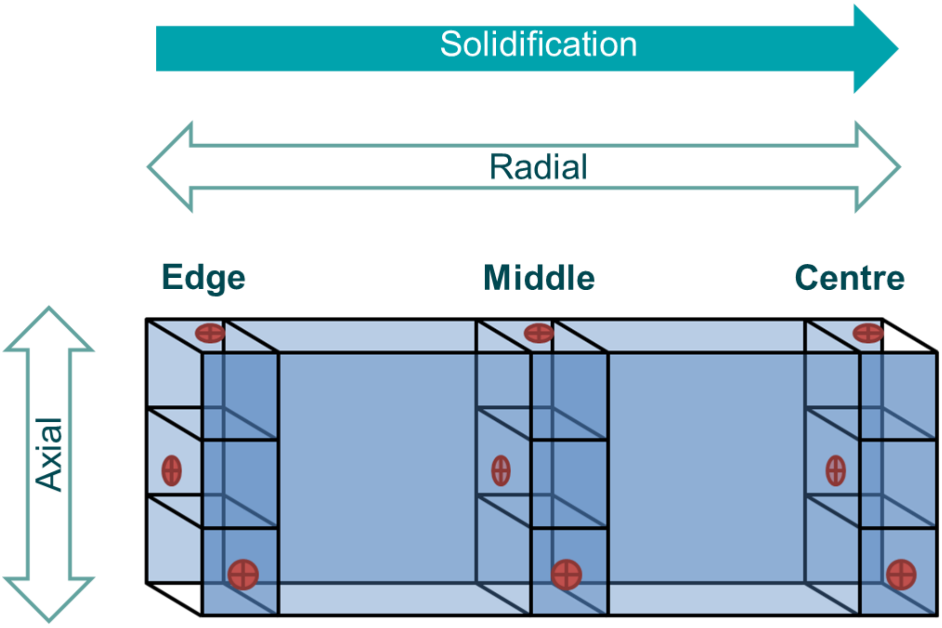

Figure 3-2. Orientations on the Billet regarding the axial and radial direction and the solidification gradient.

3.1.1. Microstructural characterization

For metallographic observations (Figure 3-3 a)), the samples are cut by an abrasive saw and mounted in a 32 mm conductive resin plate to be prepared for microstructural examination.

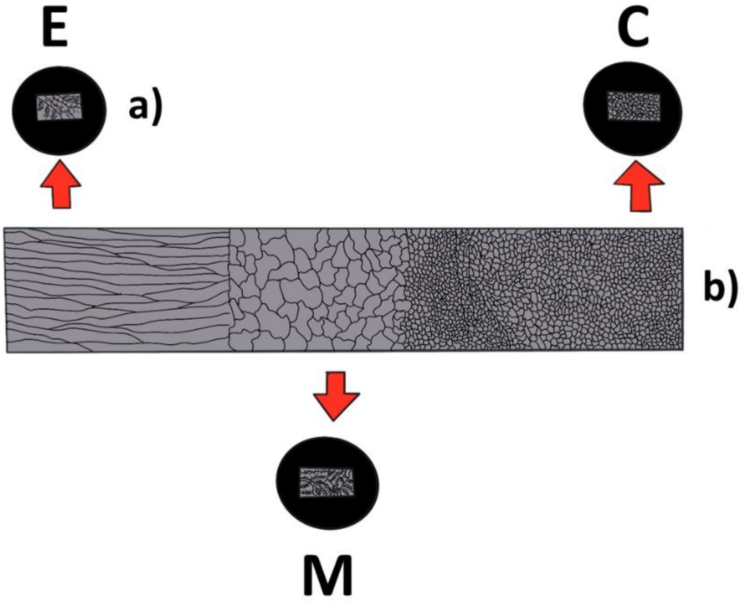

Figure 3-3. Schematic representation of a) microstructural characterization of the As-cast billet, b) macrostructural characterization of the as-cast billet.

Standard metallographic preparation is conducted, as shown in Figure 3-4. The samples are ground in three steps using an automatic grinding machine, followed by three polishing, using a diamond paste of 3 μm and 1 μm, finishing with an alumina suspension of 0.3 μm. Each plate is maintained for 5 minutes applying 20 N in an automatic grinding machine. After the grinding process, the samples are etched using a chemical solution of FeCl face-up until the microstructure reveals on the surface.

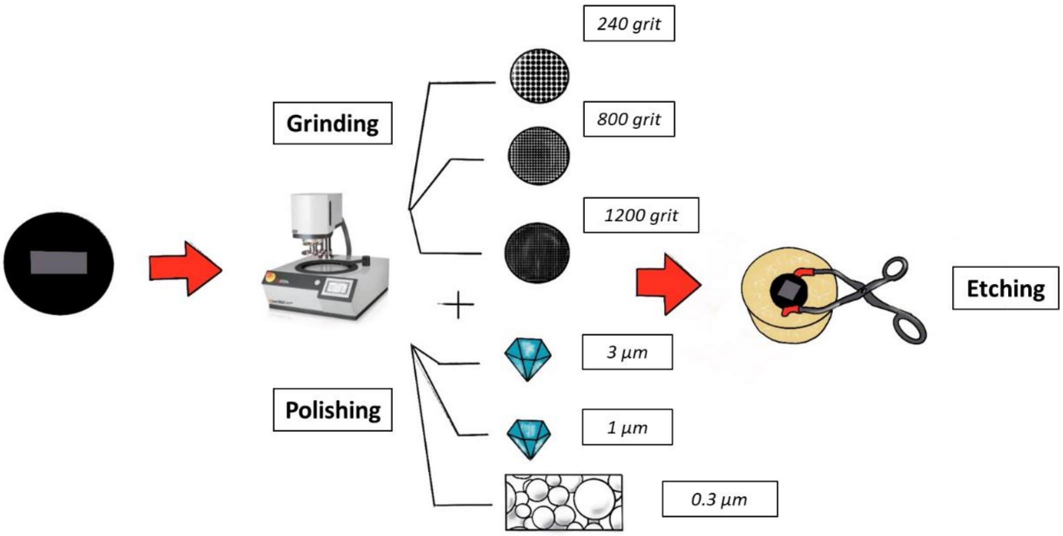

Figure 3-4. Standard metallographic preparation.

To reveal the macrostructure (Figure 3-3 b)), a longitudinal section of slice 3 is cut using a wire EDM cutting. Next, the surface is ground and polished using an EM® Rotaflex® until the surface shows shining. Finally, the surface is etched using "royal water" (HNO_3 and HCl in proportion 3:1).

3.1.2. Compositional characterization

This characterization is divided into two stages: analysing the average percentage along the radial direction and studying the presence of precipitates and microsegregation.

The average composition percentage is obtained through Inductively Coupled Plasma (ICP) in the three studied areas: centre, middle, and edge. ICP analysis utilizes a plasma torch to vaporize fine droplets of the sample. Depending upon the ICP analysis test method, the atomic emission or ion mass is used to quantify the elements present in the sample.

Energy-dispersive X-ray Spectroscopy (EDS) is used to study the composition gradient between the dendritic and interdendritic space, along with the appearance of precipitates. The samples are prepared by standard metallography (Figure 3-4) and examined through a Scanning Electron Microscope (SEM). This study aims to determine the compositional deviations between the dendrite and the interdendritic space.

3.2. Pre-forge thermal treatment

Before forging, thermal treatment is necessary to refine the as-cast grains and eliminate the microsegregation during the industrial process. Due to the impossibility of obtaining samples from the billet after the thermal treatment, the industrial's heating cycle shown in Figure 3-3 is reproduced in the laboratory.

The hot and cold forming software FORGE® is used to determine the heating time of the samples to be as representative as possible to the actual process. These times are resumed in Figure 3-1.

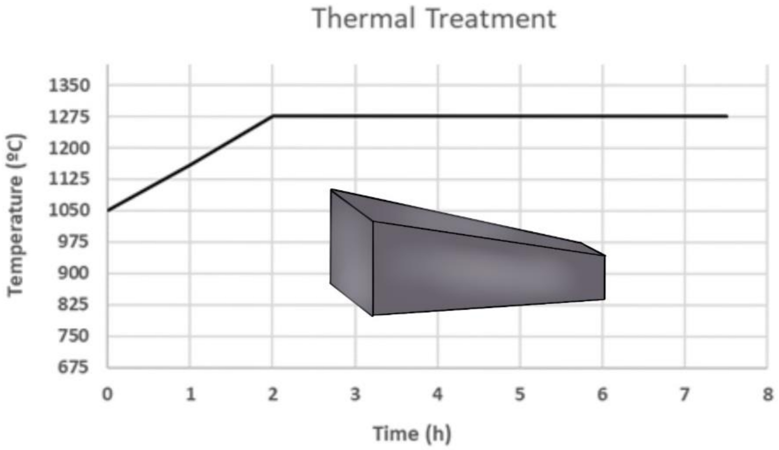

Figure 3-5. Furnace cycle for the Alloy 28 Industrial process.

Temperature	Centre	Middle	Edge
1250 ºC	3 h	4 h	5 h

Table 3-1. Exposure times to target temperature in the ingot.

Three cylindric samples (Figure 3-6) are obtained using a wire EDM cutting machine to perform the treatment in the laboratory, using a Hobersal furnace (Max. temperature 1300 ºC). The samples are heated for two hours from 1025 ºC up to 1250 ºC and then are maintained at the holding times in Table 3-1. The samples are quenched in water after the heating to preserve the microstructure.

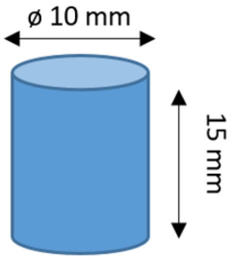

Figure 3-6. The geometry of the samples.

The samples are examined by optical microscopy (Figure 3-4). Using a Leica Microscope, the microstructure is observed, and the grain size is measured according to the ASTM E1181-02 for large grains. In addition, EDS examinations are conducted to observe if the segregation identified in the as-cast samples disappeared. The compositional maps obtained are commented in Section 4.

3.3. Forged bar characterization

Both micro and macrostructures are examined following both ways explained in Section 3.1.1. The samples are obtained from the edge, middle and centre of two areas of the rounded bar: the Top feeder corresponding to area 1 and the Foot corresponding to area 5 of the ingot (Figure 3-1). The schematic representation of the studied areas for the rounded bar is shown in Figure 3-7.

Figure 3-7. Schematic representation of the rounded bar.

Due to the smaller grains size, in comparison with the As-Cast, the grain size is obtained using the UNE-EN ISO 643 standard

A macroscopic examination was done to observe the grains distribution in the bar section, both top feeder and foot, as shown in Figure 3-8, using the methodology described above for the as-cast.

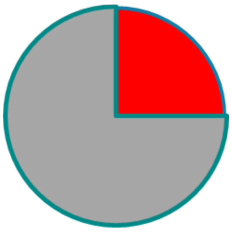

Figure 3-8. Section of the Round Bar for the macroscopic analysis (Red).

3.4. Hot compression test

Hot compression test is one of the most extended methods to study recrystallization in metallic materials because allows playing with multiple variables, i.e. strain, strain rate, temperature, holding time, compression steps.

Hot compression tests are performed at TU Graz using a Gleeble 3800® machine up to a strain of 0.8 at the strain rates and temperatures shown in Table 3-2. Fifty samples are machined by EDM from the middle section of the as-cast billet (Figure 3-6), and the thermal treatment described in Section 3.2 is applied. The MR is chosen because the edge suffers from debarking after forging, and the centre is more susceptible to present physical defects even though it has been seen that the precipitates dissolved after the thermal treatment. To prepare the samples for the test, two consumable thermocouples type K are welded in each sample's middle using spot welding, as shown in Figure 3-9.

Hot compression	
$\varepsilon = 0.8$	
T (ºC)	$\dot{\varepsilon}$ (s^{-1})
1100	0.1
1200	1
1250	10

Table 3-2. Condition for hot compression test.

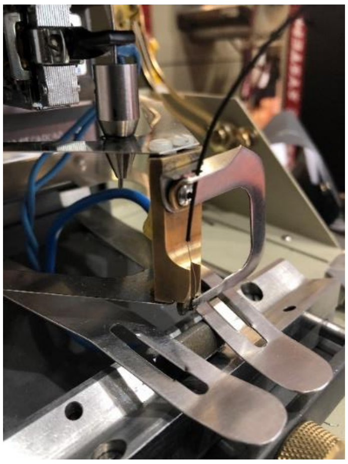

Figure 3-9. Spot welding machine.

Set-up is shown in Figure 3-10, where the sample is placed horizontally between dies, and thermocouples are engaged to the Gleeble. For lubrication purposes, tantalum and graphite foils are placed between the samples and the dies. A quick quenching is necessary to preserve the microstructure after the deformation, so a water spreader device is used when deformation is completed.

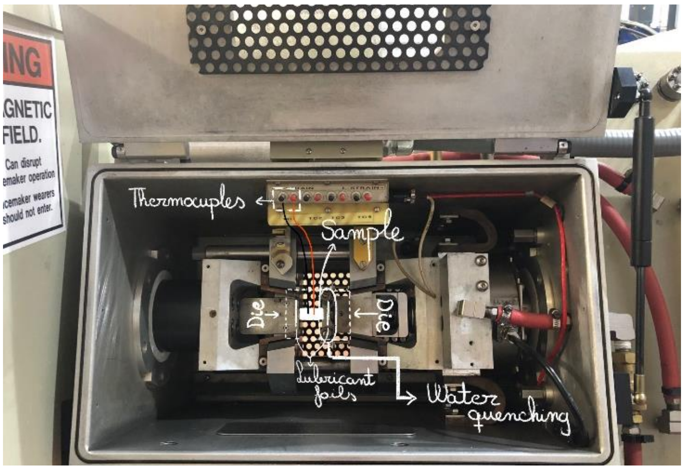

Figure 3-10. Hot compression experimental setup.

The samples obtained after the test are prepared for recrystallization measurements presented in the following section.

3.4.1. Recrystallization measurements

Optical microscopy and EBSD measurements are used to obtain the deformed samples recrystallisation fraction and grain size. Each sample is cut along the longitudinal axis from the hot compression test, and the middle section is examined, as shown in Figure 3-2.

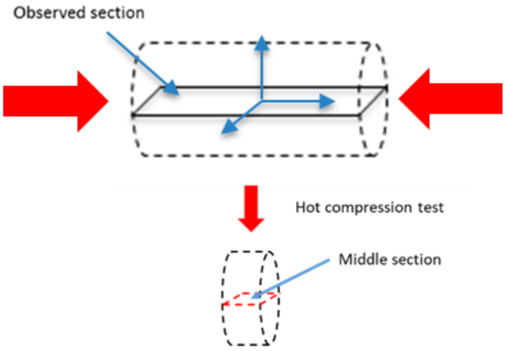

Figure 3-11. Representation of the sectioned samples from the Hot compression samples.

For EBSD measurements, preparation is critical. The compression test samples are cut on the transversal section by an abrasive saw and are mounted in conductive resin (diameter 1)) and then, the standard preparation is shown in Section 3.1.1 (Figure 3-4) is performed, skipping the etching step. Instead, the samples are polished by vibration (60 HZ) using an Aluminium 0.01 µm suspension between four and six hours. For EBSD measurements at SEM microscopy, five areas are selected from each sample to obtain representative results. The conditions for the analysis are:

- Voltage: 30 eV.
- Step size: 7 eV.
- Aperture: 3.
- Beam mode: Between 2x2 and 4x4.
- Gain: 10.
- Step size: Between 2 and 0.7.
- Analysis time: Between 2 and 12h.

For optical microscopy, the preparation shown in Figure 3-4 is carried out in a sample of 32 mm using ½ A etchant (120 ml water, 100 ml hydrochloric acid and 10 ml nitric acid).

3.4.1.1. Recrystallized grain size

The recrystallized grain size is obtained from the EBSD maps. The data acquisition software AZTEQ obtains the files treated in Channel 5 software for misorientation analysis. The grain orientation spread (GOS) map was calculated using the Tango extension for Channel 5 software of all the maps obtained. The average orientation angle is defined first as the value of 15° for the studied case. As reviewed in Section 2, during DRX, the recrystallized grains are small and usually with an equiaxed shape, while original deformed grains are elongated in deformation. Therefore, the spread is obtained by comparing the deviation between each point's orientation in the grain with the average orientation angle, which leads to the following criteria [112] and shown in Figure 3-12:

- 1º to 2º => DRX defects free grains.
- 2º to 15 º => LAGB (grains recrystallized in the process of growing).
- > 15º => HAGB (non-recrystallized/deformed grains).

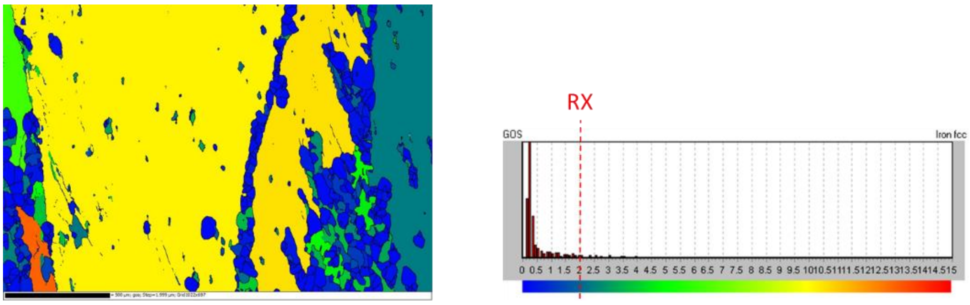

Figure 3-12. Acquisition of the recrystallized limit using GOS analysis.

After the GOS filter, a recrystallized grain size is obtained, but for the case of study, the GOS analysis is unprecise. Then, a second filter by grain size in the grains over the GOS value is necessary to obtain the recrystallized grain size.

3.4.1.2. Recrystallization fraction

From the analysis explained in the previous section, the Recrystallized fraction is calculated using Equation (47):

$$\chi_{DRX} = \frac{A_{DRX}^{i}}{\sum_{I=1}^{i=n} A_{DRX}^{i}}, \tag{47}$$

where n is the number of grain under the GOS limit, and the size filter explained previously and A_{DRX}^{i} is the area of each recrystallized grain. Although, it is necessary to complement the EBSD analysis with optical microscopy (OM) due to the large grains (Figure 3-13), to obtain an accurate measurement of χ_{DRX}.

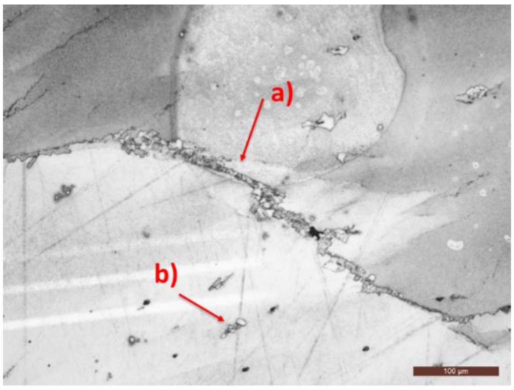

Figure 3-13. Detail of microstructure of large grains and recrystallized areas located in: a) Grain boundaries; b) Hetegoneous nucleation.

For OM, half of each sample is prepared by standard preparation (Figure 3-4). The recrystallized area appear as small grains gathered along the grain boundaries (Figure 3-13 a)) of the large deformed grains and from heterogeneous nucleation (Figure 3-13 b)). 70 to 80 micrographs from each sample are taken, so the recrystallized areas can be differentiated and coloured precisely in black to create a contrasting image. The non-recrystallized areas are presented in white, as is shown in Figure 3-15.

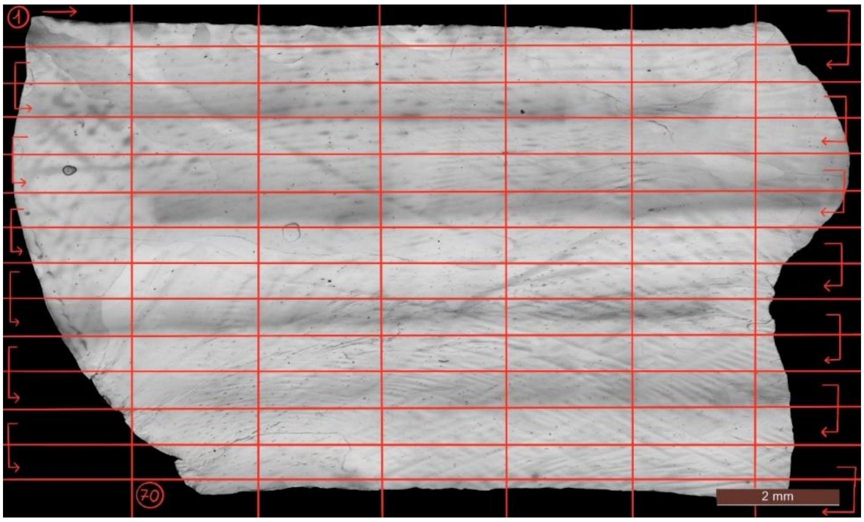

Figure 3-14. Optical microstructure from the hot-working sample.

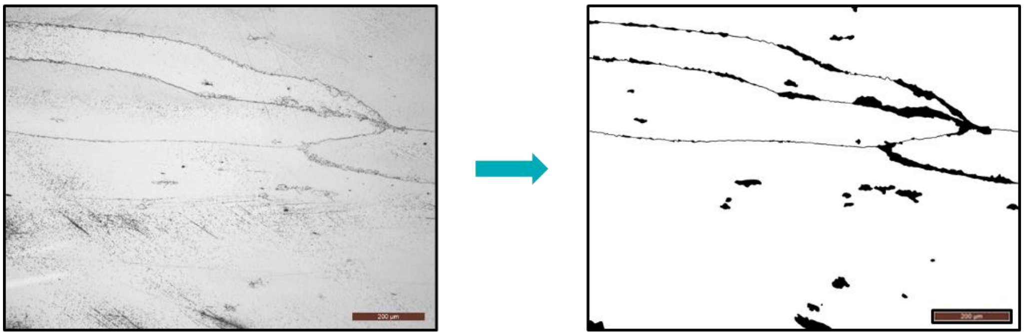

Figure 3-15. Contrast image acquisition of area 31.

The contrasted picture is then treated with the software Image J used to process and analyses scientific images. As shown in Figure 3-16, the threshold tool is used to obtain the percentage of recrystallized grains in the picture. This analysis is performed in every picture taken from the sample, and the average percentage is obtained.

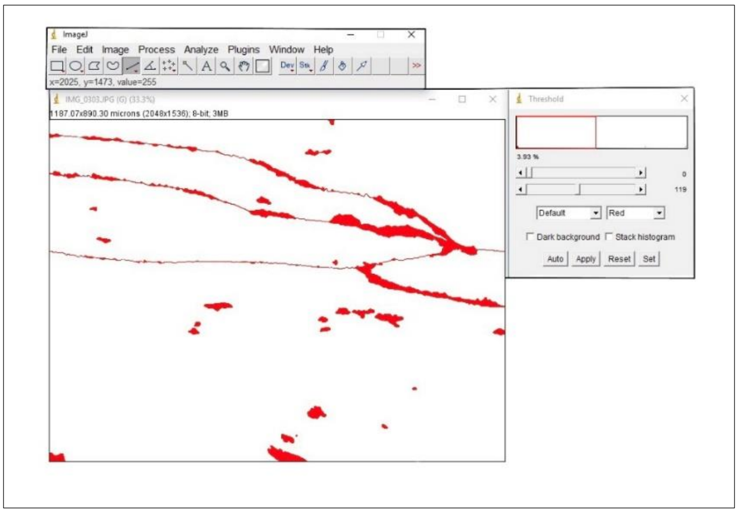

x=2025, y=1473, value=255

1187.07x890.30 microns (2048x1536); 8-bit; 3MB

3.93 %

0

119

Figure 3-16. Application of Image J to obtain the recrystallized area.

3.5. Summary

The changes in mechanical behaviour during hot deformation are a direct consequence of microstructure evolution and are observed from the evolution of the stress-strain curve. Therefore, all the phenomena involved are intimately linked to the material's properties.

Compression tests are carried out to study the mechanical behaviour of Alloy 28 during hot deformation. The microstructure evolution is characterised using optical microscopy (OM), scanning electron microscopy (SEM) and EBSD.

The implementation of the model using the experimental data is described in detail in the previous sections, along with the results and the flow stress-strain curves analysis methodology.

4. RESULTS AND MODEL IMPLEMENTATION

In this chapter, the results obtained from the described methodology are analysed.

The study of the as-cast microstructure and chemical composition is explained, followed by the evolution after the thermal treatment. The microstructure, composition and grain size are observed.

The raw curves from the hot compression test are smoothed and fitted following the Poliak and Jonas method explained in Section 2.4 to obtain the critical parameters for the onset of dynamic recrystallization. The results from the microstructural studies by EBSD and OM are used to obtain the recrystallized fraction and grain size. The study of strain-stress curves and recrystallization parameters are then used to adjust the material model.

Finally, the semi-empirical JMAK approach is presented, and the material parameters are obtained based on the experimental data.

4.1. As cast characterization

The results from the analysis of the as-cast billet are shown in this section.

4.1.1. Microstructural characterization

From Figure 3-2, the results on the microstructural characterization for the axial and radial direction are shown in Figure 4-1.

The interdendritic space becomes larger as it approaches the centre and finner in the edge, which shows that the microstructure changes along the radial direction. However, in the axial direction, the structure remains homogeneous.

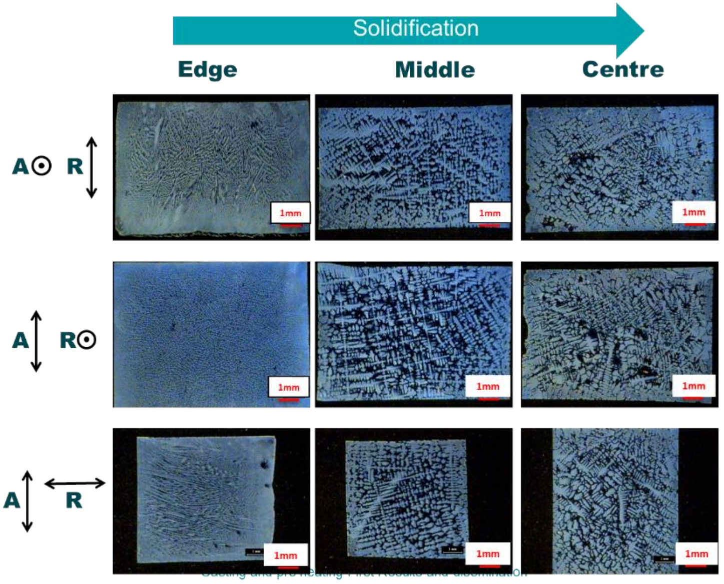

Figure 4-1. Microstructures correspond to the different axial and radial orientations.

A micro and macro-structural map are obtained in Figure 4-2 and Figure 4-3 to determine the relationship between the granular and dendritic distribution. The fine dendritic structure corresponds with the columnar grains, which have a 6 cm intro de billet depth, and the coarse dendritic corresponds to the equiaxial grains. The distribution of the equiaxial grains is coarse in the middle and gets finer as it approaches the centre of the billet because the grain has more time to develop as the cooling speed gets low.

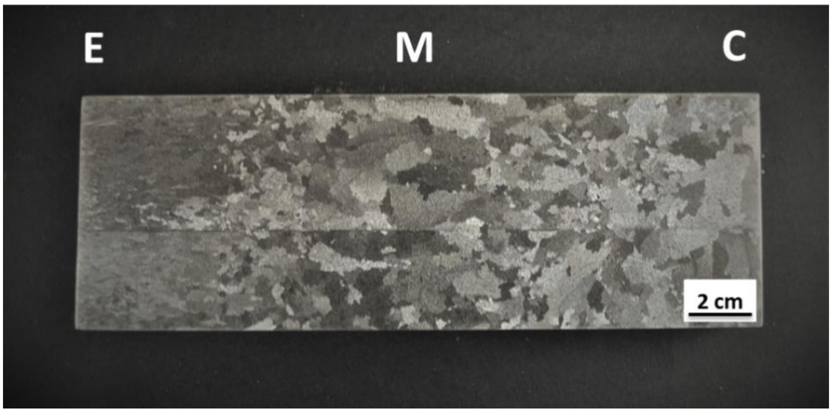

Figure 4-2. as-cast microstructural grain map for the Alloy 28.

As shown in Figure 4-3, the dendritic distribution gets coarse as it gets close to the centre of the billet, which involves an increase in the interdendritic space. Therefore, in the centre of the billet, the appearance of precipitates is most likely to occur.

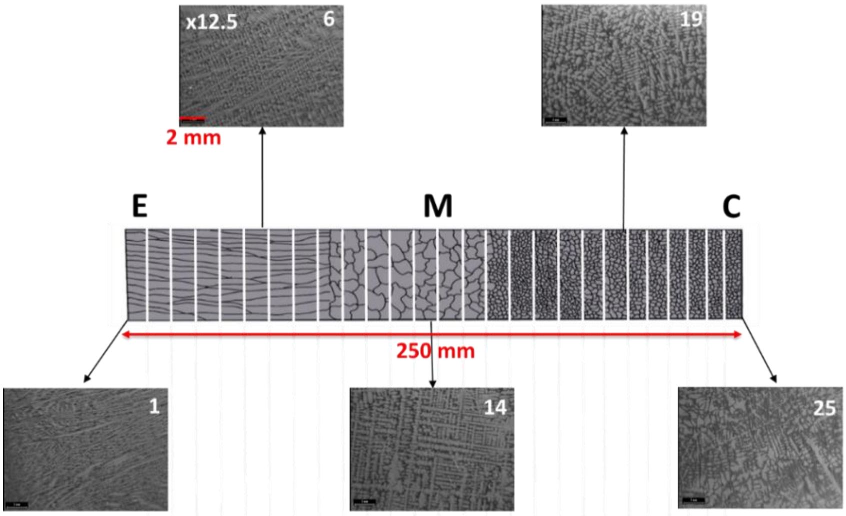

Figure 4-3. As cast dendritic structure map for the Alloy 28.

The initial grain size is obtained using the ASTM E1122-13 I standard (Table 4-1). For the columnar grain size, the equivalent diameter is obtained due to the tubular structure of the grains.

Zone	G (ISO)	Average grain size (mm)
Edge (*)	-5	2.00
Middle	-9	7.96
Centre	-7	4.00

(*) Average diameter, this zone presents columnar grains deep 6 cm of the ingot.

Table 4-1. Diameter for the As cast Alloy 28.

According to Table 4-1, the results agree with the macroscopic observation, which concludes that the ingot presents a heterogeneous structure: columnar grains at the edge of the billet, equiaxial grain that refines as it approaches towards the centre because the degree of subcooling is already high and the critical size of the nuclei decreased when solidification reaches the centre. Consequently, the interdendritic space increases in the billet's centre, favouring the appearance of precipitates [113].

4.1.2. Compositional Characterization

The average composition is shown in Table 4-2. A general homogeneity with a Mo decrease in the centre of the billet is observed.

Area	**Chemical Analysis (%)**												
	C	**Si**	**Mn**	**P**	**S**	**Cr**	**Mo**	**Ni**	**Cu**	**Ti**	**Nb**	**V**	**Al**
Centre	0.010	0.31	1.38	0.013	<0.005	27.0	3.55	31.2	1.04	0.01	0.03	0.07	0.013
	±0.002	±0.02	±0.03	±0.002	--	±0.4	±0.05	±0.7	±0.03	±0.005	±0.004	±0.01	--
Middle	0.012	0.32	1.45	0.015	<0.005	27.0	3.75	31.4	1.06	0.01	0.03	0.07	0.013
	±0.002	±0.02	±0.03	±0.002	--	±0.4	±0.05	±0.7	±0.03	±0.005	±0.004	±0.01	--
Edge	<0.010	0.32	1.45	0.015	<0.005	27.1	3.8	31.2	1.04	0.01	0.03	0.07	0.014
	±0.002	±0.02	±0.03	±0.002	--	±0.4	±0.05	±0.7	±0.03	±0.005	±0.004	±0.01	--

Expanded uncertainly calculated for 95% confidence interval

Table 4-2. Composition by area of the As-Cast Alloy 28.

In Figure 4-4, the results for the compositional microsegregation are obtained. In the middle and centre of the billet, the interdendritic areas present high values of Mo in contrast with the dendritic area, where the composition is homogeneous.

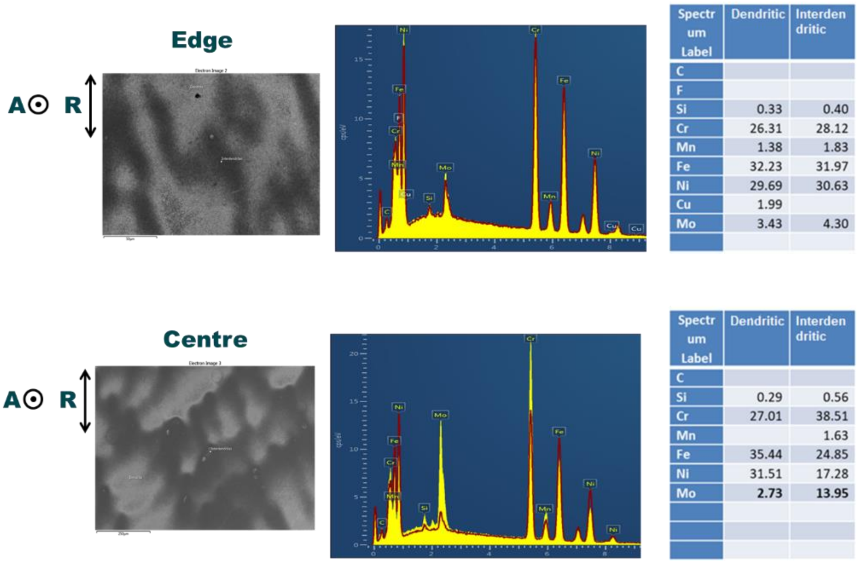

Spectrum Label	Dendritic	Interdendritic
C		
F		
Si	0.33	0.40
Cr	26.31	28.12
Mn	1.38	1.83
Fe	32.23	31.97
Ni	29.69	30.63
Cu	1.99	
Mo	3.43	4.30

Spectrum Label	Dendritic	Interdendritic
C		
Si	0.29	0.56
Cr	27.01	38.51
Mn		1.63
Fe	35.44	24.85
Ni	31.51	17.28
Mo	**2.73**	**13.95**

Figure 4-4. Microsegregation and composition in the edge and centre of the As cast Alloy 28.

Compositional maps are used to confirm the presence of Mo in the centre of the ingot. As seen in Figure 4-5, the presence of molybdenum appears in the interdendritic space, which can lead to brittles and a reduction in the mechanical properties and delayed recrystallization during forging.

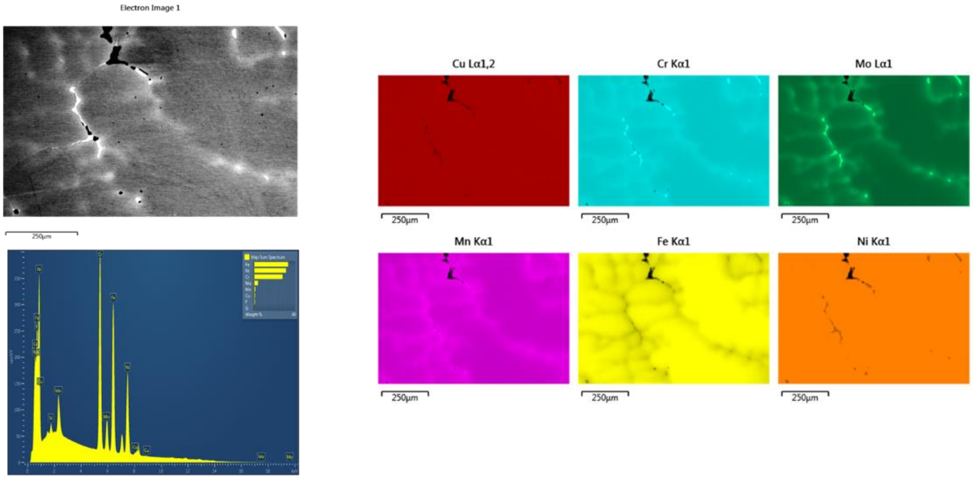

Figure 4-5. Compositional map for the centre of the As cast Alloy 28.

Mo percentage decreasing in the centre is caused by the appearance of Mo precipitates in the interdendritic spaces. This is related to the increase of the interdendritic space in the centre compared to the edge where the Mo concentration is homogeneous, and precipitation does not occur.

These results are compared with the material after the thermal treatment used to solve heterogeneity in the ingot and eventually dissolve Moprecipitates.

4.2. Pre-Forge thermal treatment

After metallographic preparation described in Section 3.2, the grain size of the thermally treated samples is obtained using the ASTM E1122-13 I standard (Table 4-3). As observed, the grain size has been homogenised in the tree areas, especially between the edge and the middle radio. In addition, segregation has disappeared, as shown in Figure 4-6.

Zone	G (ASTM)	Average Grain Size (mm)
Edge	-8.78	7.58
Middle	-9.00	7.96
Centre	-7.78	5.36

Table 4-3. Diameter for the Pre forge Alloy 28.

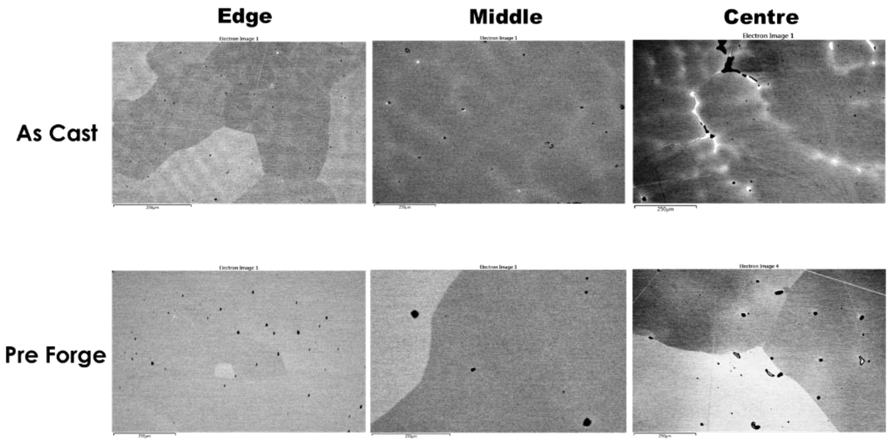

Figure 4-6. Comparison between the As-Cast and the Pre Forge microstructure.

At a microstructural level, the composition map in the centre is obtained (Figure 4-7), where it can be observed that the molybdenum precipitates are dissolved.

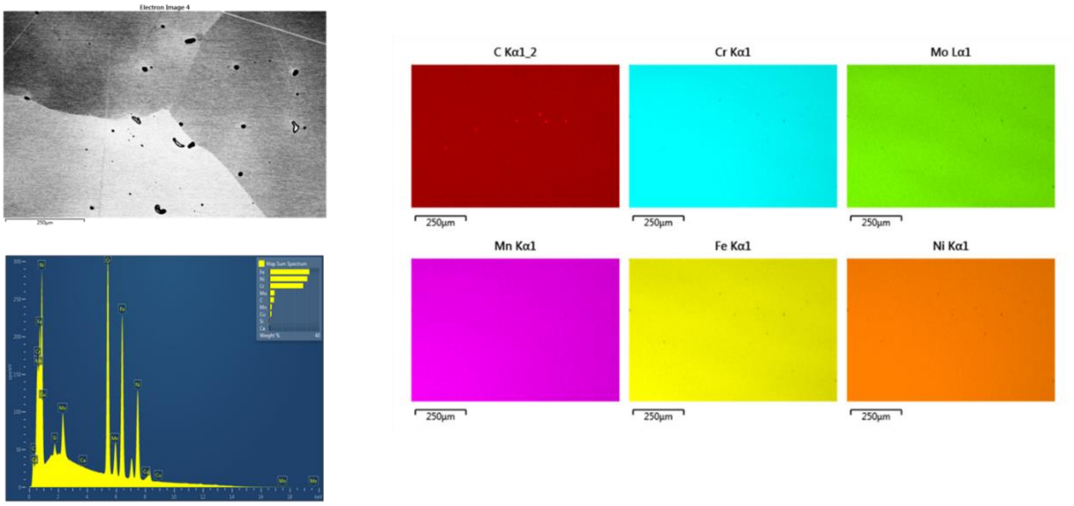

Figure 4-7. Microsegregation and composition for the pre forge As cast alloy 28.

The results agree with the previous predictions and confirm that the thermal treatment can homogenize and dissolve the precipitates. In conclusion, the thermal treatment is effective for the initial objectives: it homogenises the ingot, removes microsegregation, and dissolves precipitates. In all this way, the material is ready for hot working.

4.3. Forged bar characterization

The rounded bar is analysed. It is found that the microstructure is heterogeneous in the Top Feeder, as shown in Figure 4-8. Large grains with a necklace structure in the boundaries are found in the edge vs a more refined grain as it approaches the centre of the bar. Because the bar is exposed to an ambient temperature, a temperature gradient is created between the centre and the edge; if the stresses increase, the recrystallization rate decreases and the necklace structure is formed. On the other hand, the centre's recrystallisation is fully developed as an austenite microstructure (Figure 4-8) because the working temperature is maintained and the stress decreases in this area,

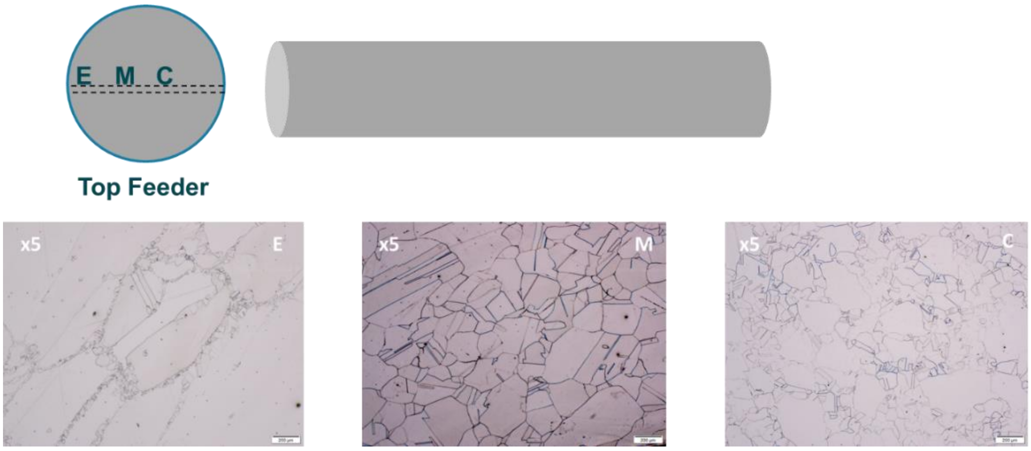

Figure 4-8. Microstructures for the Top Feeder of the Forged bar.

The corresponding distribution of the heterogeneous grains along the section is shown in Table 4-9, where the difference between coarse (Figure 4-9 (1)) and fine grain (Figure 4-9 (2)) is observed.

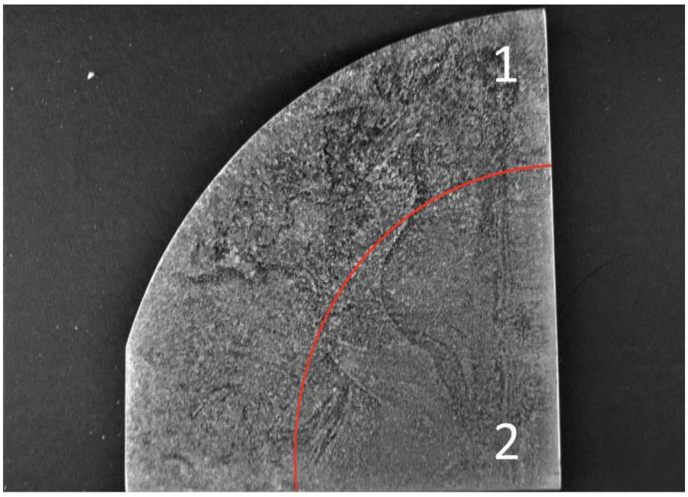

Figure 4-9. Macrostructure of the Top Feeder Forged bar.

The microstructure of the rounded bar foot is also heterogeneous, but no necklace structure is present in comparison with the top feeder. As a result, the grain becomes thinner as we approach the billet's centre. In Figure 4-11, it is observed that the area of coarse grain size (Figure 4-11 (3)) and when the thinner grain appears (Figure 4-11(2)).

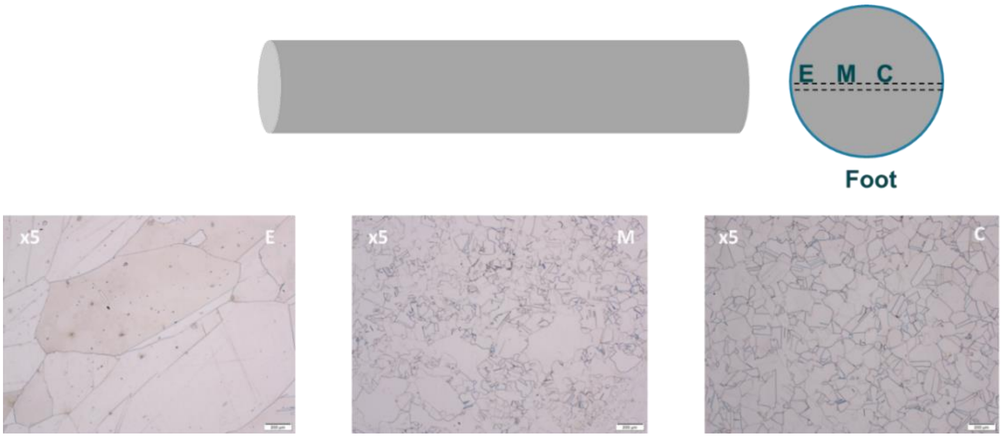

Figure 4-10. Microstructures for the Foot of the Forged bar.

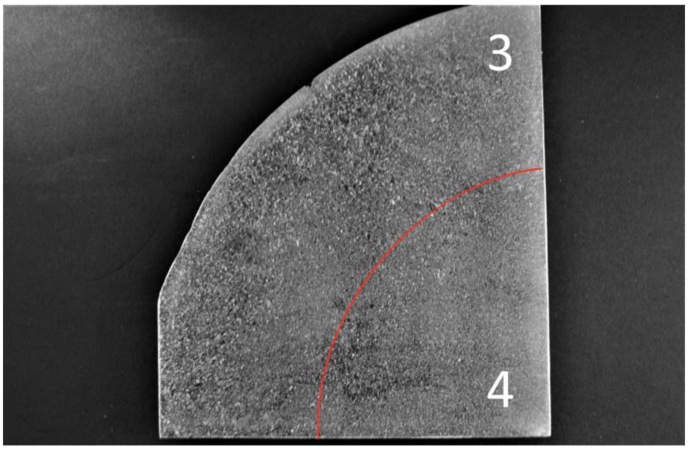

Figure 4-11. Macrostructure of the foot Forged bar.

The ASTM E112 standard is used to obtain each zone's grain size from the forged bar grain distribution, as is shown in Table 4-4.

Zone	G (ASTM)	Average Grain Size (mm)
Top Feeder Centre	2.6	1.27
Top Feeder Edge	-1.8	5.85
Foot Centre	2.7	1.22
Foot Edge	-1.8	5.85

Table 4-4. ASTM Grain Size for the forged bar.

The grain size distribution shows the already observed microstructural differences along the radial axis. However, there is no significant contrast between the top feeder and foot sections; therefore, the grain distribution along the axial axis is considered homogeneous. The data will then use later for model validation.

4.4. Hot compression test

The MR section from the billet is chosen for the hot compression test, as indicated in Section 3.4. In the following Figure 4-12, an estimated representation of the section based on the results obtained in Section 4.2 shows the grain distribution in the as-cast section (Figure 3-1) after the thermal treatment. Although the microstructure is not entirely homogeneous, the grain size range is catalogued under the same template according to the ASTM E1122-13-13 standard, so it is assumed to represent the whole section.

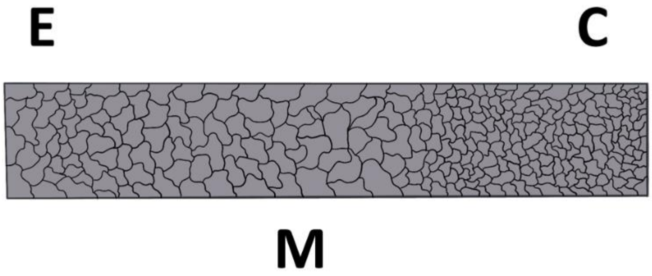

Figure 4-12. Representation of the Pre-forge section of Alloy 28.

The results obtained from the hot compression test are shown in this section. First, the strain stress curves are treated and analyzed and later on, the metallographic analysis is presented to obtain the parameters for the material modelling.

4.4.1. Stress-Strain curves

The strain-stress curves are refined and corrected before the Poliak and Jonas method [35], [44], [46] reviewed in 2.4.3. is applied to obtain the critical values for the onset of dynamic recrystallization.

The compression samples are measured twice with the same deformation parameters, and the raw data is obtained. Then, using the software ORIGIN®, the average of these curves is calculated and plotted as a simple curve, using the fitting tool and the Adjacent-Averaging method interpolated with 40 point from strain 0 to strain 0.8.

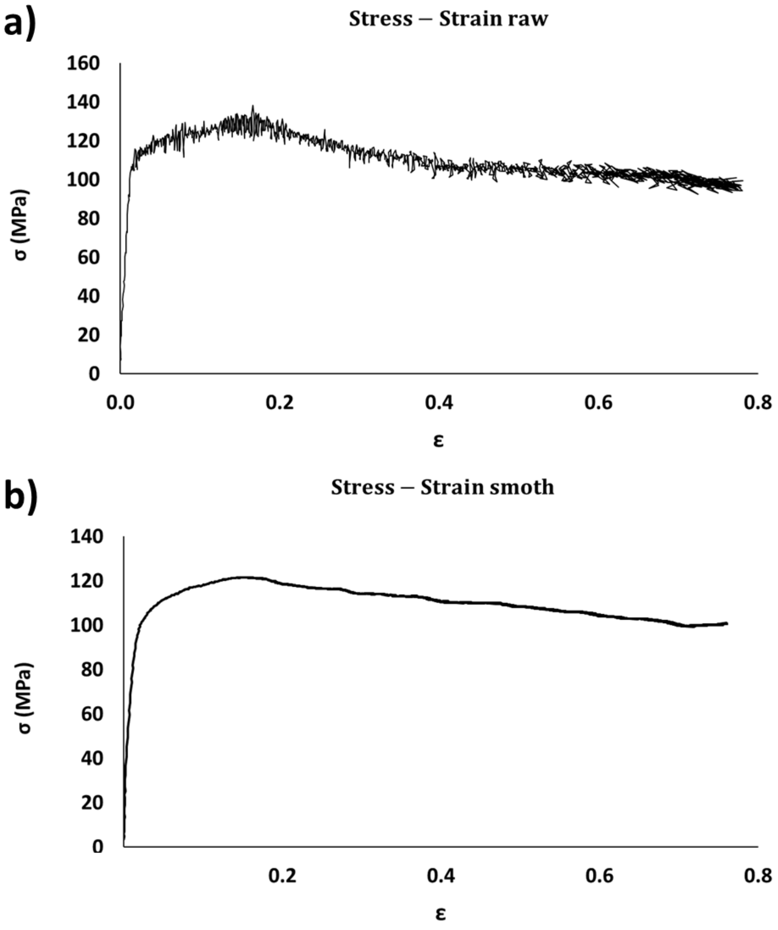

Figure 4-13. Exemplary interpolation of a hot compression flow curve, a) Raw data; After the interpolation.

During the deformation process, mechanical energy is converted to heat, raises the temperature and decreases the flow stress of the sample. The corrected flow stress is calculated with Equation (48), used before by Kapoor *et al.* [114], [115]:

$$\sigma_{\text{corr}} = \sigma_{\text{meas}}(\varepsilon) - \frac{\partial\sigma}{\partial T} I_{\varepsilon,\dot{\varepsilon}}\, \Delta T, \tag{48}$$

where σ_{corr} corresponds to the corrected flow stress, σ_{meas} is the experimentally measured flow stress, $\frac{\partial \sigma}{\partial T}$ is the temperature dependence of the flow stress as a function of strain and strain rate, and ΔT is the rise in temperature due to deformation. The temperature dependence of the flow stress is evaluated out of ten stress values ranging from $\varepsilon = 0 - 0.8$ as a function of the temperature, as it can be seen in Figure 4-14. The slope is obtained for every condition from each strain, and the correct temperature is applied.

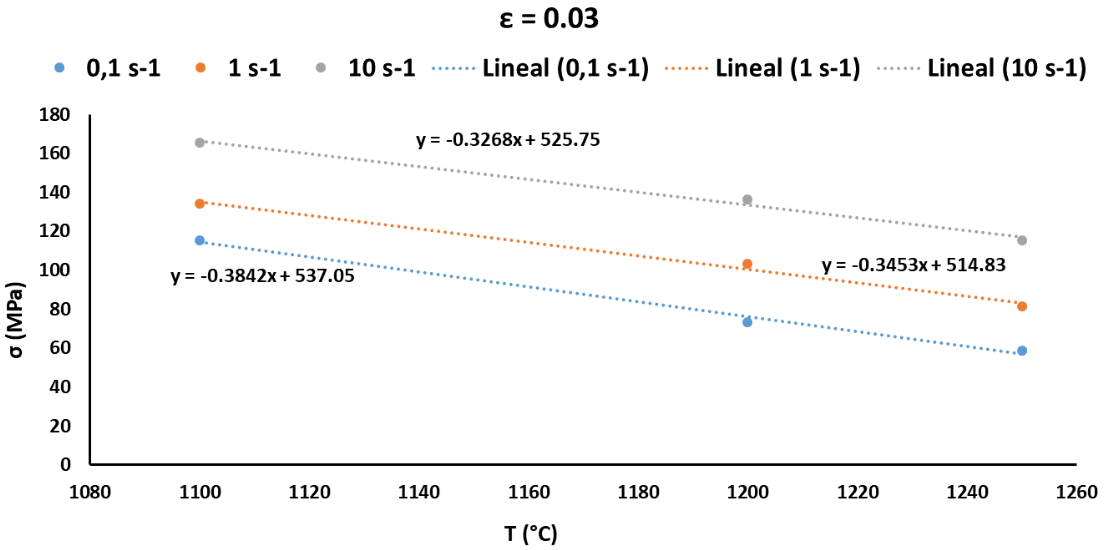

Figure 4-14. Flow stress versus the temperature for a strain of 0.03 for the tested Alloy 28.

Friction increases nonhomogeneous deformation, leading to the samples barrelling, as shown in Figure 4-15. Applying suitable lubricant can reduce friction between the sample and the die, but it would not eliminate and has to be corrected.

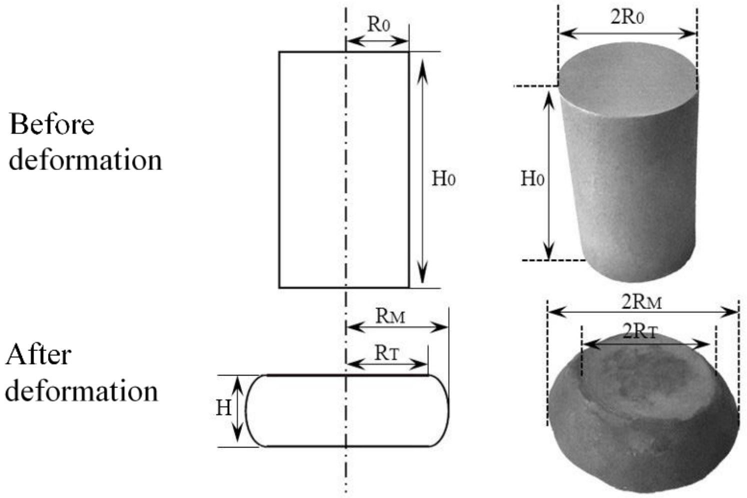

Figure 4-15. Schematic representation (left) and Physical representation (right) of a hot compression test.

In Figure 4-15, R_0 and H_0 are the initial radius and height of sample 15 mm and 10 mm, respectively (Figure 3-6). R_{T} and R_{M} are the top and maximum radio of the deformed samples, respectively. H is the instantaneous height during hot compression test. Roebuck *et al.* [116] developed a criterion named B, when $1 < B < 1.1$, the effect of friction on the flow stress can be eliminated. However, when $B \geq 1.1$, the difference between measured and the true flow stess cannot be overlooked.

Based on the upper-bound theory, Eberahimi and Najafizadeh [117] developed a simple theoretical analysis of barrel compression test, and a friction factor relationship is given by:

$$\begin{cases} R_{\text{av}} = \dfrac{R_0}{\sqrt{{H_0}/{H}}} \\ b = 4\dfrac{\Delta R}{R_{\text{av}}}\dfrac{H}{\Delta H} \\ \mu = \dfrac{(R_{\text{aw}}/H)b}{(4\sqrt{3})-(\frac{2b}{3\sqrt{3}})} \end{cases} , \qquad \textbf{(49)}$$

where μ is the friction coefficient varying from 0 (perfect sliding) to 1 (sticking), b is the barrelling parameter, R_{aw} is the average radius of the cylindrical sample after deformation, ΔH is the heat reduction $(\Delta H = H_0 - H)$, and $\Delta R = R_{\text{M}} - R_{\text{T}}$, i.e., the difference between the maximum and top radius. For the R_{T}, Eberahimi and Najafizadeh provided an experimental equation [117] by approximating the barrel sample with an arc of a circle. This equation is given by:

$$R_{\text{T}} = \sqrt{3\frac{H_0}{H}R_0^2 - 2R_{\text{M}}^2}. \qquad \textbf{(50)}$$

Therefore, the flow stress can be corrected for frictional effect using the following relationship [117]:

$$\begin{cases} \sigma^F = K\sigma^M \\ K = \dfrac{c^2}{2(\exp(C)-c-1)}, \\ C = \dfrac{2\mu R_0}{H_0} \end{cases} \qquad \textbf{(51)}$$

where σ^F is the flow stress after friction correction, σ^M is the measured flow stress by isothermal compression test, and k is the equivalent frictional coefficient $(k = \sigma^F/\sigma^M)$.

For Alloy 28, the thermal correction is applied using Equation (48), followed by Equation (51) to correct the friction of Figure 4-16 a). The result is a smoothed stress-strain curve with a stress reduction, as is shown in Figure 4-16 b). After this step, the P-J approach to obtain the critical values for DRX is applied.

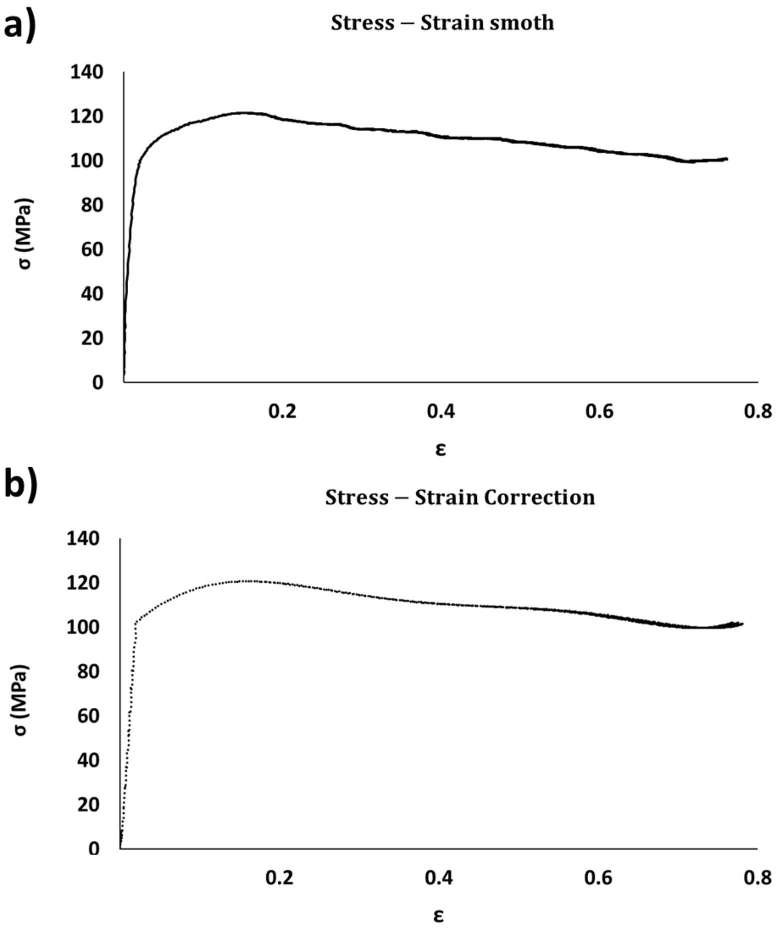

Figure 4-16. Stress-Strain curves for the pre-forge Alloy 28: a) Smooth thought interpolation; b) After thermal and friction correction.

Only plastic deformation is considered for the Poliak and Jonas method due to the irreversibility assumption [35]. Finally, in Figure 4-17, the calculus of the offset yield point and the elastic limit is shown.

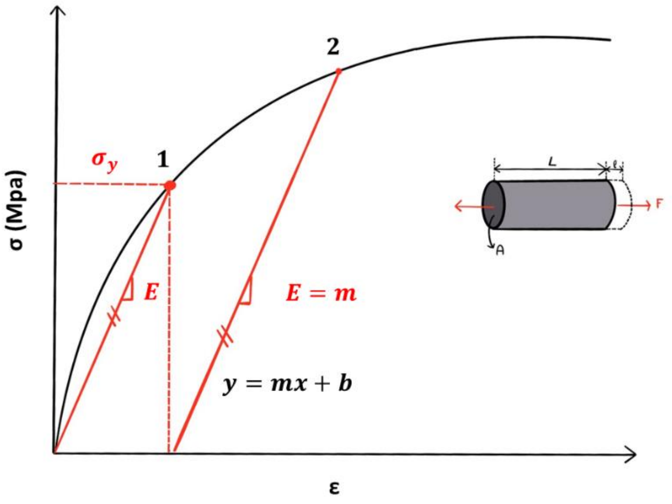

Figure 4-17. Stress-Strain curve showing typical yield behaviour: 1) Elastic limit; 2) Offset yield strength.

The Yield strength is obtained for each condition, and then the corresponding curve plastic zone of Figure 4-16 b) is fitted to a 7th-grade polynomial using excel solver tool as is shown in Figure 4-18 and expressed as:

$$\sigma = a_1\varepsilon^7 + a_2\varepsilon^6 + a_3\varepsilon^5 + a_4\varepsilon^4 + a_5\varepsilon^3 + a_6\varepsilon^2 + a_7\varepsilon + a_8. \tag{52}$$

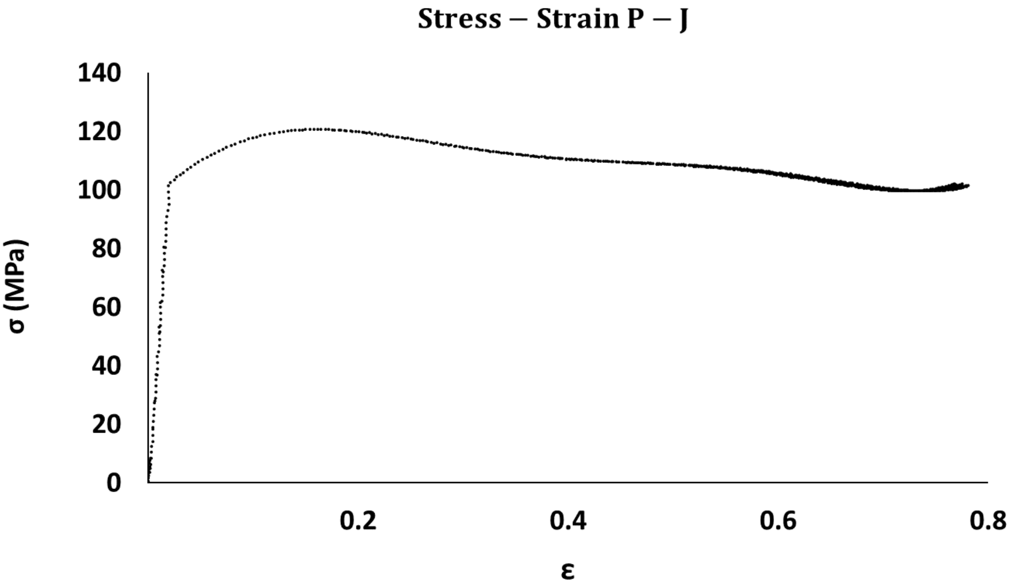

Figure 4-18. 7th polynomial fitting for the case of study.

According to P&J [35], [44], the initiation of DRX is associated with the point of inflection in the curve of strain hardening rate (θ) vs flow stress (σ). To plot the curve, an equation that fits the experimental $\theta - \sigma$ needs to be find which is calculated as:

$$\theta = \frac{\partial\sigma}{\partial\varepsilon} = 7a_1\varepsilon^6 + 6a_2\varepsilon^5 + 5a_3\varepsilon^4 + 4a_4\varepsilon^3 + 3a_5\varepsilon^2 + 2a_6\varepsilon + a_7 \ , \tag{53}$$

where a_1 to a_7 are constant for a given set of deformation conditions from zero until the peak stress. Consequently, the simplest equation that has an inflexion point is:

$$\theta = b_1\sigma^3 + b_2\varepsilon^2 + b_3\varepsilon + b_4 \ , \tag{54}$$

where b_1 to b_4 are constants for a given set of deformation conditions. Differentiation of (54) concerning σ results in:

$$\frac{d\theta}{d\sigma} = 3b_1\sigma^2 + 2b_2\sigma + b_3 \ , \tag{55}$$

from which the minimum point corresponds to the critical stress, i.e.,

$$\frac{d^2\theta}{d\sigma^2} = 0 => 6b_1\sigma + 2b_2 = 0 => \sigma_c = \frac{-b_2}{3b_1}, \tag{56}$$

represented inFigure 4-19. In Figure 4-20, σ_c is obtained with the coefficients of the 3th grade Equation (55) using the solver tool adjusting to the minimum error. Then, σ_p is calculated by interpolation when $\theta = 0$, and due to the lack of steady state in this particular case, no σ_{ss} is appreciated.

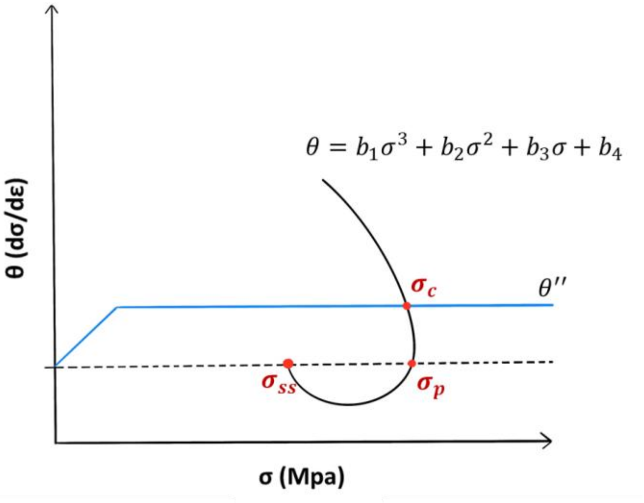

Figure 4-19. Schematic representation of θ vs σ curve and the corresponding σ_c, σ_{ss} and σ_p.

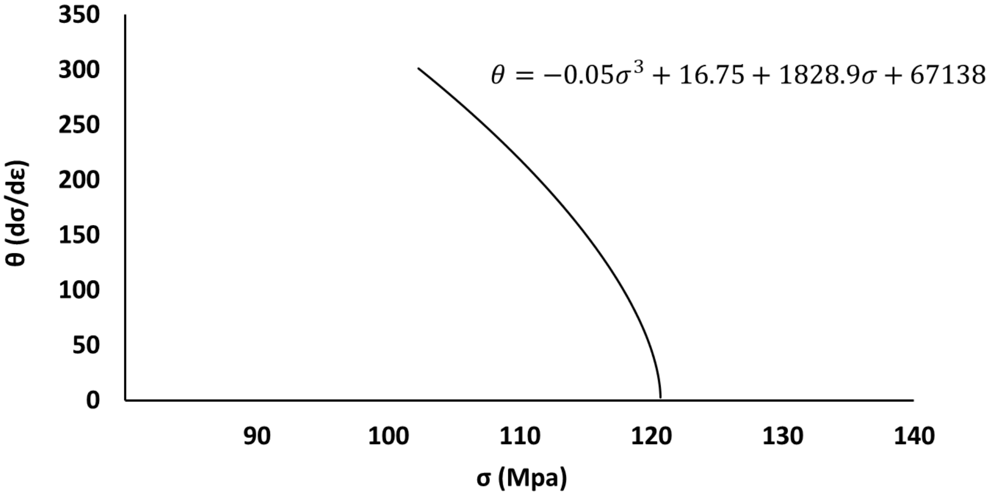

Figure 4-20. $\theta - \sigma$curve for the Alloy 28.

Finally, the corresponding strains $(\varepsilon_c, \varepsilon_p)$ are obtained from the above curve, as is presented in Figure 4-21.

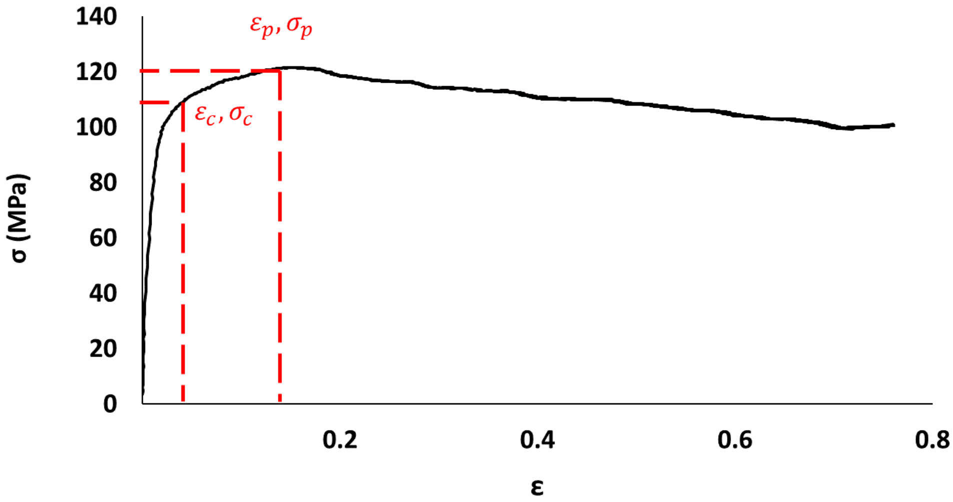

Figure 4-21. Corresponding ε_c and ε_p for the current case of Alloy 28.

The above steps are applied for every condition tested, and the corresponding curves are shown in Appendix A. The experimental ε_c and ε_p are presented in Table 4-5.

Strain rate	$0.1\ s^{-1}$		$1\ s^{-1}$		$10\ s^{-1}$	
T (°C)	ε_c	ε_p	ε_c	ε_p	ε_c	ε_p
1100	0.04	0.15	0.04	0.13	0.05	0.16
1200	0.04	0.13	0.03	0.12	0.03	0.07
1250	0.05	0.16	0.03	0.11	0.03	0.07

Table 4-5. Resume of the critical and peak strains for the study case.

In Figure 4-22, a visual comparison of each ε_c and ε_p is showed. According to the bibliography for wrought materials, the ε_c increases as the strain rates increase for a constant temperature and decrease as the temperature increases for a constant strain rate [13], [15]. The hypothesis is fulfilled for the 1100 °C case. On the other hand, for 1200 °C and 1250 °C ε_c decreases as the $\dot{\varepsilon}$ increases. When the focus is on temperature variation, only the case of $0.1\ s^{-1}$ does not agree with the behaviour showed for the alloy 28, which DRX easily occurs at high deformation temperature and low strain rate [13].

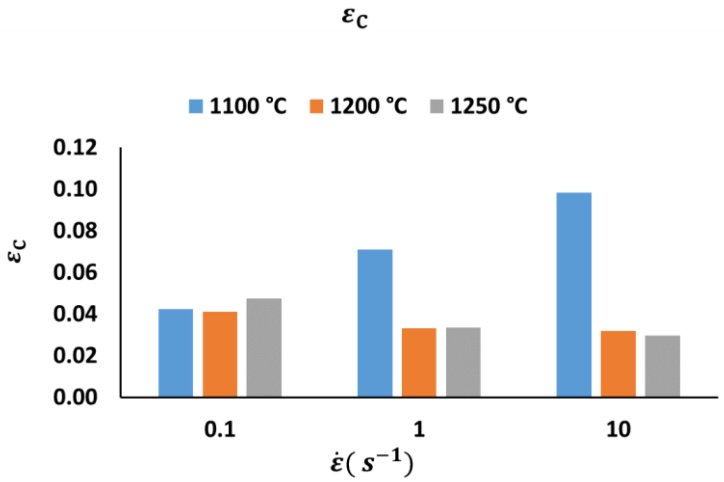

Figure 4-22. Comparison of the critical strain for the different test conditions.

The disagreement between the literature and the current work is related to the coarse structure from the pre-forge state used versus the wrought material used in previous research [118]. The DRX in ingot material is sensitive to the starting as-cast microstructure and cannot be accurately modelled using wrought material behaviour [58]. Therefore, the critical conditions depend on the starting microstructure's morphology.

In the following section, the results from the strain stress curves are complemented with the microstructure and EBSD measurements.

4.4.2. Recrystallization measurements

In this section, the results from the EBSD measurements are presented. For the seek of understanding, the charts used to summarize the parameters obtained show the recrystallization fraction (χ_{drx}) in percentage (blue) and the recrystallized grain size (D_{drx}) in μm (orange). Then, the corresponding EBSD map at the same scale for each condition is displayed above the bars. The remaining EBSD maps for every condition is presented in Appendix B.

In Figure 4-23, it can be seen that χ_{drx} is higher at lower strain rate and on the other hand, D_{drx} is as the strain rate increases. As shown in Figure 4-22, the initiation of DRX does not ensure a higher development of the DRX. For the case of 1100 ° and 0.1 s^{-1}, DRX starts earlier, so a larger recrystallized grain size is shown when the strain is reached. On the other hand, for 1100 ºC and 1 s^{-1}, the DRX is almost nonexistent due to the strain rate conditions that are not low or high enough to make the DRX progress for the initials coarse grains.

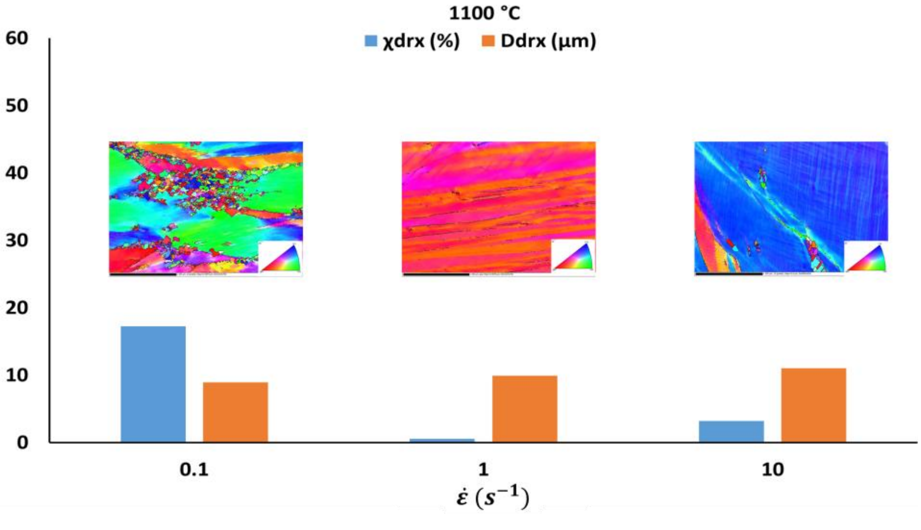

Figure 4-23. Recrystallized fraction and grain size for 1100 ºC vs EBSP map (200 μm).

In Figure 4-24, the microstructure for 1200 ºC shows that the recrystallized fraction increases with the strain rate. At a higher temperature, the DRX progresses further for a higher strain rate. However, for the particular case of 0.1 s^{-1}, despite χ_{drx} is the lowest, the average recrystallized grain is higher than the case of 10 s^{-1}. This may be because fewer nuclei are formed, so the recrystallization progresses further in less former grains. For the intermediate strain rate and the previous temperature, the conditions are insufficient for the DRX to progress.

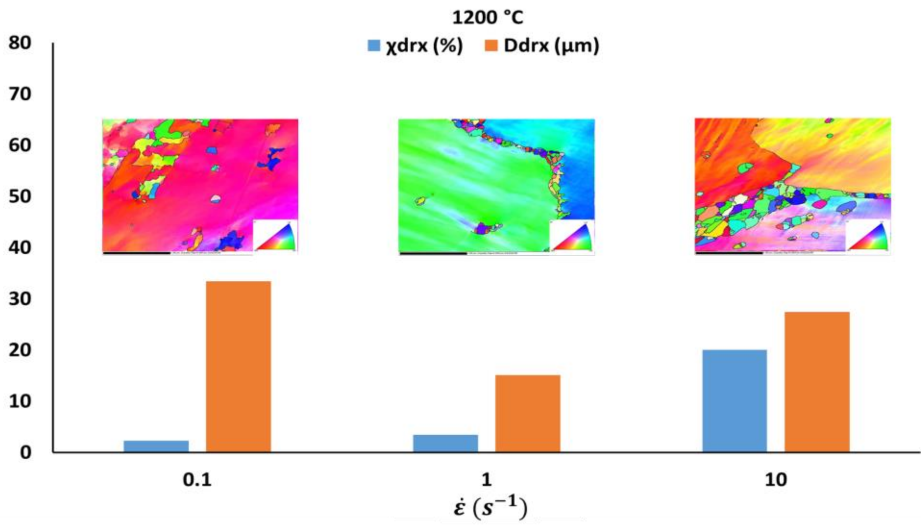

Figure 4-24. Recrystallized fraction and grain size for 1100 °C vs EBSP map (200 μm).

In Figure 4-25, for 1250 ºC, the recrystallized fractions and grain size are much higher than the previous cases at lower temperatures. This may be a consequence of the temperature rises, as is reviewed in Section 2.5. The χ_{drx} increased along with the D_{drx} even at the strain rate of 1 s^{-1}, in which at the lowest temperatures, the DRX does not progress.

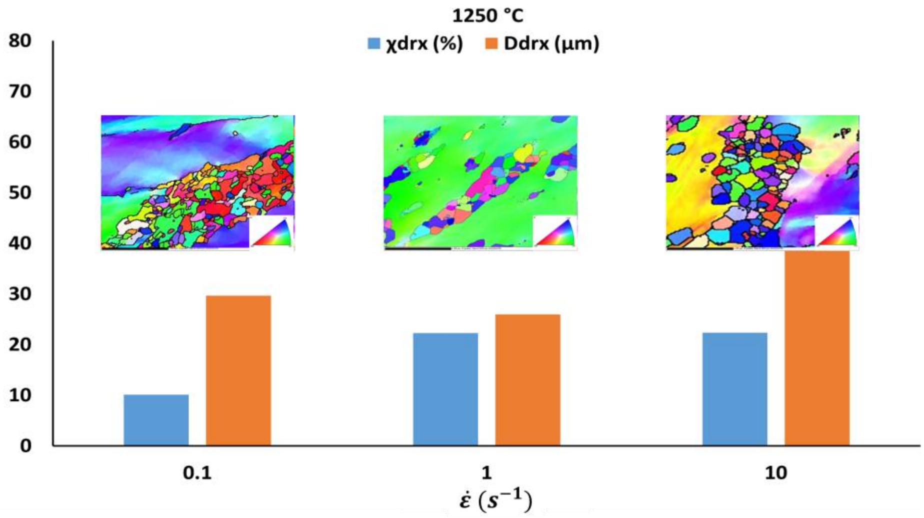

Figure 4-25. Recrystallized fraction and grain size for 1200 °C vs EBSD map (200 μm)

The above figures conclude that the initial microstructure greatly influences the DRX behaviour, as suggested from the critical conditions obtained in the previous section. Then, for an initial coarse grain microstructure, as the higher temperature is, the DRX mechanism progress further. For strain rates of 0.1 s^{-1} and 10 s^{-1}, the DRX ratio is higher than for the case of 1 s^{-1}, for which the material finds it hard to recrystallize.

Due to the higher activation energy in as-cast vs wrought material [61], the results obtained for the critical conditions do not agree with a delayed DRX scenario. However, as observed in this microstructural study, even though recrystallization has already started, it does not develop entirely in any deformation conditions. From these observations, it can be concluded that critical strain is a condition necessary but not sufficient since a low ε_c do not ensure a high DRX ratio.

4.5. Modelling on dynamic recrystallization

The analytical modelling of recrystallization often uses modified versions of the JMAK equation. This model has been adapted to be used in hot working simulation software from the experimental data. Before the equations for DRX, a constitutive model in viscoplastic behaviour needs to be applied. The Hansell-Spittel model is used as a generalized model for this purpose

4.5.1. Hansell-Spittel constitutive model

The "Hansel-Spittel" law applies to viscoplastic behaviour. It is temperature-dependent and takes strain hardening for softening phenomena into account and the strain rate. The equation takes the following form:

$$\sigma = Ae^{m_1 T}\, T^{m_9}\, \varepsilon^{m_2}\, e^{\frac{m_4}{\varepsilon}}\, (1+\varepsilon)^{m_5 T}\, e^{m_7 \varepsilon}\, \dot{\varepsilon}^{m_3}\, \dot{\varepsilon}^{m_8 T}, \tag{57}$$

where T is the temperature given in Celsius, m_1 and m_9 define the material's sensitivity to temperature, m_5 term coupling temperature and strain, m_8 term coupling temperature and strain rate, m_2, m_4, and m_7 define the material's sensitivity to strain, and m_3 depends on the material's sensitivity to the strain rate.

The H-S parameters are obtained from the corrected stress-strain curves from Section 4.3.1 using the tool solver from excel. The goal is to obtain a Hansell-Spittel Stress-Strain curve as close as possible to the corrected one, as shown in Figure 4-26. The complete set of corrected curves for the Hansell-Spittel model is shown in Appendix C.

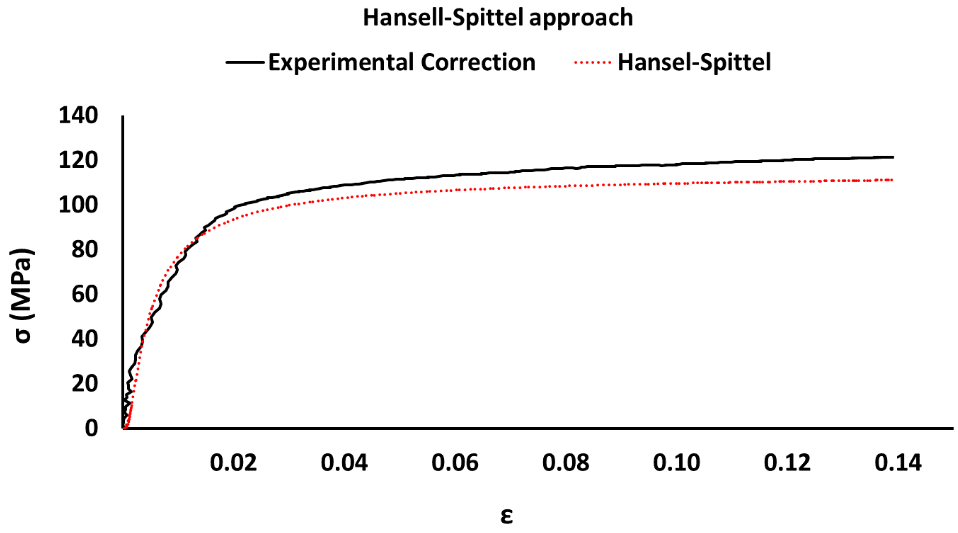

Figure 4-26. Hansell-Spittel approach for the studied Alloy 28.

The parameters obtained are shown in Table 4-6.

HS Variables									
A	**m_1**	**m_2**	**m_3**	**m_4**	**m_5**	**m_6**	**m_7**	**m_8**	**m_9**
35645	-0.004	0	-0.290	-0.004	0	0.70755	0	0	0

Table 4-6. Hansell-Spittel parameters for the studied Alloy 28.

4.5.2. Semi-empirical JMAK approach

Modified JMAK used in this project only takes into account DRX, and DRV predicts both: recrystallized fraction and Recrystallized grain size.

The equation presented in this part has been generalized from different models found in the literature [79].

4.5.2.1. Critical Strain

As it was reviewed in Section 2, the critical strain ε_c defines a threshold value for nucleation of recrystallized grains during the deformation step. It corresponds to the minimum strain level, from which dynamic and meta-dynamic recrystallization processes could occur. For strain lower than ε_c, only the static recrystallization type is observed.

The following Equation (58) is used to obtain the material parameters, using the excel tool Solver to adjust with the experimental data:

$$\varepsilon_\mathrm{c} = A_\mathrm{crit}\, E_\mathrm{p1}\, {d_0}^{E_\mathrm{p2}}\, \dot{\varepsilon}^{E_{p3}}\, Z^{E_\mathrm{p4}}\, exp\left(\frac{Q_{E_\mathrm{p}}}{RT}\right), \tag{58}$$

where A_crit, E_p1, E_p2, E_p3, E_p4, are the material parameters and $Q_{\mathrm{E_p}}$ is the activation energy for the initiation of dynamic recrystallization. The obtained parameters for the studied material are shown in Table 4-7.

JMAK Variables								
A_{crit}	**Ep_1**	**Ep_2**	**Ep_3**	**Ep_4**	**Q**	**Q_{ep}**	**R [J/mol K]$_7$**	**d_0 (µm)**
-0.08	-0.05	-0.37	-0.10	-0.06	501205.71	32457	8.31	4554.83

Table 4-7. Material parameters for the prediction of ε_c.

In Figure 4-27, the comparison between the experimental ε_c and the JMAK approach is shown. The model corrects the critical strain, so, as the strain rate increases, the critical strain decreases. For the 1100 ºC, the JMAK ε_c highly differs from the experimental data. On the contrary, for 1200 ºC and 1250 ºC, the error decreases.

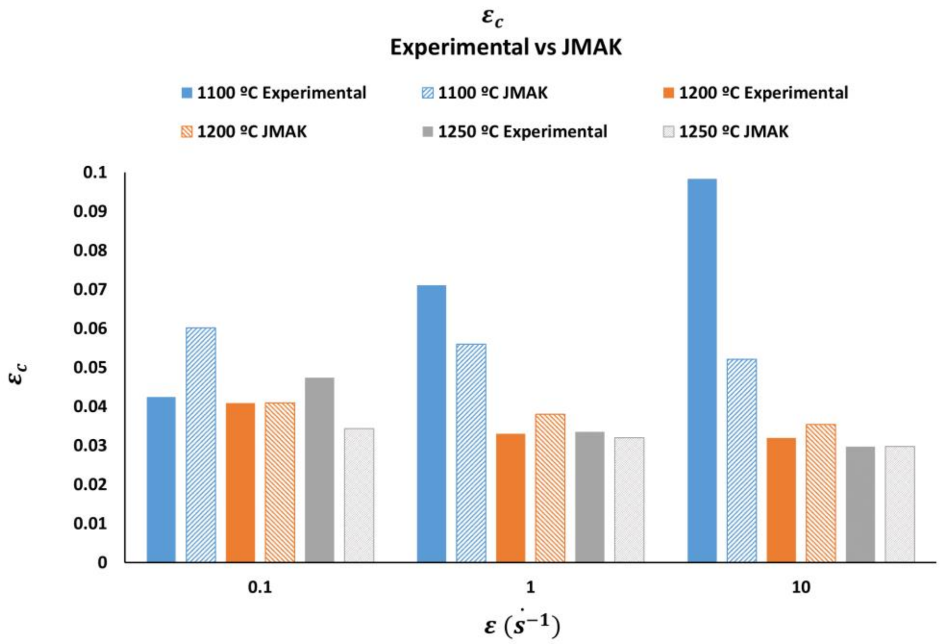

Figure 4-27. Comparison between experimental vs predicted ε_c.

4.5.2.2. Dynamic recrystallization (DRX)

Dynamic recrystallization describes the process where nuclei of new grains appear and grow during the deformation step only for $\bar{\varepsilon} > \varepsilon_c$.

The recrystallization kinetics is given by:

$$X_{\mathrm{drx}} = 1 - exp\left(X_{d_1}\left(\frac{\bar{\varepsilon}_f - X_{d_3}\varepsilon_c}{\bar{\varepsilon}_{0.5} - X_{d_4}\varepsilon_c}\right)^{X_{d_2}}\right), \tag{59}$$

where,

$$\bar{\varepsilon}_{0.5} = T_{\mathrm{d}_1}\, d_0{}^{T_{\mathrm{d}_2}} \dot{\varepsilon}^{T_{\mathrm{d}_3}} Z^{T_{\mathrm{d}_4}}\ exp\left(\frac{Q_{\mathrm{T_d}}}{RT}\right), \tag{60}$$

is the strain for 50% recrystallization and $\chi_{\mathrm{d}_1}, \chi_{\mathrm{d}_2}, \chi_{\mathrm{d}_3}, \chi_{\mathrm{d}_4}, T_{\mathrm{d}_1}, T_{\mathrm{d}_2}, T_{\mathrm{d}_3}, T_{\mathrm{d}_4}, Q_{\mathrm{T_d}}$ are the material parameters. $Q_{\mathrm{T_d}}$ is the energy necessary for the DRX to progress.

The recrystallized grain size is defined by:

$$D_{\mathrm{drx}} = D_{\mathrm{d}}\, X_{\mathrm{drx}}^{\mathrm{adrx}}, \tag{61}$$

where,

$$D_{\mathrm{d}} = D_{\mathrm{d}_1}\, d_0{}^{D_{\mathrm{d}_2}} \dot{\varepsilon}^{D_{\mathrm{d}_3}} Z^{D_{\mathrm{d}_4}}\ exp\left(\frac{Q_{D_d}}{RT}\right), \tag{62}$$

is the recrystallized diameter for a full DRX and $a_{\mathrm{drx}}, D_{\mathrm{d}_1}, D_{\mathrm{d}_2}, D_{\mathrm{d}_3}, D_{\mathrm{d}_4}$ are the material parameters. $Q_{\mathrm{D_d}}$.is the activation energy for the development of the recrystallized grain to grow.

Using the solver tool from Excell, the material parameters are found to minimise the error between the experimental data obtained in Section 4.3.2. and the model. In Table 4-8, the parameters for the recrystallized fraction prediction are obtained.

HS Variables										
X_{d1}	X_{d2}	X_{d3}	X_{d4}	T_{d1}	T_{d2}	T_{d3}	T_{d4}	Q_{td}	R [J/mol K]	d_0 (μm)
0	7.46	4	-4.44	0.39	0.13	0	-0.04	299.84	8.31	4554.83

Table 4-8. Material parameters for the prediction of χ_{drx}.

As it can be seen in Figure 4-28, the modelized χ_{drx} increases with the strain rate and temperature. According to this model, recrystallization progress further as the strain rate increases for a given temperature and vice-versa.

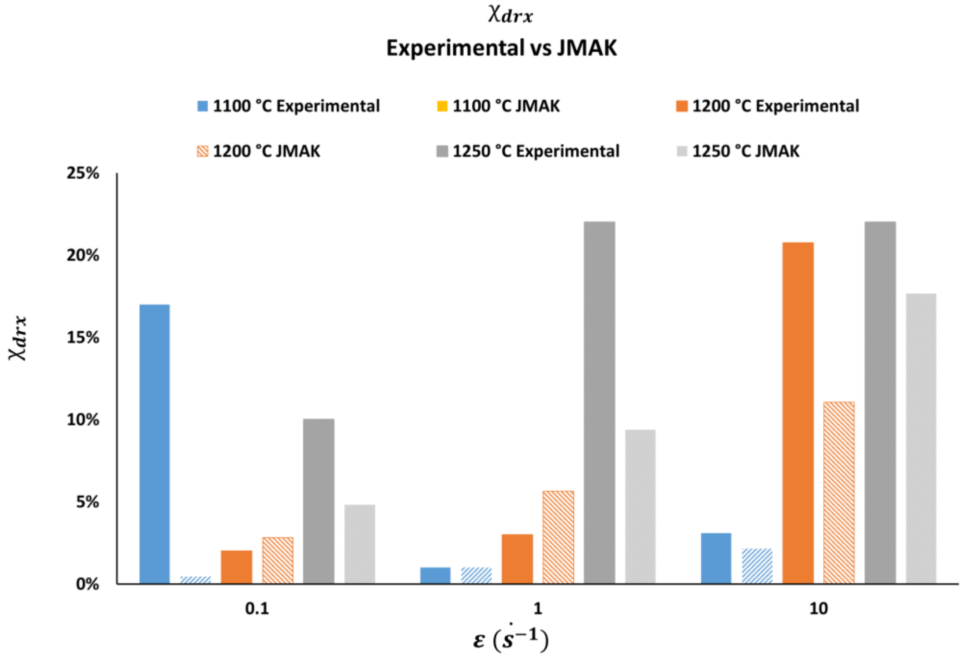

Figure 4-28. Comparison between experimental vs predicted χ_{drx}.

In Table 4-9, the material parameters for the modelling of D_{drx} is showed. The parameters are obtained using the solver tool from excel minimizing the error between the experimental and the predicted values.

JMAK Variables							
D_{d1}	Dd_2	D_{d3}	D_{d4}	Q_{Dd}	a_{drx}	R [J/mol K]$_7$	d_0 (μm)
0	1.38	-0.16	0.06	-80334.45	0.46	8.31	4554.83

Table 4-9. Material parameters for the prediction of D_{drx}.

In Figure 4-29, the comparison between the experimental and the predicted D_{drx} are showed. For the experimental data, the recrystallized grain size increased with the temperature except for the case of 1200 ºC and 0.1 s^{-1}. In the model, this behaviour is represented, and as it can be seen for the same temperature the D_{drx} slightly increase with the strain rate. According to the literature, the recrystallized grain size increases with the temperature for a given strain rate, so the model agrees with this behaviour. However, the experimental data do not agree with the case of 0.1 s^{-1}.

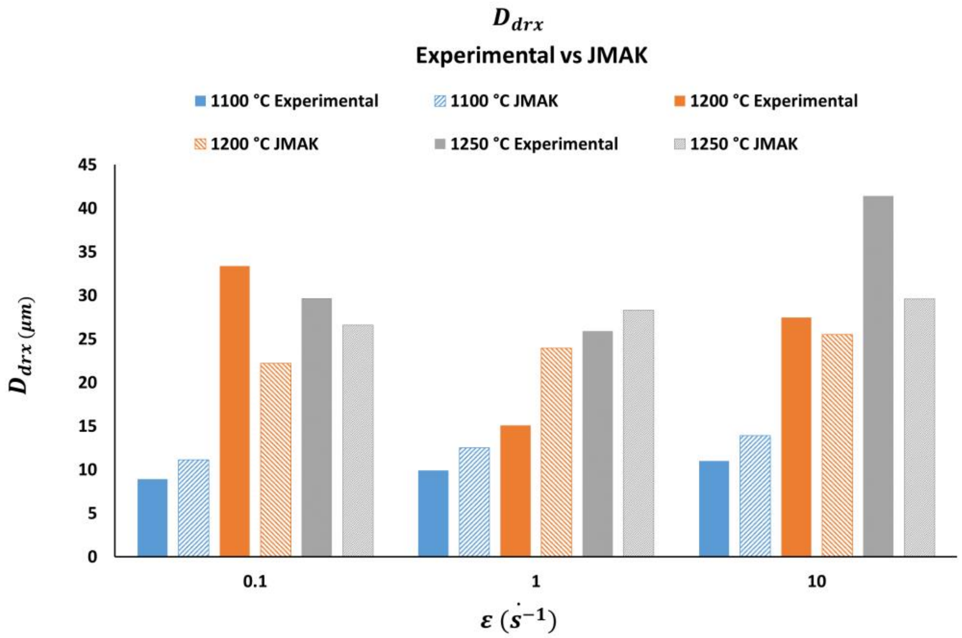

Figure 4-29. Comparison between experimental vs predicted D_{drx}.

The above parameters are introduced in the material model file to simulate the process and compare it to a reference model described in Section 5.

4.6. Summary

This section summarized the results from the experimental methodology described in Section 3.

Poliak and Jona's method is used to obtain experimental critical strain. Using EBSD and optical microstructures, the recrystallized diameter and fraction are obtained using EBSD and optical microscopy.

The Semi-empirical model is then revied and fitted using the experimental data, and the material parameters were obtained. At first sight, the model homogenized and created a tendency in the values, and the represented errors are minimized.

The following chapter validates the model with the parameters obtained above.

5. MODEL VALIDATION AND DISCUSSION

In this section, the model obtained is tested using Forge ® simulation software. These results are then compared with an industrial adapted model and validated with the measurements of the forged bar.

5.1. Simulation groundwork

The process parameters are studied to set up the simulation, and a process implementation is built for FORGE®. In this section, both requirements are set.

5.1.1. Industrial process

The ingot geometry shown in Figure 5-1 is used as an initial step for the simulation.

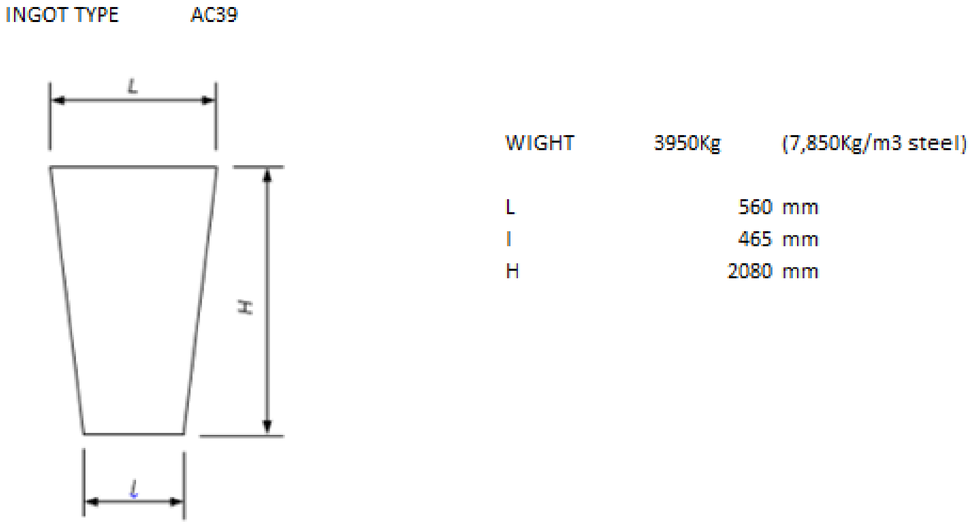

INGOT TYPE AC39

WIGHT 3950Kg (7,850Kg/m3 steel)

L	560 mm
l	465 mm
H	2080 mm

Figure 5-1. Initial ingot geometry.

The manufacture conditions are determined and presented in the below Table 5-1:

Air temperature	20 ºC
Air heat transfer Coefficient	10 W/m²
Initial bar temperature	1270 ºC
Initial transfer time	180 s
Tooling temperature	250 ºC
Heat exchange parameters	4000 W/m² K
Friction coefficient	0.3 – (Coulomb's law) Water+Graphite

Table 5-1. Design conditions.

The forging process is divided into three steps, as shown in Figure 5-2. After each forging, the billet is heated to prepare it for the next step.

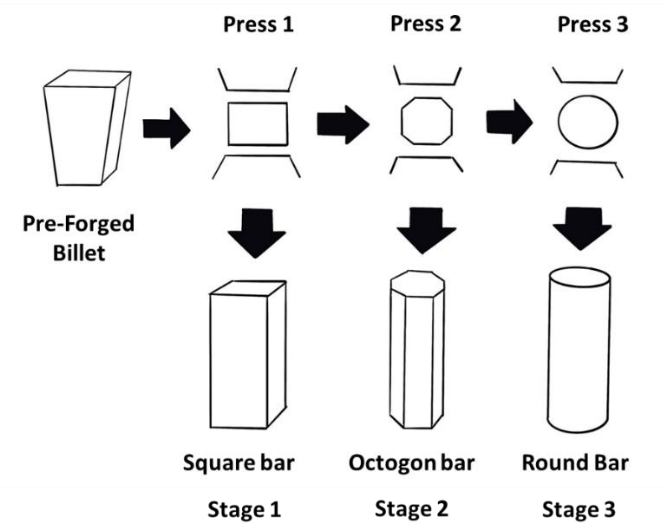

Figure 5-2. Steps of the forging process for de Alloy 28.

The following Table 5-2, Table 5-3 and Table 5-4 show the schedule for each stage. The parameters measured are summarized and shown in Figure 5-3:

- **Manipulator**: Refers to the driven side of the bar: right (R) and lefts (L).
- **Stroke**: Pass depth.
- **Bite**: Longitudinal spacing covered by the manipulator.
- **Rotation**: The degrees rotated by the manipulator after each stroke.

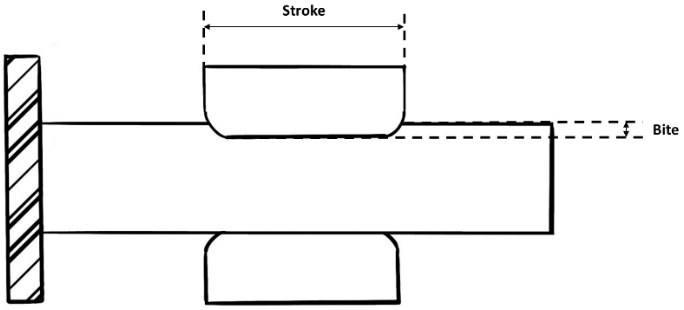

Figure 5-3. Diagram of the forging process.

Pass	Manipulator	Stroke (mm)	Bite (mm)	Rotation (º)
1	L	120	150	90
2	L	120	150	90
3	L	120	150	90
4	L	120	150	90
5	L	120	150	90
6	L	120	150	90
7	L	80	150	90
8	L	60	150	90
9	L	120	100	90

10	L	120	100	90
11	R	120	150	90
12	R	120	150	90
13	R	120	150	90
14	R	120	150	90
15	R	110	150	90
16	R	80	150	90
17	R	60	100	90
18	R	60	100	90

Table 5-2. First pass schedule.

Pass	Manipulator	Stroke (mm)	Bite (mm)	Rotation (º)
1	L	120	150	90
2	L	100	150	90
3	L	60	100	45
4	L	140	150	90
5	L	140	150	90
6	L	100	100	90
7	L	110	100	45
8	R	120	150	90
9	R	100	150	90
10	R	60	100	45
11	R	140	150	90
12	R	140	150	90
13	R	100	150	90
14	R	110	100	90

Table 5-3. Second pass schedule.

Pass	Manipulator	Stroke (mm)	Bite (mm)	Rotation (º)
1	R	-	-	-
2	R	90	30	+40
3	R	70	35	+35
4	R	30	15	-18

Table 5-4. Third pass schedule.

5.1.2. Simulation settings

When the process is defined, the simulation is designed to reproduce it. But, first, the hypothesis and the parameter have to be set:

- The stress-strain analysis was performed adopting a 3D model with no symmetry.
- Eighty seconds of air transfer was considered before getting the bar into the water.
- Stress and thermal calculation were considered in the simulation.
- Microstructure calculation was considered in the simulation.

Then, the physical properties of stainless-steel, temperature-dependent, thermal and mechanical properties for the Alloy 28 are defined, extracted from the recommended values of thermos-physical properties for the selected commercial-grade:

Specific Heat	700 J/GMC
Density	Kg/m³
Conductivity	30 w/mK
Epsilon	0.88 (-)

Table 5-5. Physical properties for the Alloy 28 used in the simulation.

For mechanical properties, the Hansell-Spittel model is obtained using input the tensile strain-stress curves of the material (Figure 5-4), which were provided by the manufacturer extracted from internal trials from other processes. The equation used is a simplified version of Equation (57):

$$\sigma = Ae^{m_1 T}\,\varepsilon^{m_2}\,e^{\frac{m_4}{\varepsilon}}\,\dot{\varepsilon}^{m_3}\,, \tag{63}$$

and the corresponding variables for the industrial validated Alloy 28 are exposed in Table 5-6:

HS Variables				
A	**m_1**	**m_2**	**m_3**	**m_4**
22000	-0.004	-0.1	0.17	-0.024

Table 5-6. Industrial validated H-S Variables for Alloy 28.

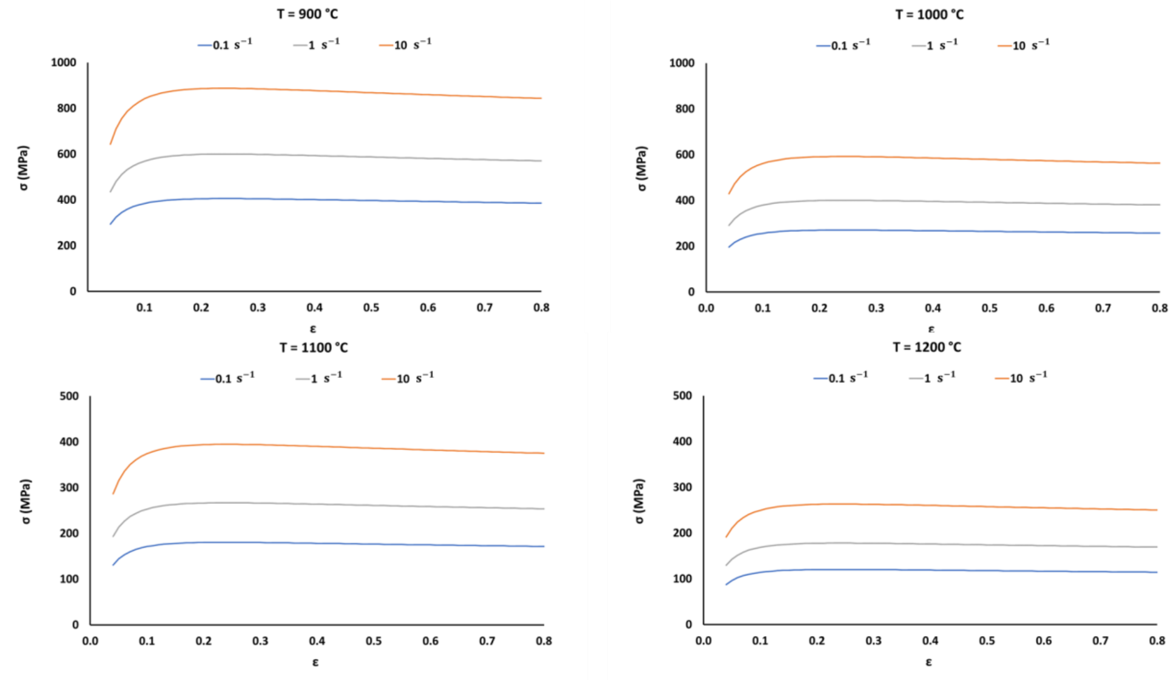

Figure 5-4. H-S approach using industrial validated Alloy 38 Strain-Stress curves given by the manufacturer.

The analysis is divided into the stages described in Figure 5-2, including 2 transition stages and the corresponding heating between forges. For consideration in a thermal calculation, the time step is defined as 2, which means 2 seconds per step. The time step is defined as free for the rest of the simulation.

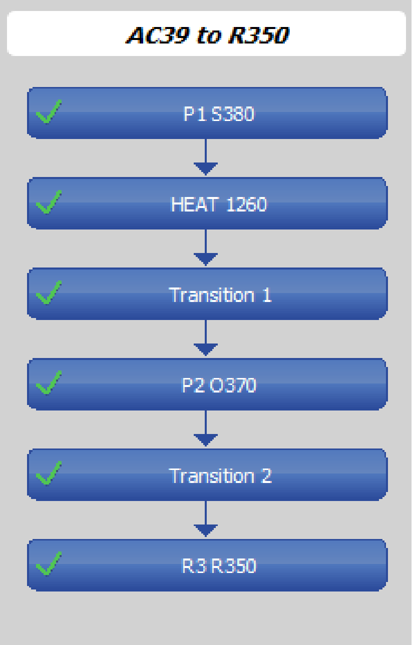

Figure 5-5. Simulation steps.

Simulation set-up is prepared as shown schematically in Figure 5-6.

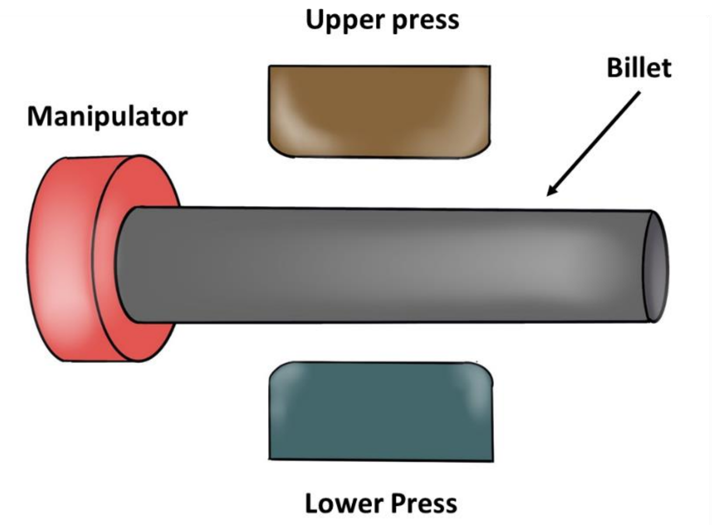

Figure 5-6. Schematic set-up of the simulation.

. The Finite Element (FE) model is generated using 3D tetrahedral elements, establishing the volume size factor as 1.1 and Length 24 mm. Also, remeshing is considered during the simulation, along with the heterogeneity of the initial structure, defining finer size for the billet edge and coarser size in the centre.

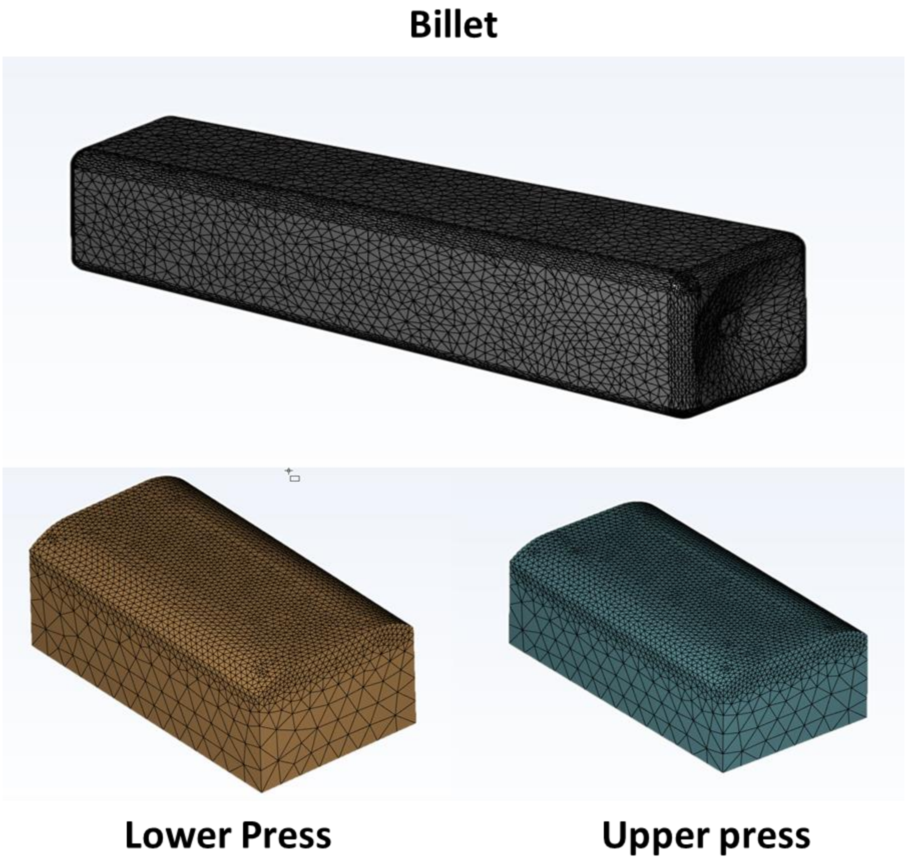

Figure 5-7. Mesh details in the simulation elements.

5.2. Model Validation

For model validation, the reference model based on a generic SASS and adapted to the industrial process for Alloy 28 is presented, followed by the model obtained in the current work, which takes into account DRX and DRV for the Alloy 28.

The H-S approach obtained for the reference model is applied to compare both models, focusing on microstructural evolution. The corresponding recrystallization material parameters for each case are used.

5.2.1. Reference model

The manufacturer provides the reference model that validates Alloy 28 for the studied manufacturing process in the industrial environment. The corresponding input for the software display is shown in Figure 5-8.

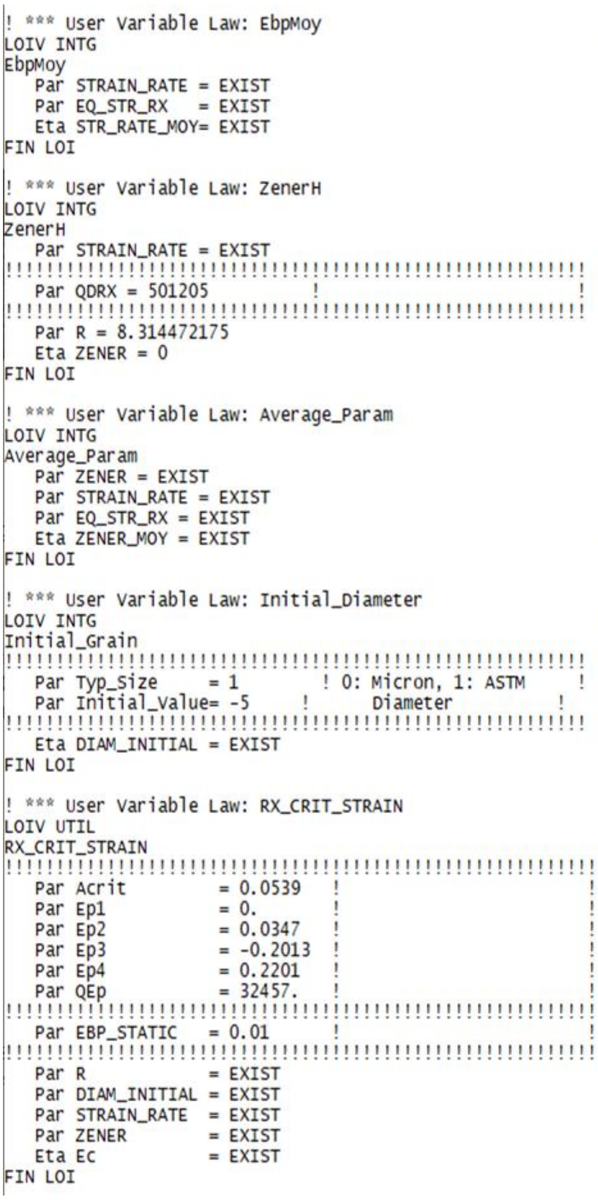

```
! *** User Variable Law: EbpMoy
LOIV INTG
EbpMoy
   Par STRAIN_RATE = EXIST
   Par EQ_STR_RX   = EXIST
   Eta STR_RATE_MOY= EXIST
FIN LOI

! *** User Variable Law: ZenerH
LOIV INTG
ZenerH
   Par STRAIN_RATE = EXIST
!!!!!!!!!!!!!!!!!!!!!!!!!!!!!!!!!!!!!!!!!!!!!!!!!!!!!!!!!
   Par QDRX = 501205            !                       !
!!!!!!!!!!!!!!!!!!!!!!!!!!!!!!!!!!!!!!!!!!!!!!!!!!!!!!!!!
   Par R = 8.314472175
   Eta ZENER = 0
FIN LOI

! *** User Variable Law: Average_Param
LOIV INTG
Average_Param
   Par ZENER = EXIST
   Par STRAIN_RATE = EXIST
   Par EQ_STR_RX = EXIST
   Eta ZENER_MOY = EXIST
FIN LOI

! *** User Variable Law: Initial_Diameter
LOIV INTG
Initial_Grain
!!!!!!!!!!!!!!!!!!!!!!!!!!!!!!!!!!!!!!!!!!!!!!!!!!!!!!!!!
   Par Typ_Size     = 1        ! 0: Micron, 1: ASTM     !
   Par Initial_Value= -5     !      Diameter           !
!!!!!!!!!!!!!!!!!!!!!!!!!!!!!!!!!!!!!!!!!!!!!!!!!!!!!!!!!
   Eta DIAM_INITIAL = EXIST
FIN LOI

! *** User Variable Law: RX_CRIT_STRAIN
LOIV UTIL
RX_CRIT_STRAIN
!!!!!!!!!!!!!!!!!!!!!!!!!!!!!!!!!!!!!!!!!!!!!!!!!!!!!!!!!!
   Par Acrit         = 0.0539  !                        !
   Par Ep1           = 0.      !                        !
   Par Ep2           = 0.0347  !                        !
   Par Ep3           = -0.2013 !                        !
   Par Ep4           = 0.2201  !                        !
   Par QEp           = 32457.  !                        !
!!!!!!!!!!!!!!!!!!!!!!!!!!!!!!!!!!!!!!!!!!!!!!!!!!!!!!!!!!
   Par EBP_STATIC   = 0.01     !                        !
!!!!!!!!!!!!!!!!!!!!!!!!!!!!!!!!!!!!!!!!!!!!!!!!!!!!!!!!!!
   Par R            = EXIST
   Par DIAM_INITIAL = EXIST
   Par STRAIN_RATE  = EXIST
   Par ZENER        = EXIST
   Eta Ec           = EXIST
FIN LOI
```

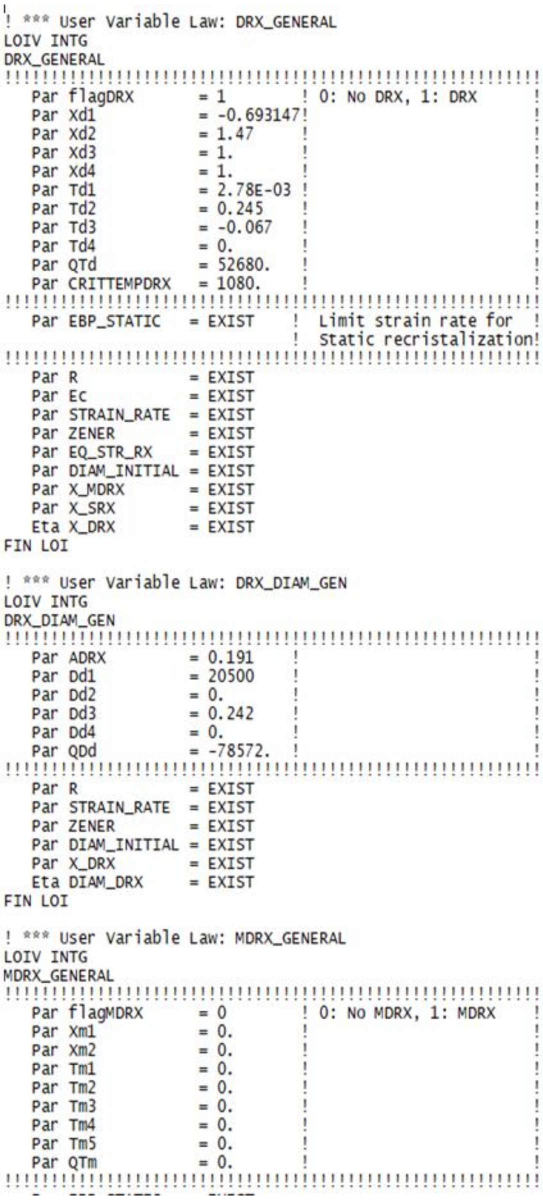

```
! *** User Variable Law: DRX_GENERAL
LOIV INTG
DRX_GENERAL
!!!!!!!!!!!!!!!!!!!!!!!!!!!!!!!!!!!!!!!!!!!!!!!!!!!!!!!!!!!
   Par flagDRX       = 1        ! 0: No DRX, 1: DRX       !
   Par Xd1           = -0.693147!                         !
   Par Xd2           = 1.47     !                         !
   Par Xd3           = 1.       !                         !
   Par Xd4           = 1.       !                         !
   Par Td1           = 2.78E-03 !                         !
   Par Td2           = 0.245    !                         !
   Par Td3           = -0.067   !                         !
   Par Td4           = 0.       !                         !
   Par QTd           = 52680.   !                         !
   Par CRITTEMPDRX   = 1080.    !                         !
!!!!!!!!!!!!!!!!!!!!!!!!!!!!!!!!!!!!!!!!!!!!!!!!!!!!!!!!!!!
   Par EBP_STATIC   = EXIST    !  Limit strain rate for  !
                               !  Static recristalization!
!!!!!!!!!!!!!!!!!!!!!!!!!!!!!!!!!!!!!!!!!!!!!!!!!!!!!!!!!!!
   Par R            = EXIST
   Par Ec           = EXIST
   Par STRAIN_RATE  = EXIST
   Par ZENER        = EXIST
   Par EQ_STR_RX    = EXIST
   Par DIAM_INITIAL = EXIST
   Par X_MDRX       = EXIST
   Par X_SRX        = EXIST
   Eta X_DRX        = EXIST
FIN LOI

! *** User Variable Law: DRX_DIAM_GEN
LOIV INTG
DRX_DIAM_GEN
!!!!!!!!!!!!!!!!!!!!!!!!!!!!!!!!!!!!!!!!!!!!!!!!!!!!!!!!!!!
   Par ADRX         = 0.191    !                          !
   Par Dd1          = 20500    !                          !
   Par Dd2          = 0.       !                          !
   Par Dd3          = 0.242    !                          !
   Par Dd4          = 0.       !                          !
   Par QDd          = -78572.  !                          !
!!!!!!!!!!!!!!!!!!!!!!!!!!!!!!!!!!!!!!!!!!!!!!!!!!!!!!!!!!!
   Par R            = EXIST
   Par STRAIN_RATE  = EXIST
   Par ZENER        = EXIST
   Par DIAM_INITIAL = EXIST
   Par X_DRX        = EXIST
   Eta DIAM_DRX     = EXIST
FIN LOI

! *** User Variable Law: MDRX_GENERAL
LOIV INTG
MDRX_GENERAL
!!!!!!!!!!!!!!!!!!!!!!!!!!!!!!!!!!!!!!!!!!!!!!!!!!!!!!!!!!!
   Par flagMDRX      = 0        ! 0: No MDRX, 1: MDRX     !
   Par Xm1           = 0.       !                         !
   Par Xm2           = 0.       !                         !
   Par Tm1           = 0.       !                         !
   Par Tm2           = 0.       !                         !
   Par Tm3           = 0.       !                         !
   Par Tm4           = 0.       !                         !
   Par Tm5           = 0.       !                         !
   Par QTm           = 0.       !                         !
!!!!!!!!!!!!!!!!!!!!!!!!!!!!!!!!!!!!!!!!!!!!!!!!!!!!!!!!!!!
```

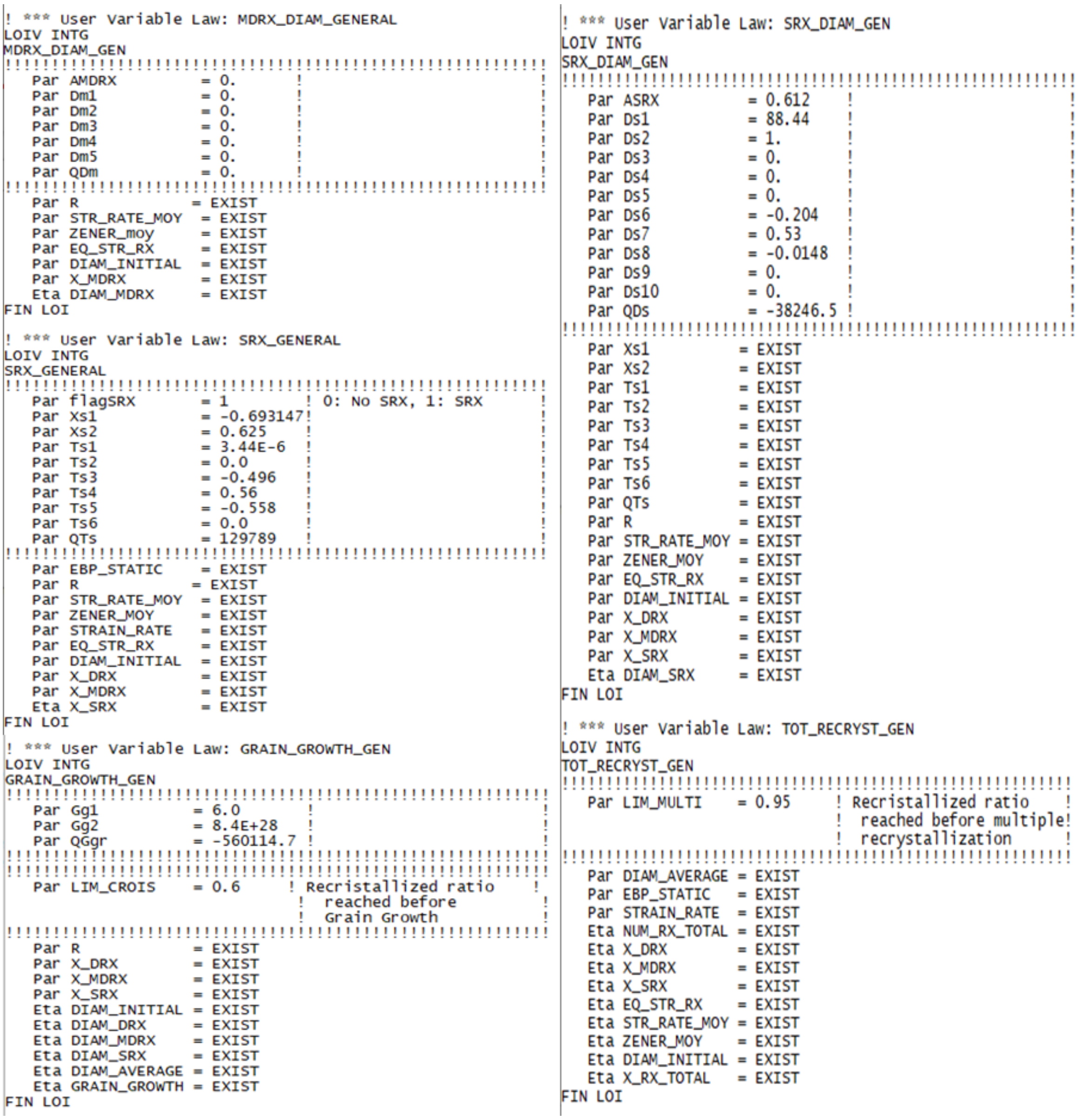

```
! *** User Variable Law: MDRX_DIAM_GENERAL
LOIV INTG
MDRX_DIAM_GEN
!!!!!!!!!!!!!!!!!!!!!!!!!!!!!!!!!!!!!!!!!!!!!!!!!!!!!!!!!!!
   Par AMDRX          = 0.       !                          !
   Par Dm1            = 0.       !                          !
   Par Dm2            = 0.       !                          !
   Par Dm3            = 0.       !                          !
   Par Dm4            = 0.       !                          !
   Par Dm5            = 0.       !                          !
   Par QDm            = 0.       !                          !
!!!!!!!!!!!!!!!!!!!!!!!!!!!!!!!!!!!!!!!!!!!!!!!!!!!!!!!!!!!
   Par R             = EXIST
   Par STR_RATE_MOY   = EXIST
   Par ZENER_moy      = EXIST
   Par EQ_STR_RX      = EXIST
   Par DIAM_INITIAL   = EXIST
   Par X_MDRX         = EXIST
   Eta DIAM_MDRX      = EXIST
FIN LOI

! *** User Variable Law: SRX_GENERAL
LOIV INTG
SRX_GENERAL
!!!!!!!!!!!!!!!!!!!!!!!!!!!!!!!!!!!!!!!!!!!!!!!!!!!!!!!!!!!
   Par flagSRX        = 1         ! 0: No SRX, 1: SRX       !
   Par Xs1            = -0.693147!                          !
   Par Xs2            = 0.625     !                          !
   Par Ts1            = 3.44E-6   !                          !
   Par Ts2            = 0.0       !                          !
   Par Ts3            = -0.496    !                          !
   Par Ts4            = 0.56      !                          !
   Par Ts5            = -0.558    !                          !
   Par Ts6            = 0.0       !                          !
   Par QTs            = 129789    !                          !
!!!!!!!!!!!!!!!!!!!!!!!!!!!!!!!!!!!!!!!!!!!!!!!!!!!!!!!!!!!
   Par EBP_STATIC     = EXIST
   Par R             = EXIST
   Par STR_RATE_MOY   = EXIST
   Par ZENER_MOY      = EXIST
   Par STRAIN_RATE    = EXIST
   Par EQ_STR_RX      = EXIST
   Par DIAM_INITIAL   = EXIST
   Par X_DRX          = EXIST
   Par X_MDRX         = EXIST
   Eta X_SRX          = EXIST
FIN LOI
! *** User Variable Law: GRAIN_GROWTH_GEN
LOIV INTG
GRAIN_GROWTH_GEN
!!!!!!!!!!!!!!!!!!!!!!!!!!!!!!!!!!!!!!!!!!!!!!!!!!!!!!!!!!!
   Par Gg1           = 6.0        !                          !
   Par Gg2           = 8.4E+28    !                          !
   Par QGgr          = -560114.7 !                          !
!!!!!!!!!!!!!!!!!!!!!!!!!!!!!!!!!!!!!!!!!!!!!!!!!!!!!!!!!!!
!!!!!!!!!!!!!!!!!!!!!!!!!!!!!!!!!!!!!!!!!!!!!!!!!!!!!!!!!!!
   Par LIM_CROIS     = 0.6      ! Recristallized ratio    !
                                 !  reached before          !
                                 !  Grain Growth            !
!!!!!!!!!!!!!!!!!!!!!!!!!!!!!!!!!!!!!!!!!!!!!!!!!!!!!!!!!!!
   Par R             = EXIST
   Par X_DRX         = EXIST
   Par X_MDRX        = EXIST
   Par X_SRX         = EXIST
   Eta DIAM_INITIAL = EXIST
   Eta DIAM_DRX      = EXIST
   Eta DIAM_MDRX     = EXIST
   Eta DIAM_SRX      = EXIST
   Eta DIAM_AVERAGE = EXIST
   Eta GRAIN_GROWTH = EXIST
FIN LOI
```

```
! *** User Variable Law: SRX_DIAM_GEN
LOIV INTG
SRX_DIAM_GEN
!!!!!!!!!!!!!!!!!!!!!!!!!!!!!!!!!!!!!!!!!!!!!!!!!!!!!!!!!!!!
   Par ASRX           = 0.612     !                          !
   Par Ds1            = 88.44     !                          !
   Par Ds2            = 1.        !                          !
   Par Ds3            = 0.        !                          !
   Par Ds4            = 0.        !                          !
   Par Ds5            = 0.        !                          !
   Par Ds6            = -0.204    !                          !
   Par Ds7            = 0.53      !                          !
   Par Ds8            = -0.0148   !                          !
   Par Ds9            = 0.        !                          !
   Par Ds10           = 0.        !                          !
   Par QDs            = -38246.5 !                          !
!!!!!!!!!!!!!!!!!!!!!!!!!!!!!!!!!!!!!!!!!!!!!!!!!!!!!!!!!!!!
   Par Xs1           = EXIST
   Par Xs2           = EXIST
   Par Ts1           = EXIST
   Par Ts2           = EXIST
   Par Ts3           = EXIST
   Par Ts4           = EXIST
   Par Ts5           = EXIST
   Par Ts6           = EXIST
   Par QTs           = EXIST
   Par R             = EXIST
   Par STR_RATE_MOY = EXIST
   Par ZENER_MOY     = EXIST
   Par EQ_STR_RX     = EXIST
   Par DIAM_INITIAL = EXIST
   Par X_DRX         = EXIST
   Par X_MDRX        = EXIST
   Par X_SRX         = EXIST
   Eta DIAM_SRX      = EXIST
FIN LOI

! *** User Variable Law: TOT_RECRYST_GEN
LOIV INTG
TOT_RECRYST_GEN
!!!!!!!!!!!!!!!!!!!!!!!!!!!!!!!!!!!!!!!!!!!!!!!!!!!!!!!!!!!!
   Par LIM_MULTI     = 0.95      ! Recristallized ratio    !
                                 !  reached before multiple!
                                 !  recrystallization       !
!!!!!!!!!!!!!!!!!!!!!!!!!!!!!!!!!!!!!!!!!!!!!!!!!!!!!!!!!!!!
   Par DIAM_AVERAGE = EXIST
   Par EBP_STATIC    = EXIST
   Par STRAIN_RATE   = EXIST
   Eta NUM_RX_TOTAL = EXIST
   Eta X_DRX         = EXIST
   Eta X_MDRX        = EXIST
   Eta X_SRX         = EXIST
   Eta EQ_STR_RX     = EXIST
   Eta STR_RATE_MOY = EXIST
   Eta ZENER_MOY     = EXIST
   Eta DIAM_INITIAL = EXIST
   Eta X_RX_TOTAL    = EXIST
FIN LOI
```

Figure 5-8. Reference model file for the Alloy 28 validated at industrial environment.

When the material record is set, the results obtained are shown in the next subsections following the three stages of the process as shown in Figure 5-2. For each stage, the cross-section of the ingot is shown to display the distribution of the following parameters along with the specimen: Temperature, Strain and ASTM grain diameter.

5.2.1.1. First Stage

For the first stage's analysis, the temperature distribution is observed in Figure 5-7, where the centre of the billet maintains an even increase in its temperature up to 1300 ºC, while it decreases in the edge down to 900 ºC creating a temperature gradient.

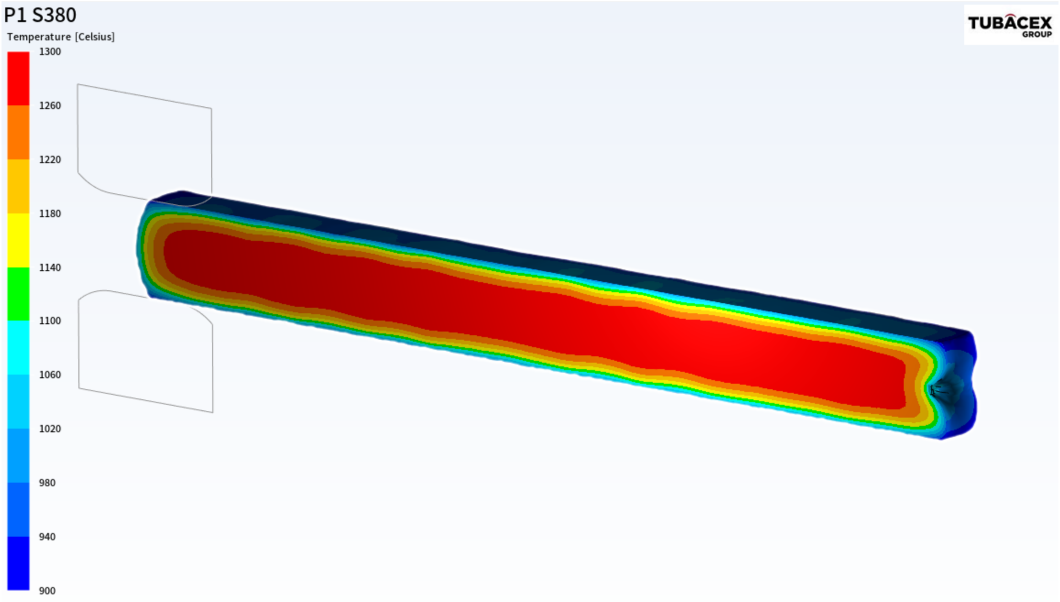

Figure 5-9. Temperature distribution after the first stage.

Figure 5-10 shows a heterogeneous strain distribution, with high strains in the centre and deformation-free areas in the spaces between passes on the surface.

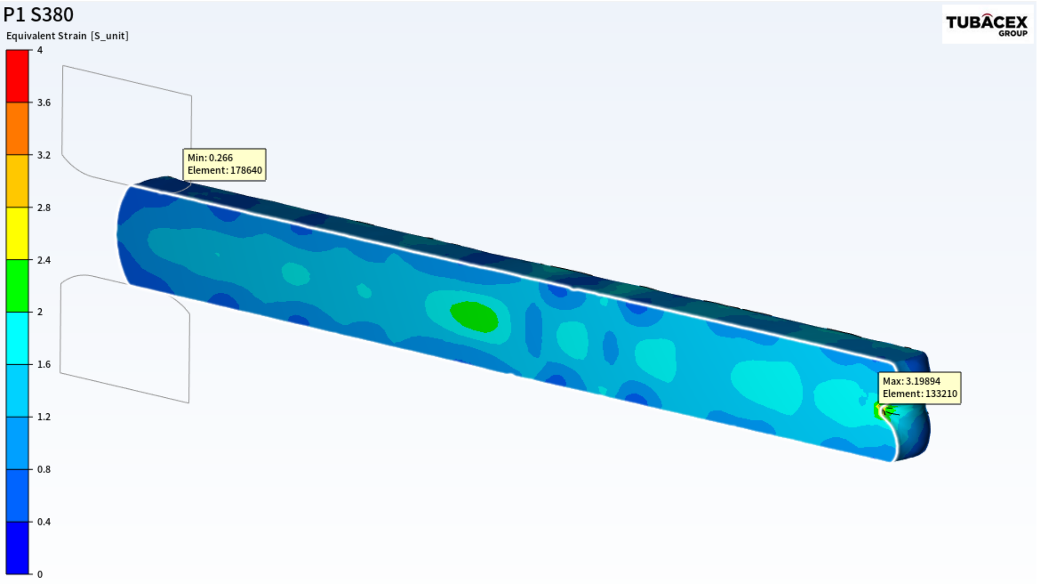

Figure 5-10. Plastic strain distribution after the first satage.

Finally, for this first stage, the ASTM diameter is shown in Figure 5-11, where the grain size is coarse, far from the desired fine grain. However, the trend towards coarse grain at the edge versus a more refined grain in the centre is observed, related to different temperatures and strain along the radial axis as it was observed in Figure 5-9 and Figure 5-10, and agree with the literature. At higher deformation and temperature are, a more refined grain is obtained and shown in Figure 5-12, where the detail of the transversal section of the first stage.

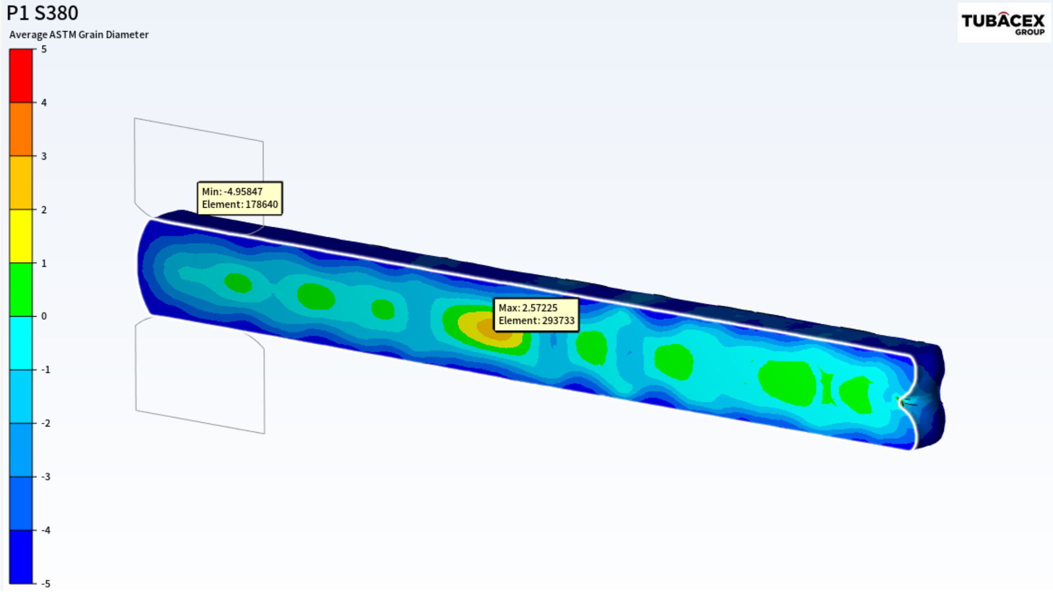

Figure 5-11. ASTM grain diameter distribution after the first stage.

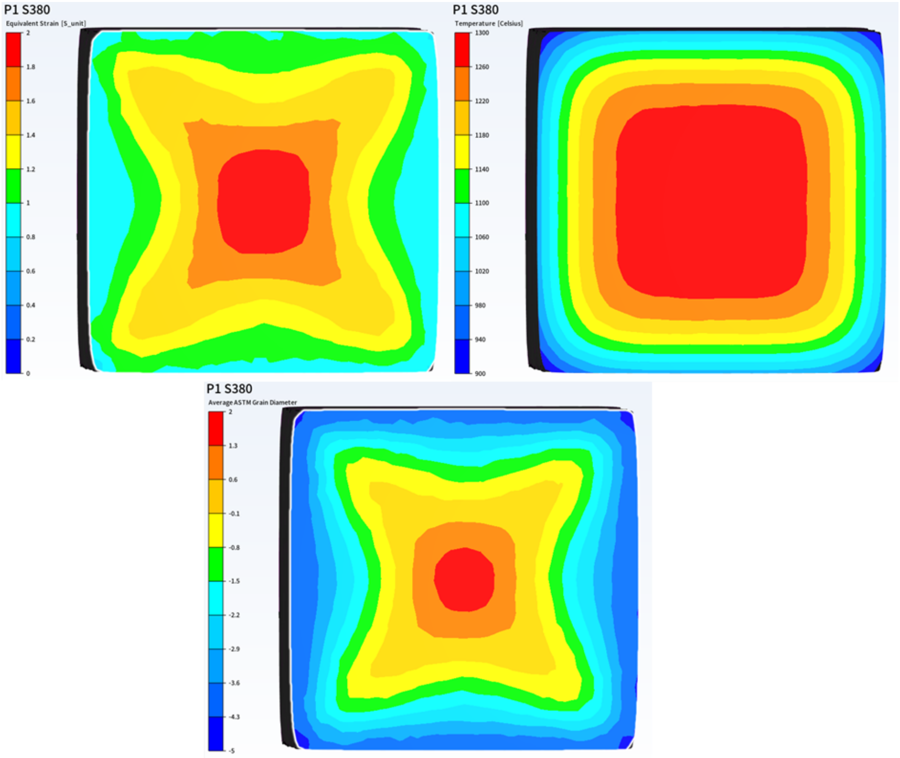

Figure 5-12. First stage S380. Plastic strain, Temperature, ASTM grain diameter.

5.2.1.2. Second Stage

After the heating transition, the second stage is initiated. The temperature distribution is observed in Figure 5-13, where the centre temperature decreases to 1250 °C while the edge keeps the same temperature due to the bar surface cooling, as seen in the previous stage.

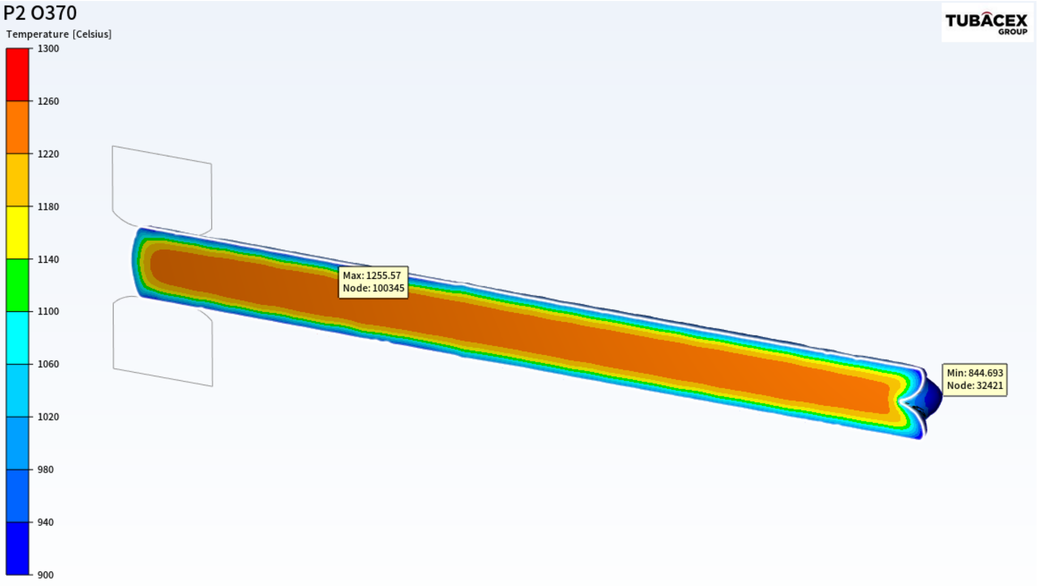

Figure 5-13. Temperature distribution after the second stage.

From the strain distribution in Figure 5-14, the deformation increases with regards to the previous stage and continues with the previously observed heterogeneity with a higher deformation in the centre.

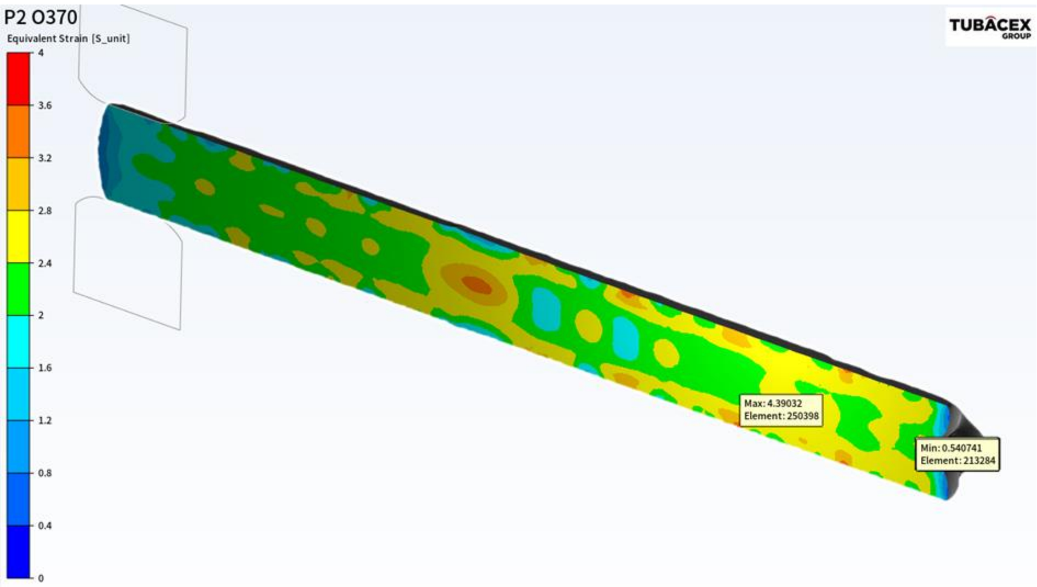

Figure 5-14. Plastic strain distribution after the second stage.

For the grain size observations, Figure 5-15 shows how the grain size refines at the centre while in the surface remains coarse due to temperature and deformation gradient observed in Figure 5-13 and Figure 5-14, and summarized, in Figure 5-16, where the cross-section of the octagonal bar is shown.

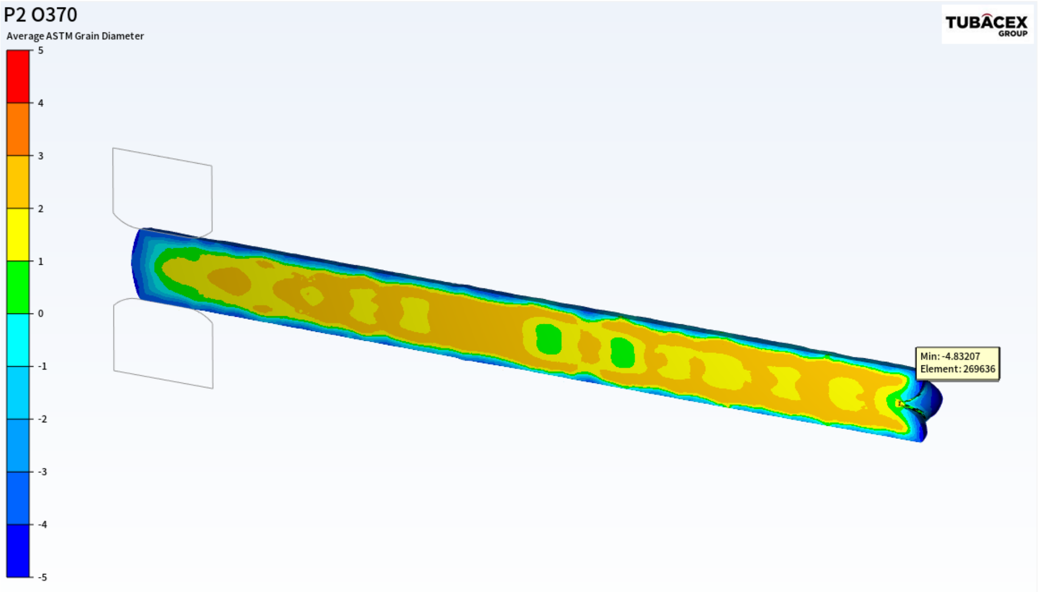

Figure 5-15. ASTM grain siameter distribution after the first stage.

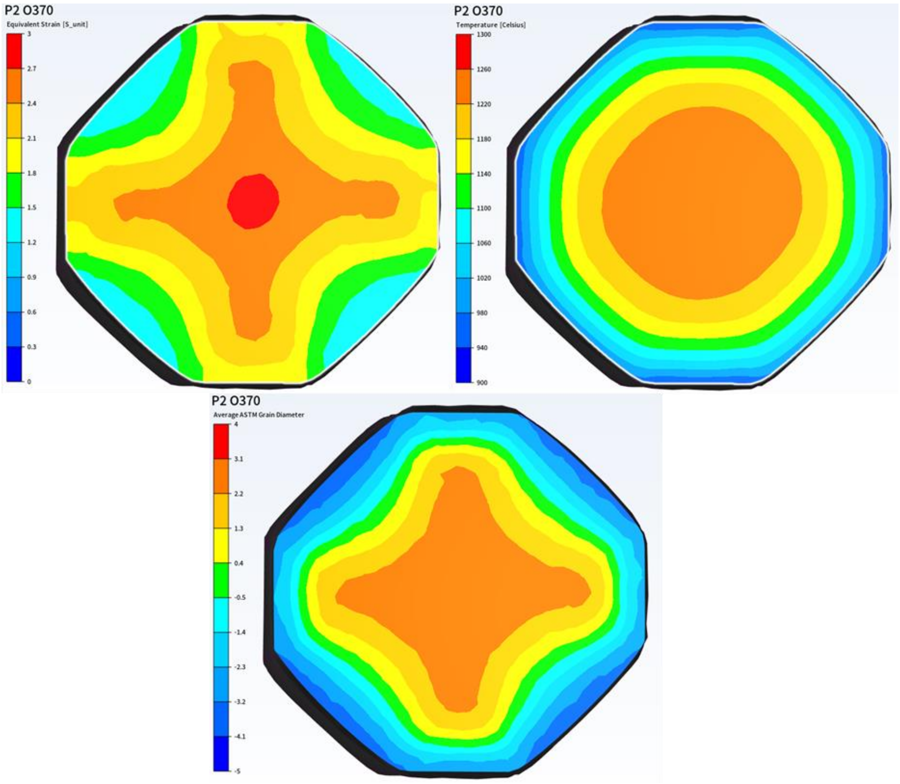

Figure 5-16. Second stage O370. Plastic strain, Temperature, ASTM grain diameter.

5.2.1.3. Third Stage

In Figure 5-17, the temperature distribution and the gradient observed between the edge and the centre remains.

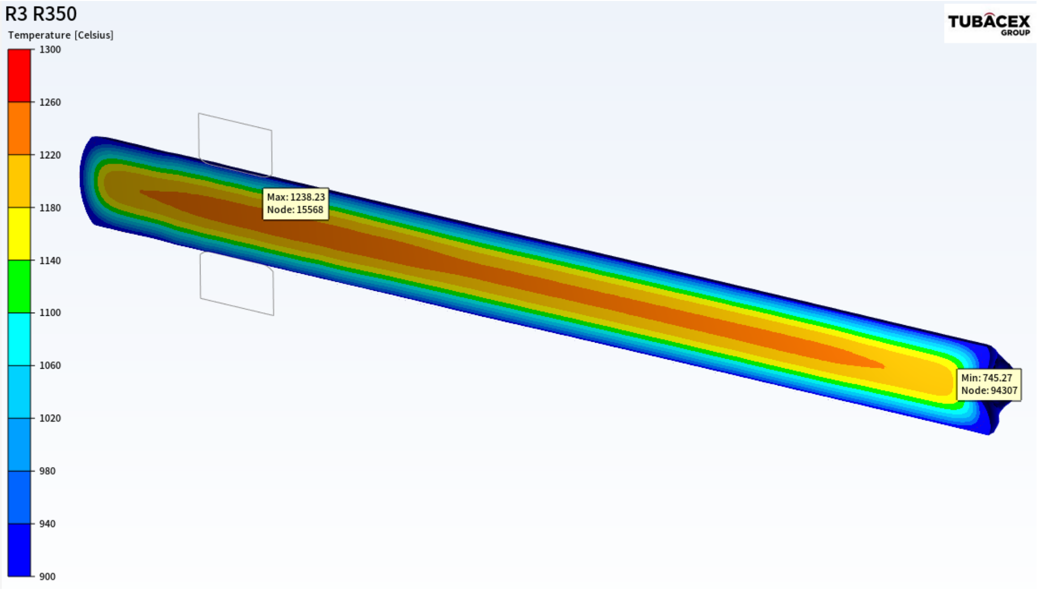

Figure 5-17. Temperature distribution after the third stage.

It is noticed from Figure 5-18 that the strain distribution is not homogeneous, and the centre presents a higher deformation than the edge and also one of the ends concerning the other. From this observation, it can be deduced that the strain distribution along the longitudinal axis during forging is not homogeneous.

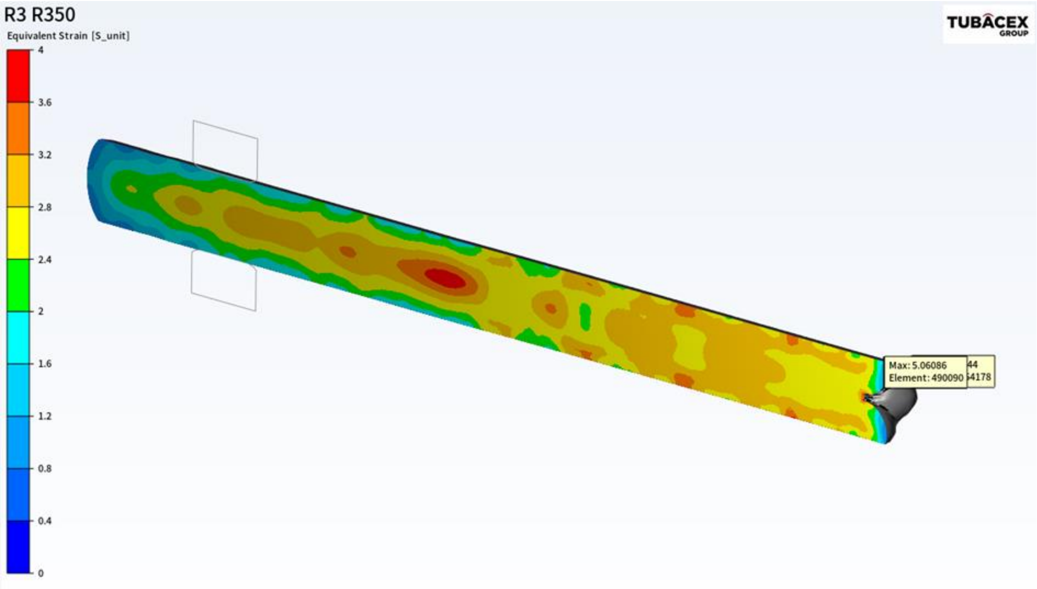

Figure 5-18. Plastic strain distribution after the third stage.

A homogeneous fine grain distribution is observed in Figure 5-19, which agrees with the analysed round bar back in Section 4.3, presenting refined grain in the centre with a small area of coarse grains due to the gradient of both strain and temperature.

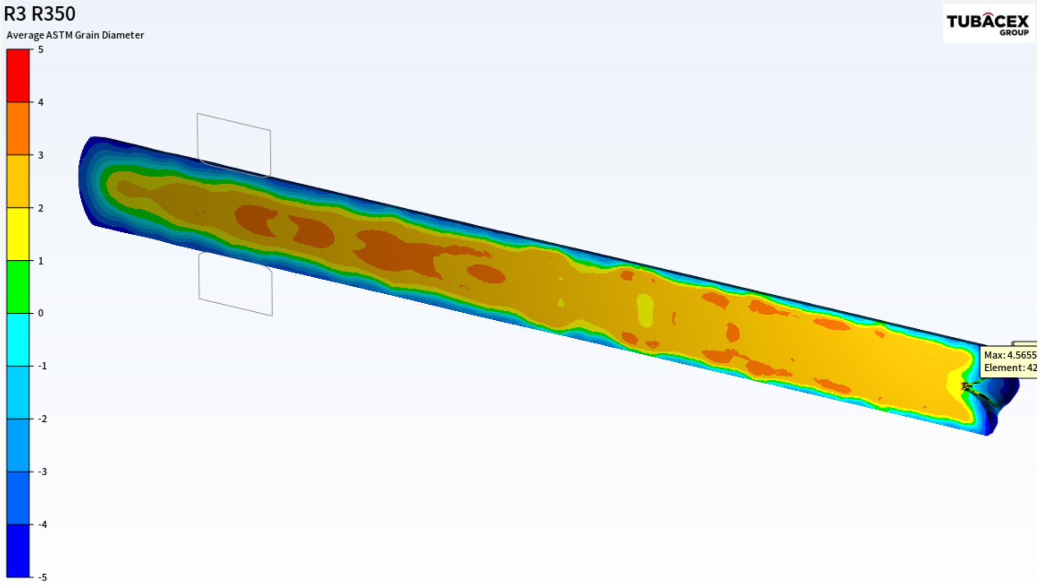

Figure 5-19. ASTM grain diameter distribution after the third stage.

Finally, the cross-section of the final bar is presented in Figure 5-20. Again, the expected distribution in the ASTM grain diameter distribution is shown, which essentially agrees with the final round bar.

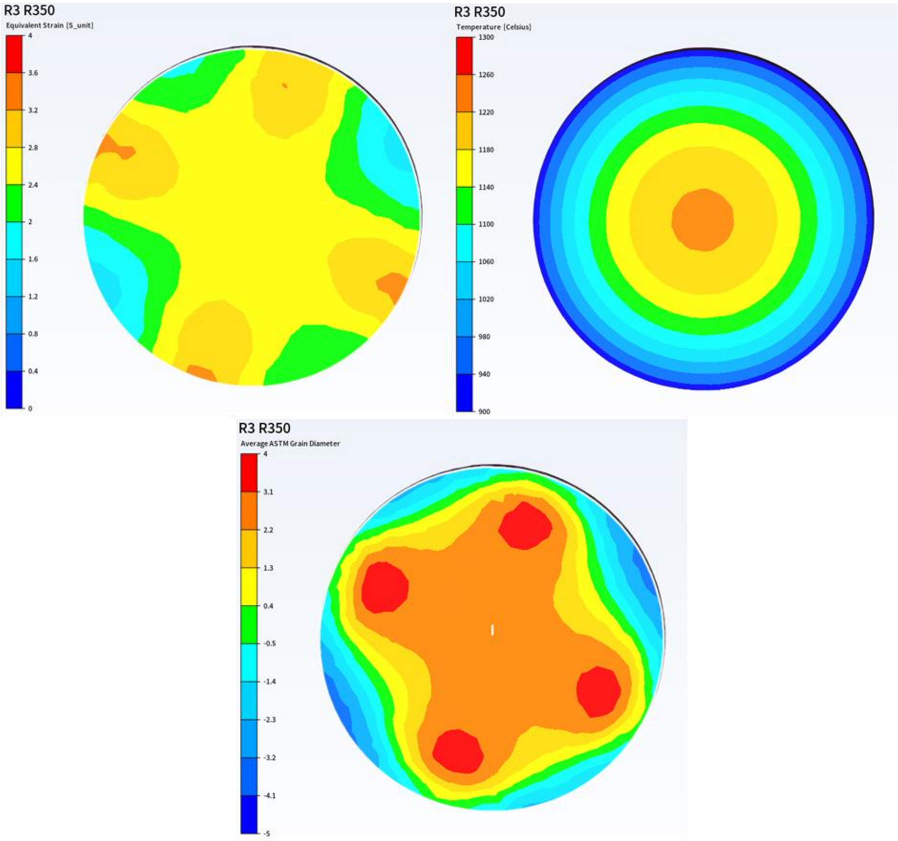

Figure 5-20. Third stage R350. Plastic strain, Temperature, ASTM grain diameter.

5.2.1.4. Summary

The evolution of the forged bar during the process is shown below for three parameters: Average strain rate (Figure 5-21), χ_{DRX} and grain growth.

For the average strain rate (Figure 5-21), it can be seen that strain lines appear on the surface during the second stage because the forging does not provide a homogeneous stress distribution causing areas of high strain. However, the strain becomes more homogeneous in the transversal section when the forging is complete.

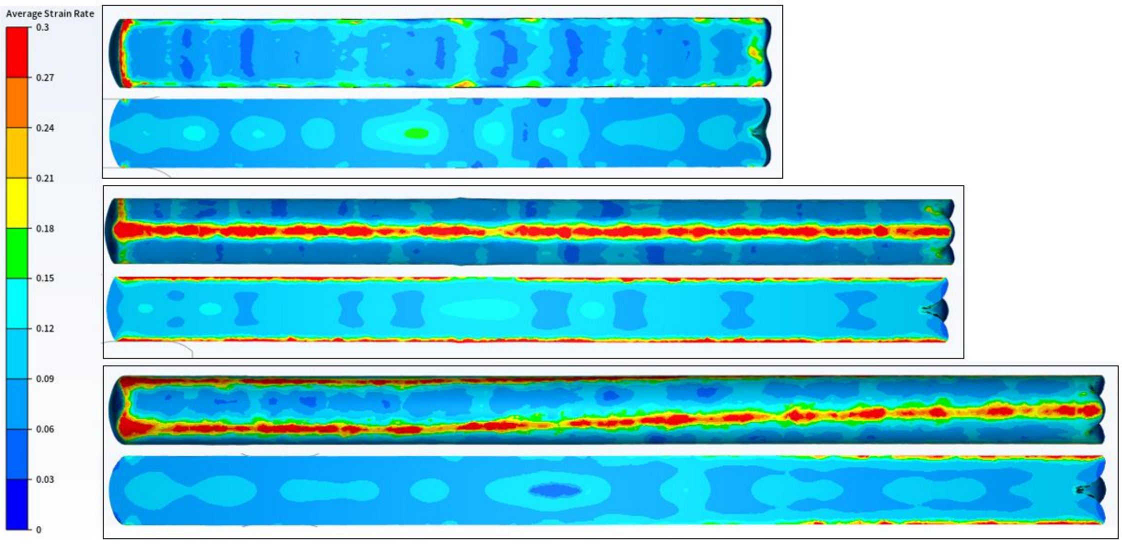

Figure 5-21. Average strain rate values in all stages.

The dynamic recrystallization fraction (Figure 5-22) indicates the amount of recrystallized material. χ_{DRX} is higher in the centre, which indicates that the conditions in this area are optimal for the recrystallization to occur. On the other hand, because of the temperature and strain gradient mentioned above, the χ_{DRX} is lower on the surface and in any location where the strain decreases.

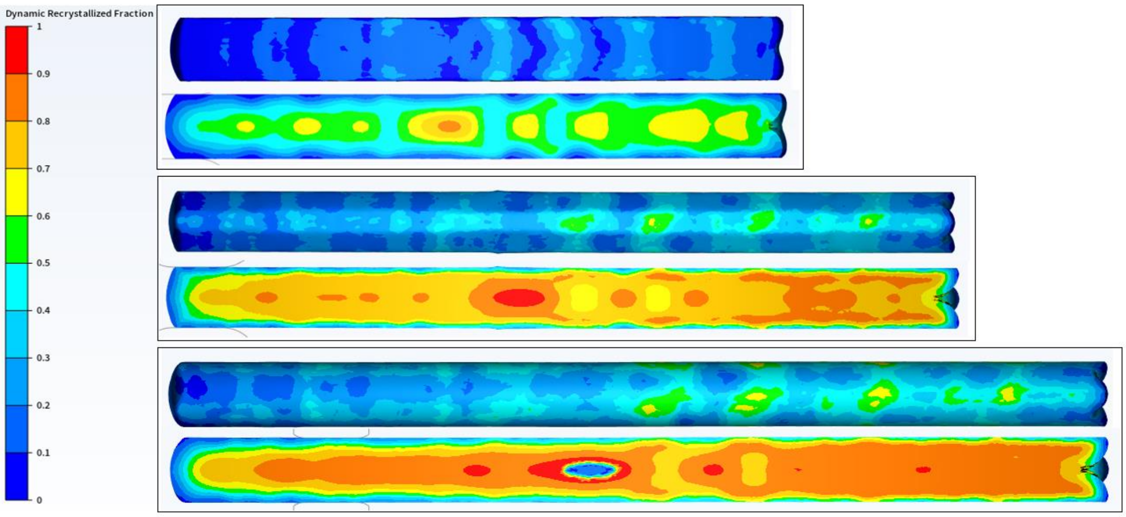

Figure 5-22. Dynamic recrystallization fraction values in all stages.

5.2.2. DRX experimental model

The experimental model developed is tested below, whose parameters were obtained in Section 4 and are shown in Table 4-7, Table 4-8 and Table 4-9. The code used in Figure 5-6 uses the variables obtained for the phenomenological model for DRX and DRV and avoids the effect of SRX, MDRX and grain growth (GG). For the validation, the focus is on ASTM grain size and χ_{DRX} output, since the distribution of temperatures and deformations are the same as the reference model.

5.2.2.1. First Stage

In Figure 5-21, the ASTM grain size distribution shows significant differences regarding the reference model. A remarkable difference between the edge and centre is appreciated. The grains are larger as temperature and strain decrease compared to the centre, where the grain is much more refined. This indicates that this approach is much more sensitive to temperature and strain changes, and the recrystallization speed is faster than the reference model.

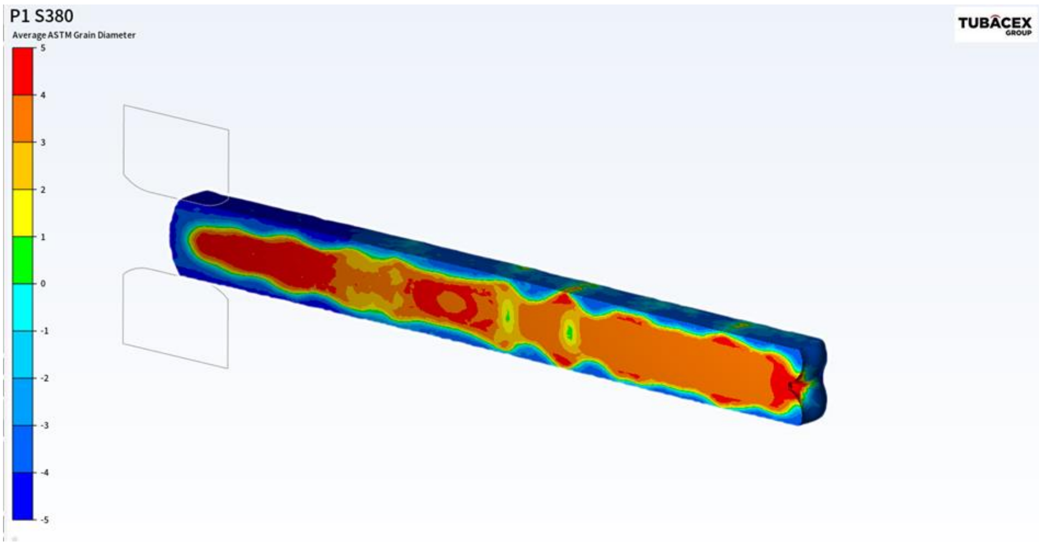

Figure 5-23. ASTM grain diameter after the first stage.

In Figure 5-24, the cross-section shows the heterogeneity described above. Due to local nucleation that generates a more active recrystallisation ratio, a high concentration of refined grains is present in the corners of the deformed area.

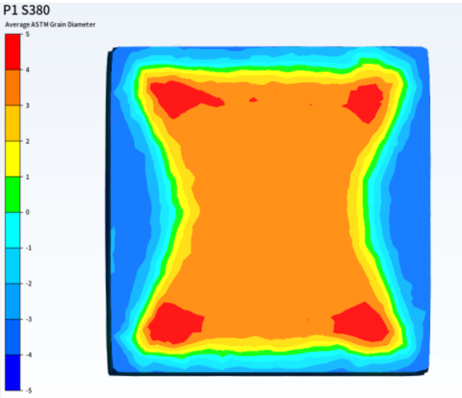

Figure 5-24. First stage S380. ASTM grain diameter.

5.2.2.2. Second Stage

In Figure 5-25 grain size becomes finner, excluding a few areas with coarse grain sizes in the edge. However, a heterogeneous distribution is shown because the right side of the bar presents a larger grain size, which is directly related to the strain distribution in the longitudinal section of the billet shown in Figure 5-14.

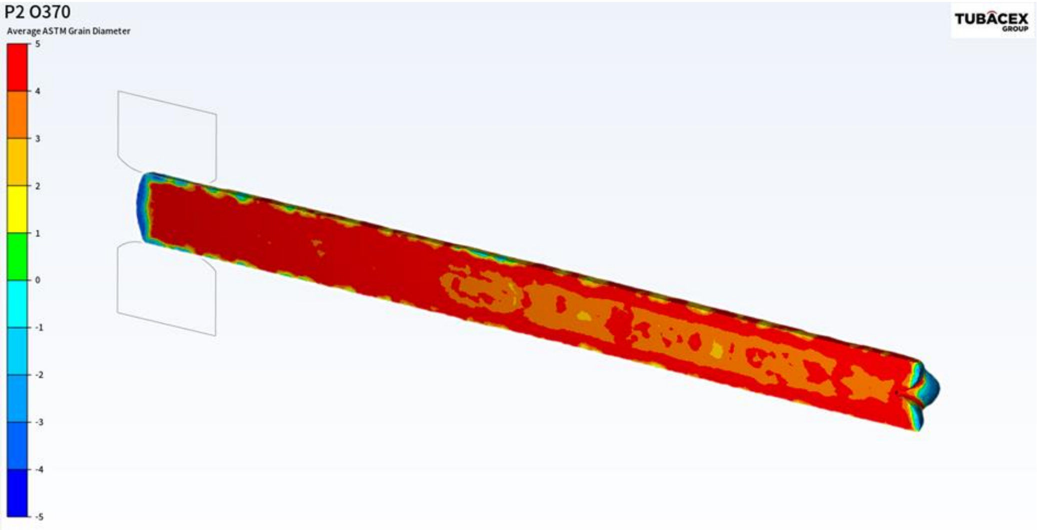

Figure 5-25. ASTM grain diameter after the second stage.

The octagonal bar cross-section is shown in Figure 5-26, where the heterogeneity described in the centre, where a coarser grain surrounded by a refiner grain distribution, is appreciated. In the edges, remaining areas with coarser grain sizes are shown, corresponding with the corners of the section.

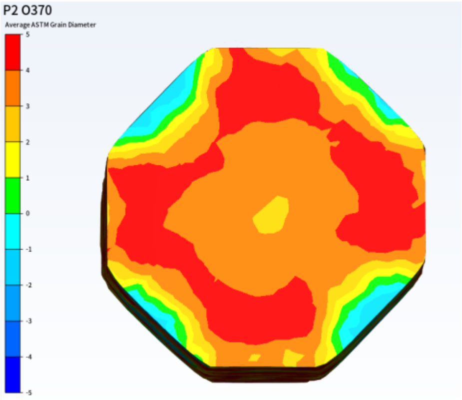

Figure 5-26. Second stage O370. ASTM grain diameter.

5.2.2.3. Third Stage

A complete recrystallized area is appreciated in Figure 5-27 with a heterogeneous fine grain size distribution, as shown in Figure 5-28. The results obtained are a fine-grained homogeneous structure desired after the forging but do not match with the forging bar structure studied in Section 4.3. Therefore, a first conclusion is made: the model obtained does not fulfil the expected results.

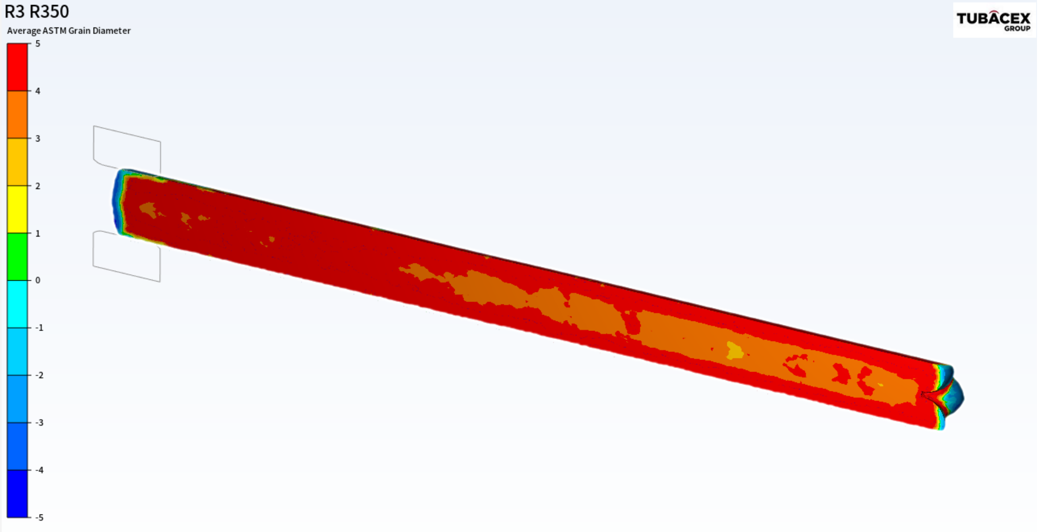

Figure 5-27. ASTM grain diameter after the third stage.

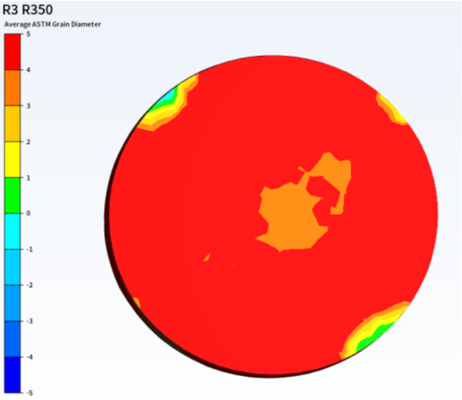

Figure 5-28. Thrid stage R350. ASTM grain diameter.

5.2.2.4. Summary

Figure 5-27 shows the dynamic recrystallization fraction evolution during the process. It has been seen that the grain refines as the process progress, but there is no increase in χ_{drv} and the software output presents a high grain refining but not a fully recrystallized material. From this behaviour, it is concluded that post-dynamic recrystallisation highly influences

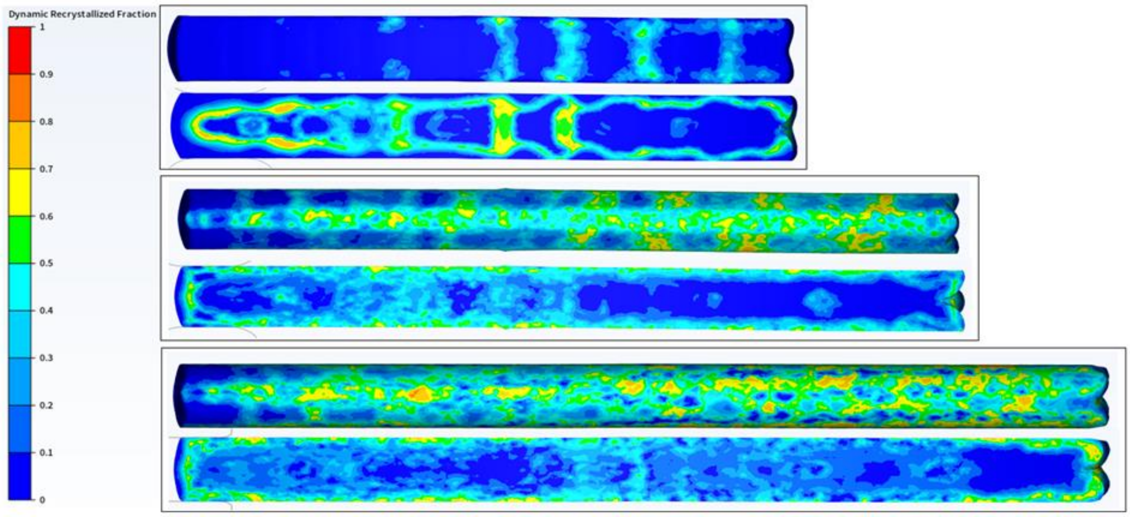

Figure 5-29. Dynamic recrystallization fraction values in all stages.

5.3. Discussion on the model

The critical analysis of the results obtained above is discussed., The mechanical models used in the simulation are compared with the experimental data, and then the accuracy of the experimental model is discussed.

5.3.1. Simulation groundwork

The results from the H-S model are analysed. Compression tests recreate the forces during the forging process for the experimental case. For industrial validation purposes, tensile curves are used because they allow higher plasticity and avoid the effects of friction that appear during compression. Cyclic stress-strain curves, known as whöler curves, show the relationship between compression and tensile behaviour. When this curve is symmetric, the tensile and compression values are equivalent [119].

In Figure 5-30, a)) [2], the cyclic stress-strain curves corresponding to wrought Alloy 28 shows symmetry, which indicates the equivalence between tensile and compression values [119]. However, the welded material (Figure 5-30, b)) presents a lower plastic character related to the initial microstructure, with coarse grain and dendritic structure. Consequently, the discrepancies between the curves from the H-S model from the reference model and the studied are related to the initial grain size, which provides nonsymmetric whöler curves. In addition, the reference model cannot fully interpolate the mechanical behaviour because it does not consider critical factors such as friction and initial microstructural structure.

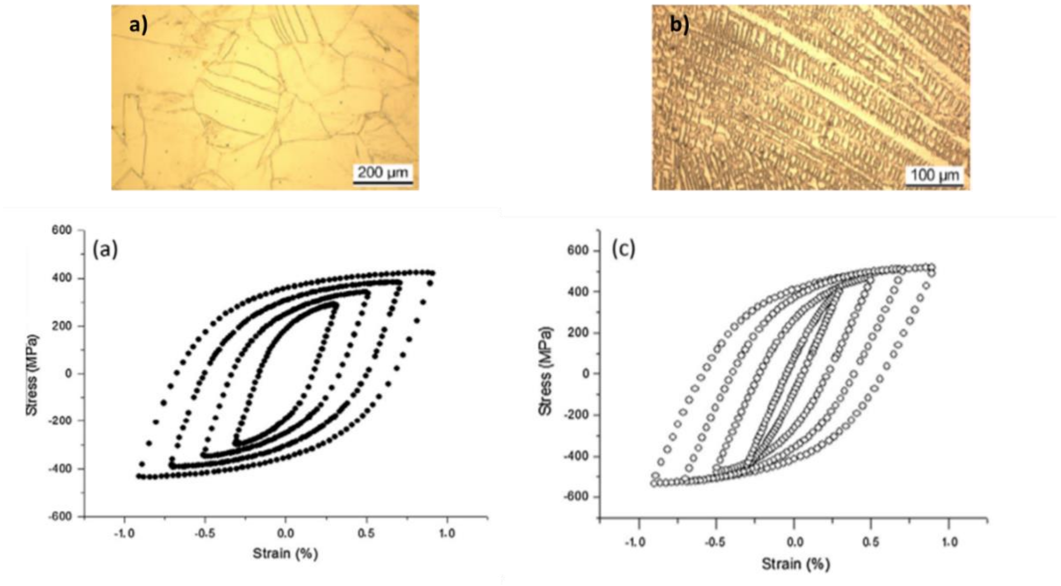

Figure 5-30. Stress-Strain curves and the corresponding microstructure for a) Wrought vs b) Welded [2].

5.3.2. Model Validation

For model validation, the accuracy of the reference model and faults of the experimental are discussed.

The reference model fulfils the functionality of the simulated process, obtaining the final result studied in Section 4. However, the parameters used for the adjustment have not been obtained experimentally and are based on the final bar structure. This makes the microstructural behaviour not extrapolated since the internal phenomena are not considered despite the model fulfil the specifications and responding to the final input.

The experimental model obtained does not fulfil the expected behaviour. The round bar presents a refined grain size with a low recrystallization fraction which distribution does not agree with the temperature and strain gradients. The material keeps recrystallising when the strain stops, but the working temperature is maintained, as seen in the reference model. This concludes that PDRX strongly influences the process and needs to be considered for modelization.

The proposed experimental model is inaccurate because it does not optimally predict the microstructure because only DRV and DRX are considered, and post-dynamic recrystallization has a critical role in the process.

5.4. Summary

The model obtained in Section 4 is validated using Forge ® software. Then, it is compared with an industrially validated reference model provided by the manufacturer.

Process conditions and parameters are shown first, followed by the simulation setup. Then, results from both models are shown and discussed. Finally, the critical analysis of the model is presented, and the conclusions are then drawn.

6. CONCLUSIONS AND FUTURE WORK

In this chapter, the modelling conclusions are made, followed by a future work proposal.

6.1. Conclusions

The work presented in this thesis describes the hot working behaviour, including hardening, recovery and recrystallization for the As-cast Alloy 28 SASS during an open die forging process.

Extensive research was conducted on the transformation phenomenon during hot working. A review of which is presented in Chapter 2, focusing on recrystallization in LSFE materials to provide a phenomenological based numerical model that predicts the microstructure evolution under multi-pass conditions with acceptable accuracy in an industrial environment.

Experiments were conducted to validate the model. First, the compression test parameters were identified, and the test was carried out at different temperatures and strain rates for a set strain. After that, the results were treated and analysed to obtain the critical initiation parameters for recrystallization. Then, the resulting microstructures were analysed, obtaining the recrystallized volume fraction and grain size using optical microstructure and EBSD analysis, as explained in Section 3.

In chapter 4, the results from the experimental methodology were obtained. The critical parameters to the initiation of DRX showed that the recrystallization starts earlier than was reviewed in literature for the wrought Alloy 28 [118], which is related to the initial structure because coarse grains present larger grain boundaries that allow the new nuclei to grow. However, from the DRX parameters D_{drx} and χ_{drx} it was observed that the recrystallization does not fully develop. Since only DRV and DRX were studied, the deformation energy is insufficient for the coarse grain to be fully recrystallized despite the early nuclei formation. This also indicates the significant effect of PDRX because it allows to reach a fully recrystallized microstructure. This hypothesis was validated in Chapter 5 when the material parameters are introduced to the material model and implemented in the process simulation.

In Chapter 5, the experimental model was set up using the software Forge ® and compared with an industrially validated model provided by the manufacturer. The reference model simulation shows an accurate approach to what was expected regarding recrystallization and grains size for the forged bar studied in Chapter 4. However, no recrystallization was observed while a fully refined grain structure appeared. This confirmed the previously made hypothesis: PDRX plays a fundamental role in the recrystallization dynamic and needs to be considered to develop the material model.

6.2. Future work

According to the results of this study, the following suggestions are given for future work.

Even though experiments are conducted in various temperature and strain rates conditions, more investigation on a broader range will allow a more accurate prediction in variable strain rate and temperature conditions. The proposed model identifies parameters values depending on the recrystallization regime DRX. Ideally, one would look for a unified model valid in all regimes. In that case, multipass recrystallization (DRX+SRX+GG, DRX+PDRX+GG) is needed for the model's accuracy for multi-pass conditions to be modelled.

Because PDRX plays a fundamental role in the process, two steep hot-compression tests for PDRX and annealing tests for grain growth are proposed for future research work to obtain the corresponding parameters to implement.

In addition, softwares like DIGIMU® provide information on the transformation phenomena more accurately. They can be linked with FORGE® to predict the industrial process used for the validation, which is an interesting future line of research.

7. REFERENCES

[1] S. J. Okullo, F. Reynès, and M. W. Hofkes, "Modelling Peak Oil and The Geological Constraints On Oil Production," *Resour. Energy Econ.*, vol. 40, pp. 36–56, 2015.

[2] Y. Kchaou, N. Haddar, G. Hénaff, V. Pelosin, and K. Elleuch, "Microstructural, compositional and mechanical investigation of Shielded Metal Arc Welding (SMAW) welded superaustenitic UNS N08028 (Alloy 28) stainless steel," *Mater. Des.*, vol. 63, pp. 278–285, 2014.

[3] Z. gang Song and E. xiang Pu, "Precipitated phases of superaustenitic stainless steel 654SMO," *J. Iron Steel Res. Int.*, vol. 24, no. 7, pp. 743–749, 2017.

[4] R. M. Forbes Jones and L. A. Jackman, "The structural evolution of superalloy ingots during hot working," *Jom*, vol. 51, no. 1, pp. 27–31, 2007.

[5] T. Anderson, "The influence of molybdenum on the microstructure of stainless steel welds," *Riv. Ital. della Saldatura*, vol. 58, no. 6, pp. 839–850, 2006.

[6] R. Wick, Charles; T.Benedict, John; F. Veilleux, "Chapter 15. Hot forging," in *Tool and manufacturing Engineers Handbook. Volume 2: Forming*, 1984.

[7] K. Lange, "Forging," in *Handbook of metal forming*, 1985, pp. 11.3-11.14.

[8] E. Pu, W. Zheng, J. Xiang, Z. Song, and J. Li, "Hot deformation characteristic and processing map of superaustenitic stainless steel S32654," *Mater. Sci. Eng. A*, vol. 598, pp. 174–182, 2014.

[9] E. Pu, M. Liu, W. Zheng, Z. Song, and Y. Miao, "Investigation on Behavior of Grain Growth in Superaustenitic Stainless Steel 654SMO," *J. Mater. Eng. Perform.*, vol. 24, no. 10, pp. 3897–3904, 2015.

[10] J. A. P.-S. Elorz, "Capítulo IX. Aceros de alta aleación (II): Austenoferríticos, Aceros maraging y especiales de alto niquel.," in *Aceros. Metalurgia física, selección y diseño*, Primera Ed., CIE Dossat 2000, 2004, pp. 505–506.

[11] J. A. P.-S. Elorz, "VIII.4 Los aceros inoxidables austeniticos," in *Aceros. Metalurgia física, selección y diseño*, 2004, pp. 446–447.

[12] N. Srinivasan, V. Kain, I. Samajdar, K. V. M. Krishna, and P. V. Sivaprasad, "Plane strain compression testing of Sanicro 28 by channel-die compression test: A direct microstructural observation," *Mater. Today Proc.*, vol. 4, no. 9, pp. 9888–9892, 2017.

[13] L. Wang and F. Liu, "Dynamic Recrystallization Behavior of N08028 Corrosion Resistant Alloy," *Mater. Sci. Forum*, vol. 788, pp. 396–405, 2014.

[14] A. Mirzaei, A. Zarei-Hanzaki, and H. R. Abedi, "Hot Ductility Characterization of Sanicro-28 Super-Austenitic Stainless Steel," *Metall. Mater. Trans. A Phys. Metall. Mater. Sci.*, vol. 47, no. 5, pp. 2037–2048, 2016.

[15] G. Varela-castro, "Critical Strain for Dynamic Recrystallisation . The particular case of steels," 2020.

[16] S. S. S. Kumar, T. Raghu, P. P. Bhattacharjee, G. A. Rao, and U. Borah, "Work hardening characteristics and microstructural evolution during hot deformation of a nickel superalloy at moderate strain rates," *J. Alloys Compd.*, vol. 709, pp. 394–409, 2017.

[17] F. J. Humphreys and M. Hatherly, "Chapter 2 The Deformed State," *Recryst. Relat. Annealing Phenom.*, no. July, pp. 13–80, 2004.

[18] M. Moallemi, A. Zarei-hanzaki, and A. Mirzaei, “On the Stacking Fault Energy Evaluation and Deformation Mechanism of Sanicro-28 Super-Austenitic Stainless,” *J. Mater. Eng. Perform.*, vol. 24, no. June, pp. 2335–2340, 2015.

[19] F. J. Humphreys and M. Hatherly, “Chapter 13 - Hot Deformation and Dynamic Restoration,” *Recryst. Relat. Annealing Phenom. (Second Ed.*, no. 1981, pp. 415–V, 2004.

[20] F. J. Humphreys and M. Hatherly, “Chapter 6 RECOVERY AFTER,” *Recryst. Relat. annealing Phenom.*, pp. 211–213, 1963.

[21] T. Sakai, A. Belyakov, R. Kaibyshev, H. Miura, and J. J. Jonas, “Dynamic and post-dynamic recrystallization under hot, cold and severe plastic deformation conditions,” *Prog. Mater. Sci.*, vol. 60, no. 1, pp. 130–207, 2014.

[22] F. J. Humphreys and M. Hatherly, “Chapter 7 - Recrystallization of Single-Phase Alloys,” *Recryst. Relat. Annealing Phenom. (Second Ed.*, pp. 215–IV, 2004.

[23] K. Huang and R. E. Logé, “A review of dynamic recrystallization phenomena in metallic materials,” *Mater. Des.*, vol. 111, pp. 548–574, 2016.

[24] P. A. Beck, “The Formation of Recrystallization Nuclei,” vol. 633, no. 1949, pp. 48–50, 2013.

[25] H. Search, C. Journals, A. Contact, and M. Iopscience, “A New Theory of Recrystallization Nuclei,” vol. 323, 1950.

[26] P. R. (EEIMVR) Rios, F. S. (CBMM) Jr, H. R. Z. (DEMAR) Sandim, U. Plaut, Ronal Lesley (Escola Politécnica, and U. Padilla, Angelo Fernando (Escola Politécnica, “Nucleation and growth during recrystallization,” *Mater. Res.*, vol. 8, no. 3, pp. 225–238, 2005.

[27] K. Huang, “Towards the modelling of recrystallization phenomena in multi-pass conditions : application to 304L steel Ke Huang To cite this version : École doctorale n ° 364 : Sciences Fondamentales et Appliquées l ’ École nationale supérieure des mines de Paris Spéc,” *Thesis*, 2012.

[28] A. Dehghan-manshadi and P. D. Hodgson, “Dynamic Recrystallization of Austenitic Stainless Steel under multiple peak flow behaviours,” vol. 47, no. 12, pp. 1799–1803, 2007.

[29] D. Le *et al.*, “Dynamic recrystallization in nickel and nickel-iron alloys during high temperature deformation,” vol. 17, no. August, 1969.

[30] T. Sakai and J. J. Jonas, “Dynamic Recrystallization: Mechanical and Microstructural Considerations,” *Acta Mater.*, vol. 32, no. 2, pp. 189–209, 1984.

[31] S. B. Brown, “An Internal Variable Constitutive Model For Hot Working Of Metals,” *Int. J. Miner. Metall. Mater.*, vol. 5, pp. 95–130, 1989.

[32] G. Gottstein, E. Brunger, M. Frommert, M. Goerdeler, and M. Zeng, “Prediction of the critical conditions for dynamic recrystallization in metals,” *Zeitschrift fuer Met. Res. Adv. Tech.*, vol. 94, no. 5, pp. 628–635, 2003.

[33] D. Ponge and G. Gottstein, “Necklace Formation During Dynamic Recrystallization: Mechanisms And Impact On Flow Behavior,” vol. 46, no. 1, pp. 69–80, 1998.

[34] M. S. Division and U. S. S. Corporation, “Onset of Recrystallization During the Tensile Deformation of Austenitic Iron at Intermediate Strain Rates - i,” vol. 6, no. June, pp. 1197–1203, 1975.

[35] E. I. Poliakt and J. J. Jonass, “A one parameter approach to determining the critical conditions for the initiation of dynamic recrystallization,” vol. 44, no. 1, pp. 127–136, 1996.

[36] H. Mirzadeh and A. Najafizadeh, “Prediction of the critical conditions for initiation of dynamic recrystallization,” *Mater. Des.*, vol. 31, no. 3, pp. 1174–1179, 2010.

[37] I. Weiss, T. Sakai, and J. J. Jonas, “Effect of test method on transition multiple to single peak dynamic recrystallization,” vol. 18, no. February, 1984.

[38] C. . Sellars, “Physical metallurgy of hotworking,” in *Hot working and Forming Processes*, 1980, pp. 3–15.

[39] C. Zener and J. H. Hollomon, “Effect of Strain Rate Upon Plastic Flow of Steel Contributed Original Research,” vol. 22, 1944.

[40] A. Laasraoui and J. J. Jonas, “Prediction of Steel Flow Stresses at High Temperatures and Strain Rates,” vol. 22, no. July, 1991.

[41] M. Bambach, “Implications from the Poliak-Jonas criterion for the construction of flow stress models incorporating dynamic recrystallization,” *Acta Mater.*, vol. 61, no. 16, pp. 6222–6233, 2013.

[42] C. H.J McQueen, N.D. Ryan (Mechanical Engineering, Concordia University, Montreal, “constitutive analysis in hot working,” *Mater. Sci. Emgineering*, vol. 322, no. 1–2, pp. 43–63, 2002.

[43] G. R. Stewart, J. J. Jonas, and F. Montheillet, “Kinetics and critical conditions for the initiation of dynamic recrystallization in 304 stainless steel,” *ISIJ Int.*, vol. 44, no. 9, pp. 1581–1589, 2004.

[44] E. I. Poliak and J. J. Jonas, “Initiation of Dynamic Recrystallization in Constant Strain Rate,” vol. 43, no. 5, pp. 684–691, 2003.

[45] E. W. Hart, “A phenomenological theory for plastic deformation of polycrystalline metals,” *Acta Metall.*, vol. 18, no. 6, pp. 599–610, 1970.

[46] E. I. Poliak and J. J. Jonas, “Critical Strain for Dynamic Recrystallization in Variable Strain,” vol. 43, no. 5, pp. 692–700, 2003.

[47] M. R. Barnett *et al.*, “Predicting the Critical Stress for Initiation of Dynamic Recrystallization,” vol. 46, no. 11, pp. 1679–1684, 2006.

[48] M. Imran, M. Kühbach, F. Roters, and M. Bambach, “Development of a model for dynamic recrystallization consistent with the second derivative criterion,” *Materials (Basel).*, vol. 10, no. 11, p. 1259, 2017.

[49] J. J. Jonas, C. Ghosh, X. Quelennec, and V. V Basabe, “The Critical Strain for Dynamic Transformation in Hot Deformed Austenite,” vol. 53, no. 1, pp. 145–151, 2013.

[50] X. Quelennec and J. J. Jonas, “Simulation of Austenite Flow Curves under Industrial Rolling Conditions Using a Physical Dynamic Recrystallization Model,” vol. 52, no. 6, pp. 1145–1152, 2012.

[51] J. J. Jonas, X. Quelennec, L. Jiang, and É. Martin, “The Avrami kinetics of dynamic recrystallization,” *Acta Mater.*, vol. 57, no. 9, pp. 2748–2756, 2009.

[52] J. Lohmar and M. Bambach, “Influence of Different Interpolation Techniques on the Determination of the Critical Conditions for the Onset of Dynamic Recrystallisation,” vol. 762, pp. 331–336, 2013.

[53] R. A. Petkovic, M. J. Luton, and J. J. Jonas, “Recovery and recrystallization of carbon steel between intervals of hot working,” vol. 14, no. 2, pp. 137–145, 1975.

[54] J. . Sah, G. . Richardson, and C. . Sellars, “Grain-Size effect during dynamic recrystallization of Nickel.,” *Met. Sci*, vol. 8, pp. 325–331, 1974.

[55] M. El Wahabi, “Effect of initial grain size on dynamic recrystallization in high purity austenitic stainless steels,” vol. 53, pp. 4605–4612, 2005.

[56] P. D. Hodgson, “Dependency of Recrystallization Mechanism to the Initial Grain Size,” pp. 23–25, 2008.

[57] M. Ohashi, T. Endo, and T. Sakai, “Effect of initial grain size on dynamic recrystallization of pure nickel,” *J.Japan Inst. Met.*, vol. 54, no. 4, pp. 435–441, 1990.

[58] M. C. Mataya, E. R. Nilsson, E. L. Brown, and G. Krauss, “Hot Working and Recrystallization of As-Cast 316L,” vol. 34, no. August, 2003.

[59] M. C. Mataya, E. R. Nilsson, E. L. Brown, and G. Krauss, “Hot Working and Recrystallization of As-Cast 317L,” vol. 34, no. December, pp. 3021–3041, 2003.

[60] G. K. Mandal, N. Stanford, P. Hodgson, and J. H. Beynon, “Effect of hot working on dynamic recrystallisation study of as-cast austenitic stainless steel,” *Mater. Sci. Eng. A*, vol. 556, pp. 685–695, 2012.

[61] C. Huiqin, H. Wenwu, Z. Xiaodong, Q. Fengming, and W. Zhenxing, “Hot deformation behavior and dynamic recrystallization of Mn18Cr18N steel with as-cast versus wrought starting structures,” *Procedia Eng.*, vol. 207, pp. 1779–1784, 2017.

[62] N. Fujita, R. Sahara, T. Narushima, and C. Ouchi, “Austenitic grain growth behavior immediately after dynamic recrystallization in HSLA steels and austenitic stainless steel.,” *ISIJ Int.*, vol. V48, pp. 1419–1428, 2008.

[63] T. Sakai, Y. Nagao, M. Ohashi, and J. J. Jonas, “Flow stress and substructural change during transient dynamic recrystallization of nickel Flow stress and substructural change during transient dynamic recrystallization of nickel,” vol. 0836, no. May, 2016.

[64] F. Drx and C. Engineering, “Dislocation substructures developed during dynamic recrystallisation in polycrystalline nickel,” vol. 6, no. December, 1990.

[65] B. Derby, “The Dependence of Grain Size on Stress During Dynamic Recrystallization,” vol. 39, no. 5, pp. 955–962, 1991.

[66] N. . Switzner, C. . Van Tyne, and M. . Mataya, “Effect of forging strain rate and deformation temperature on the mechanical properties of warm-worked 304L stainless steel,” *J. Mater. Process. Technol.*, 2000.

[67] Y. C. Lin and X. Chen, “A critical review of experimental results and constitutive descriptions for metals and alloys in hot working,” *Mater. Des.*, vol. 32, no. 4, pp. 1733–1759, 2011.

[68] C. W. Johnson GR, “A constitutive model and data for metals subjected to large strains, high strains rates and high temperatures,” in *Proceedings of the 7th International Symposium on Ballistics*, 1983, pp. 543–3.

[69] B. W. Fields DS, “Determination of strain hardening characteristics by torsion testing,” *Proc Am Soc Test Mater*, vol. 57, pp. 1259–72, 1957.

[70] R. Liang and A. S. Khan, “A critical review of experimental results and constitutive models for BCC and FCC metals over a wide range of strain rates and temperatures,” vol. 15, pp. 963–980, 1999.

[71] Y. Q. Cheng, H. Zhang, Z. H. Chen, and K. F. Xian, “Flow stress equation of AZ31 magnesium alloy sheet during warm tensile deformation,” *J. Mater. Process. Technol.*, vol. 208, no. 1–3, pp. 29–34, 2008.

[72] Q. Guo-zheng, L. I. U. Ke-wei, Z. Jie, and C. Bin, “Dynamic softening behaviors of 7075 aluminum alloy,” *Trans. Nonferrous Met. Soc. China*, vol. 19, no. August, pp. s537–s541, 2009.

[73] J. Mclaren, C. M. Sellars, R. Shahani, and R. Bolingbroke, “Constitutive equations for high temperature flow stress of aluminium alloys,” vol. 13, no. March, pp. 210–216, 1997.

[74] Y. C. Lin, M. S. Chen, and J. Zhong, “Constitutive modeling for elevated temperature flow behavior of 42CrMo steel,” *Comput. Mater. Sci.*, vol. 42, no. 3, pp. 470–477, 2008.

[75] Y. . Lin, M.-S. Chen, and J. Zhong, “Effect of temperature and strain rate on the compressive deformation behavior of 42CrMo Steel,” *J. Mater. Process. Technol.*, vol. 205, no. 1–3, pp. 308–315, 2008.

[76] A. Momeni and K. Dehghani, “Characterization of hot deformation behavior of 410 martensitic stainless steel using constitutive equations and processing maps,” *Mater. Sci. Eng. A*, vol. 527, no. 21–22, pp. 5467–5473, 2010.

[77] S. Mandal, V. Rakesh, P. V. Sivaprasad, S. Venugopal, and K. V. Kasiviswanathan, “Constitutive equations to predict high temperature flow stress in a Ti-modified austenitic stainless steel,” *Mater. Sci. Eng. A*, vol. 500, no. 1–2, pp. 114–121, 2009.

[78] D. Samantaray, S. Mandal, and A. K. Bhaduri, “Constitutive analysis to predict high-temperature flow stress in modified 9Cr-1Mo (P91) Steel,” *Mater. Des.*, vol. 31, no. 2, pp. 981–984, 2010.

[79] Transvalor, “Part 8 : Metallurgy Table of Contents : On the modelling scope for FORGE.”

[80] A. Hensel and T. Spittel, *Kraft-und Arbeitsbedarf bildsamer Formgebungsverfahren*, 1 st. Leipzig: VEB Deutscher Verlag fur Grundstoffindustrie, 1978.

[81] H. Deformation *et al.*, “Constitutive Equations for Describing the Warm and Hot deformation behaviour of 20Cr2Ni4A.”

[82] Y. C. Lin and Q. Wu, “Hot tensile deformation mechanism and dynamic softening behavior of Ti - 6Al - 4V alloy with thick lamellar microstructures.”

[83] Y. Bergstrom, “A dislocation model for the stress-strain behaviour of polycrystalline alpha-Fe with special emphasis on the variation of the desities of mobile and inmobile dislocations,” *Master Sci Eng A*, vol. 426, pp. 101–13, 2006.

[84] Honeycombe, *Steels microstructure and properties*. 1981.

[85] C. Sellars, *On the mechanism of hot deformation*. 1966.

[86] Y. C. Lin, M. Chen, and J. Zhong, “Prediction of 42CrMo steel flow stress at high temperature and strain rate,” vol. 35, pp. 142–150, 2008.

[87] J. Liu, Z. Cui, and C. Li, “Modelling of flow stress characterizing dynamic recrystallization for magnesium alloy AZ31B,” vol. 41, pp. 375–382, 2008.

[88] R. Cahn, *Physical metallurgy*. Amsterdam: North Holland Publishing Company, 1965.

[89] J. J. Jonas, C. . Sellars, and M. Tegart, “Strength and structure under hot-working conditions.,” *Metall. Rev.*, vol. 130, pp. 1–33, 1969.

[90] W. C. Hahn, R. A. P. Djaic, J. J. Jonas, and R. A. P. Djaic, “Recrystallization of High Carbon Steel Between Intervals of High Temperature Deformation,” vol. 4, no. February, pp. 4–7, 1973.

[91] R. Djaic and J. J. Jonas, “Static Recrystallization of Austenite Between Intervals of Hot Working,” *J. iron Steel Inst.*, vol. 210, no. APR, pp. 256-, 1972.

[92] R. A. Petkovic, M. J. Luton, and J. J. Jonas, “Recovery And Recrystallization Of Polycrystalline Copper After Hot Working,” *Acta Metall.*, vol. 27, pp. 1633–1648, 1979.

[93] M. J. Luton, R. A. Petkovic, and J. J. Jonas, “Kinetics Of Recovery And Recrystallization In Polycrystalline Copper,” *Acta Metall.*, vol. 28, pp. 729–743, 1979.

[94] “Kinetics of recovery and recrystallization in Dynamically recrystallized Austenite.pdf.” .

[95] P. D. Hodgson and R. K. Gibbs, “A Mathematical Model to Predict the Mechanical Properties of Hot Rolled C-Mn and Microalloyed Steels,” *ISIJ Int.*, vol. 32, no. 12, pp. 329–338, 1992.

[96] C. Roucoules, P. D. Hodgson, S. Yue, and J. J. Jonas, “Softening and Microstructural Change Following the Dynamic Recrystallization of Austenite,” vol. 25, no. February, 1994.

[97] P. D. Hodgson, “Post-dynamic recrystallization after multiple peak dynamic recrystallisation in C-Mn steels,” vol. 11, no. June, pp. 548–556, 1995.

[98] H. Beladi, P. Cizek, and P. D. Hodgson, “The mechanism of metadynamic softening in austenite after complete dynamic recrystallization,” *Scr. Mater.*, vol. 62, no. 4, pp. 191–194, 2010.

[99] H. Beladi, P. Cizek, and P. D. Hodgson, “New insight into the mechanism of metadynamic softening in austenite,” *Acta Mater.*, vol. 59, no. 4, pp. 1482–1492, 2011.

[100] A. D. I. Schino and J. M. Kenny, “Analysis of the recrystallization and grain growth processes in AISI 316 stainless steel,” vol. 7, pp. 5291–5298, 2002.

[101] C. Roucoules, C (Mc Gill University, Montreal, “Dynamic and metadynamic recrystallization in HSLA steels,” 1992.

[102] H. J. Mcqueen, “Static Recrystallization of Tool Steels,” vol. 543, pp. 4458–4463, 2007.

[103] H. . McAqeen, S. Yue, N. . Ryan, and E. Fry, “Hot working characteristics of steels in austenitic state,” *J. Mater. Process. Technol.*, vol. 53, no. 1–2, pp. 293–310, 1995.

[104] C. Sellars, “Deformation, processing, and structures,” in *ASM Materials Science Seminar*, 1982, pp. 245–257.

[105] A. R. Morgridge, “Metadynamic recrystallization in C steels,” vol. 25, no. 4, pp. 291–299, 2002.

[106] A. Dehghan-manshadi, M. R. Barnett, and P. D. Hodgson, “Recrystallization in AISI 304 austenitic stainless steel during and after hot deformation,” vol. 485, pp. 664–672, 2008.

[107] S. Cho, “Hot rolling simulations of austenitic stainless steel,” vol. 6, pp. 4267–4272, 2001.

[108] L. Slaz, T. Sakai, and J. J. Jonas, “Effect of initial grain size on dynamic recrystallization of copper,” vol. 17, no. December, pp. 609–616, 1983.

[109] D. Barraclough and C. Sellars, “Static recrystallization and restauration after hot deformation of type 304 stainless steel,” *Mater. Sci. Emgineering*, vol. 13, pp. 257–267, 1979.

[110] C. M. Sellars, “The kinetics of softening processes during hot working of austenite,” no. 2, pp. 239–248, 1985.

[111] Y. C. Lin and M. S. Chen, “Study of microstructural evolution during static recrystallization in a low alloy steel,” *J. Mater. Sci.*, vol. 44, no. 3, pp. 835–842, 2009.

[112] H. Mirzadeh, J. M. Cabrera, A. Najafizadeh, and P. R. Calvillo, “EBSD study of a hot deformed austenitic stainless steel,” *Mater. Sci. Eng. A*, vol. 538, pp. 236–245, 2012.

[113] J. Smith, William F; Hashemii, “Solidificación de metales,” in *Fundamentos de la cienci ae ingeniería de materiales.*, 2007, pp. 132–133.

[114] R. Kapoor, J. B. Singh, and J. K. Chakravartty, “High strain rate behaviour of ultrafine-grained Al-1.5 Mg,” *Mater. Sci. Eng. A*, vol. 496, no. 1–2, pp. 308–315, 2008.

[115] R. Kapoor and S. I. A. Nemat-Nasser, “Comparison between high and low strain-rate deformation of tantalum,” *Metall. Mater. Trans. A Phys. Metall. Mater. Sci.*, vol. 31, no. 3, pp. 815–823, 2000.

[116] B. Roebuck, J. D. Lord, M. Brooks, M. S. Loveday, C. M. Sellars, and R. W. Evans, “Measurement of flow stress in hot axisymmetric compression tests,” vol. 23, no. 2, pp. 59–83.

[117] R. Ebrahimi and A. Najafizadeh, “A new method for evaluation of friction in bulk metal forming,” vol. 152, no. January 2003, pp. 136–143, 2004.

[118] L. Wang, F. Liu, Q. Zuo, and C. F. Chen, “Prediction of flow stress for N08028 alloy under hot working conditions,” *Mater. Des.*, vol. 47, pp. 737–745, 2013.

[119] N. P. Opolska, “Cyclic Stress-Strain Response of Metals and Alloys Modelling on a Microstructural Basis,” vol. 2, pp. 53–72, 2005.

APPENDIX A: INITIATION OF DRX

The corrected curves and their corresponding Poliak-Jonas approach are shown in Appendix A. The calculated $(\sigma_c, \varepsilon_c)$ and $(\sigma_p, \varepsilon_p)$ Are indicated, and the calculation method is explained in the Strains hardening vs stress graphic.

The appearance of inconsistencies with the second derivate criterium has to be mentioned, as reviewed in Chapter 2.

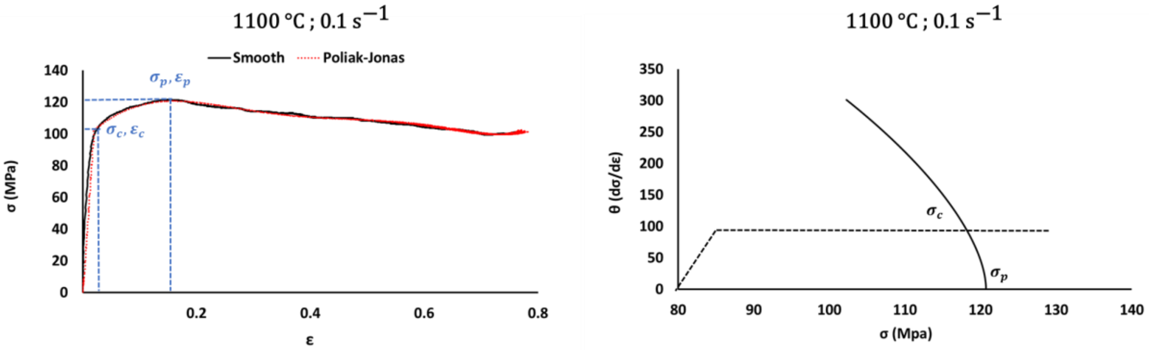

Figure A- 1. Corrected vs P-J approach Stress-Strain curve and the corresponding Strains hardening rate vs Stress for 1100 °C and 0.1 s^{-1}.

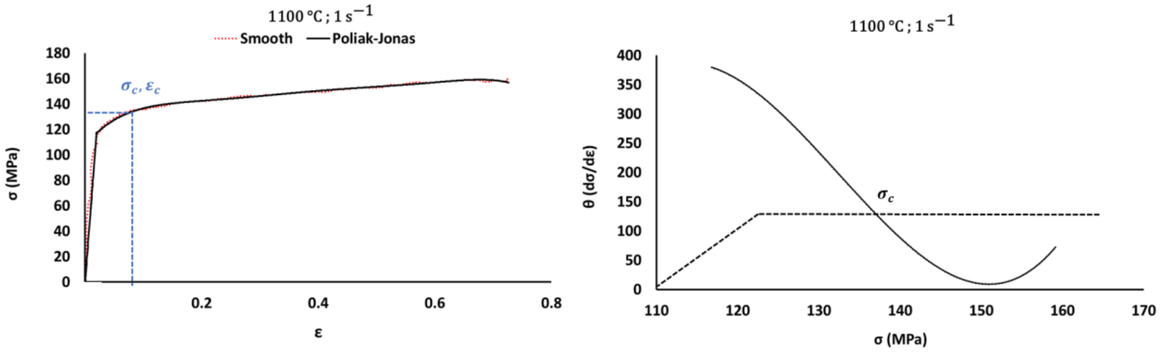

Figure A- 2. Corrected vs P-J approach Stress-Strain curve and the corresponding Strains hardening rate vs Stress for 1100 °C and 1 s^{-1}.

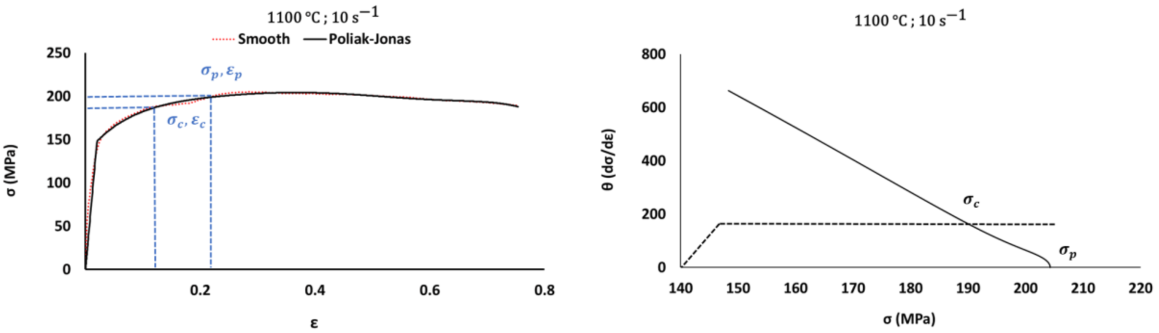

Figure A- 3. Corrected vs P-J approach Stress-Strain curve and the corresponding Strains hardening rate vs Stress for 1100 °C and 10 s^{-1}.

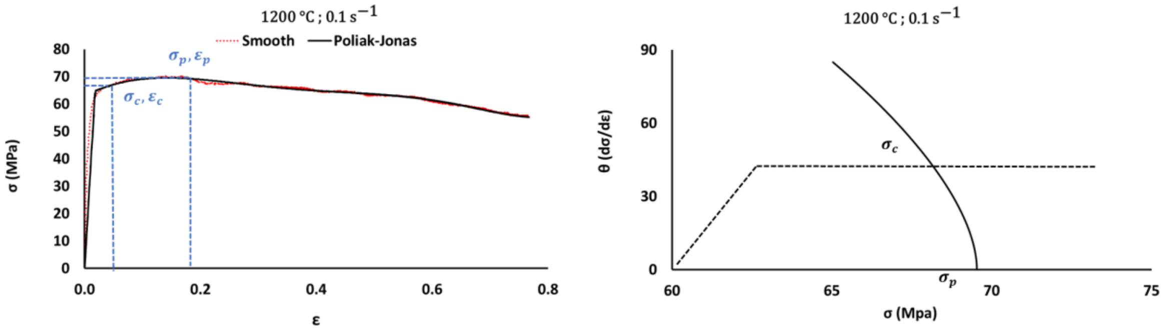

Figure A- 4. Corrected vs P-J approach Stress-Strain curve and the corresponding Strains hardening rate vs Stress for 1200 °C and 0.1 s^{-1}.

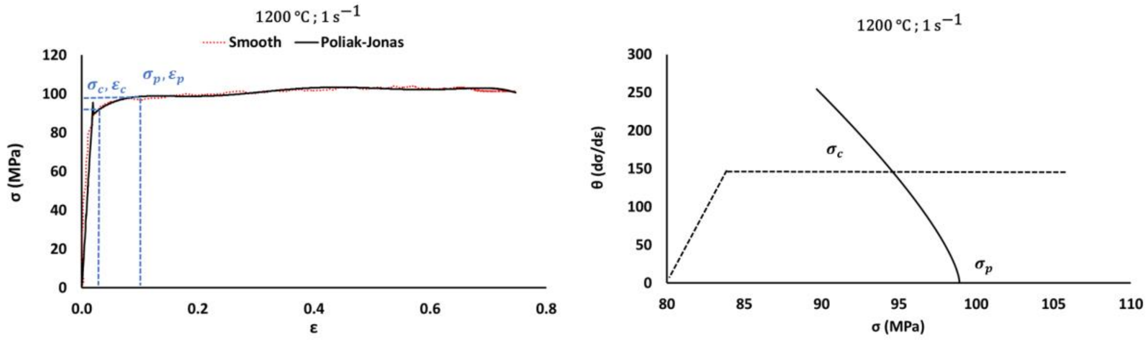

Figure A- 5. Corrected vs P-J approach Stress-Strain curve and the corresponding Strains hardening rate vs Stress for 1200 °C and 1 s^{-1}.

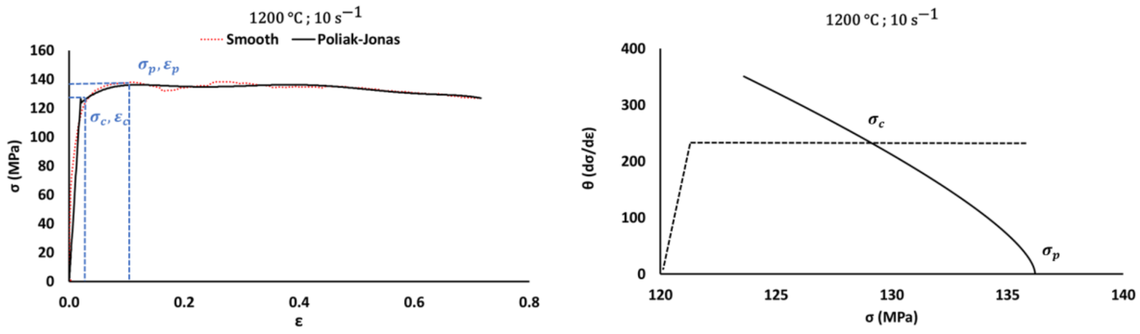

Figure A- 6. Corrected vs P-J approach Stress-Strain curve and the corresponding Strains hardening rate vs Stress for 1200 °C and 10 s^{-1}.

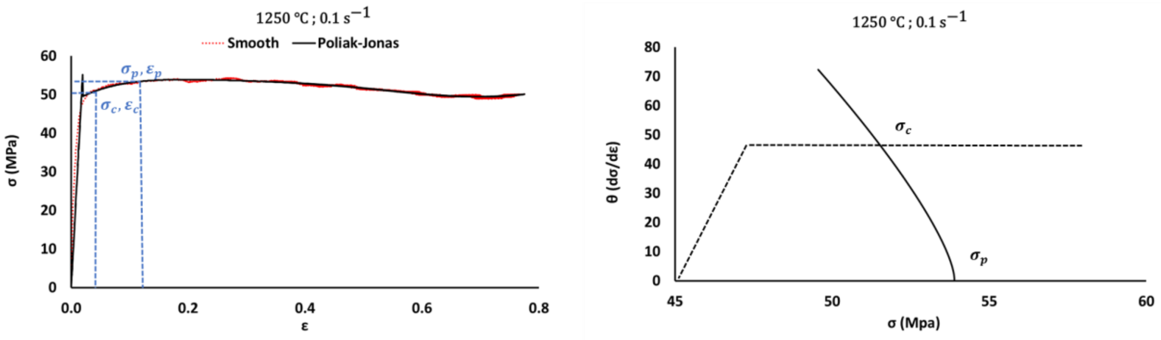

Figure A- 7. Corrected vs P-J approach Stress-Strain curve and the corresponding Strains hardening rate vs Stress for 1250 °C and 0.1 s^{-1}.

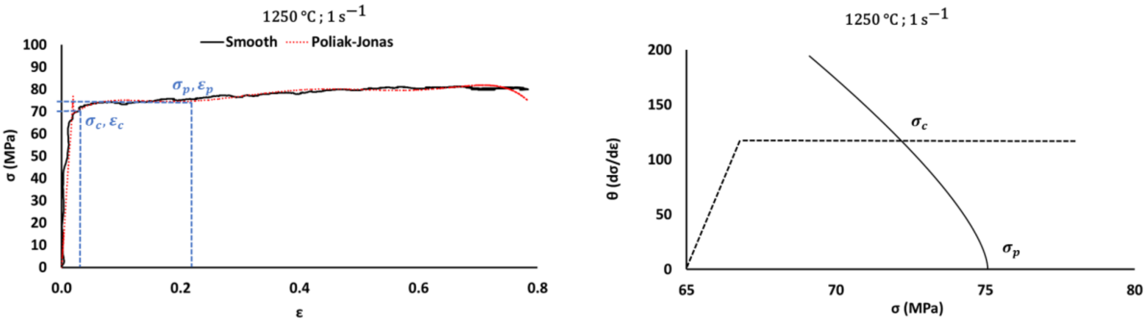

Figure A- 8. Corrected vs P-J approach Stress-Strain curve and the corresponding Strains hardening rate vs Stress for 1250 °C and 1 s^{-1}.

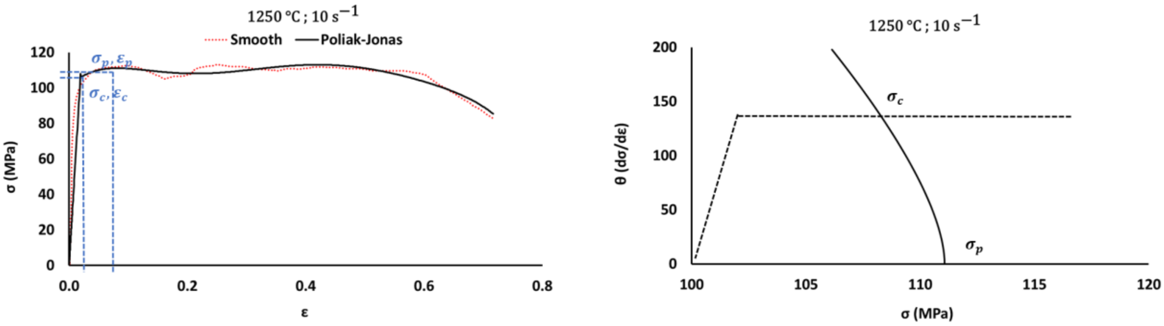

Figure A- 9. Corrected vs P-J approach Stress-Strain curve and the corresponding Strains hardening rate vs Stress for 1250 °C and 10 s^{-1}.

APPENDIX B: EBSD ANALYSIS

In this Appendix, a selection of the Images obtained by EBSD is shown. The scale used for this summary is 200 μm for a step size of 0.5694 at a different gain, which depends on the sample's preparation.

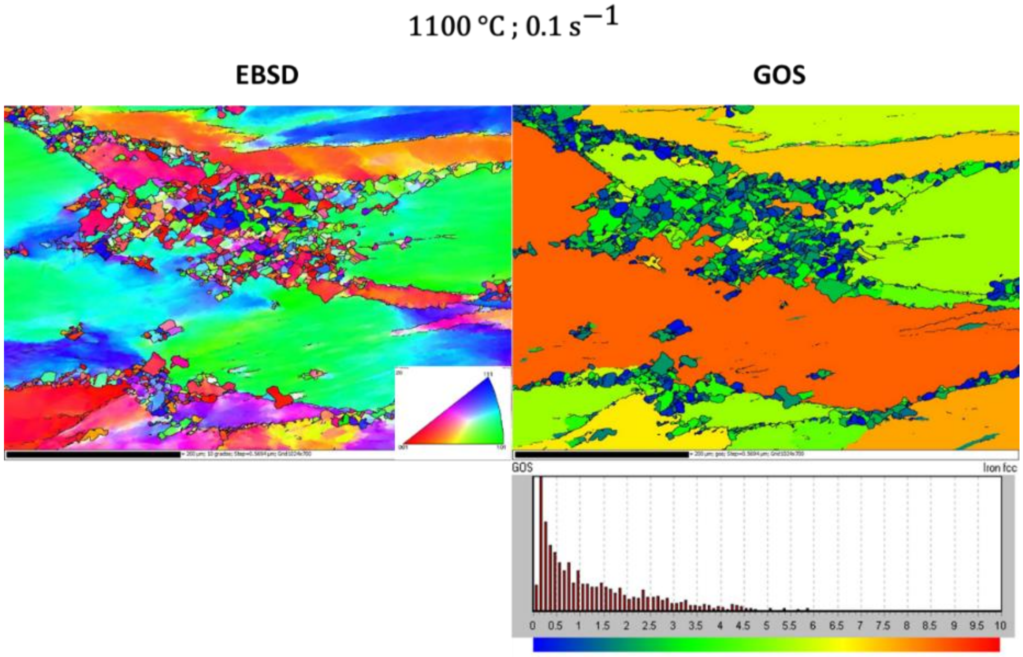

$1100\,°C\,;\,0.1\,s^{-1}$

EBSD

GOS

Figure B- 1. EBSD map and GOS Map for 1100 ºC and 0.1 s^-1^.

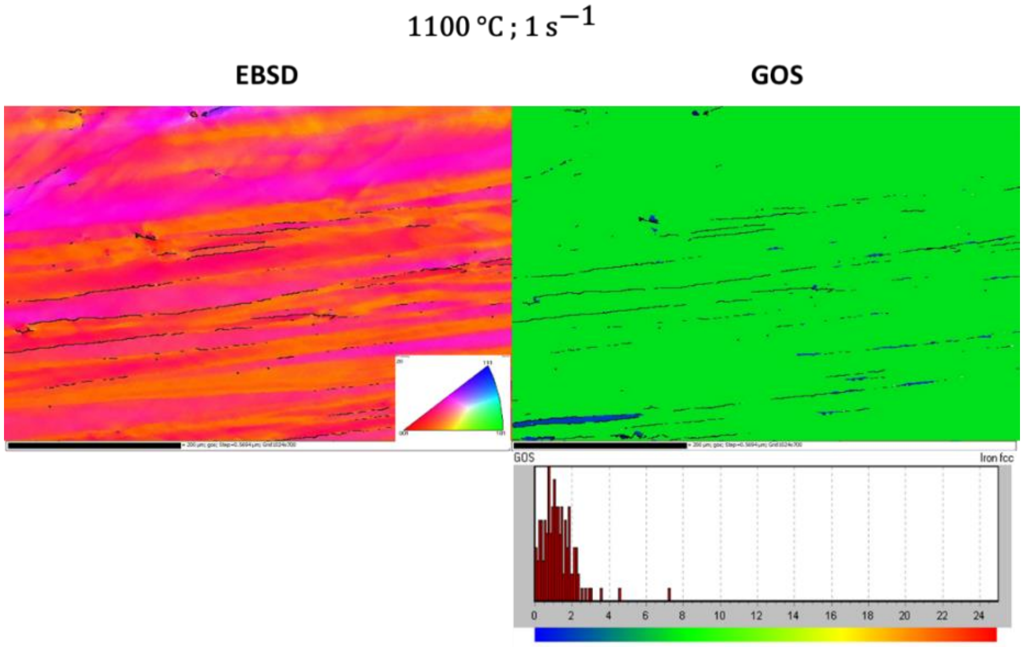

$1100\,°C\,;\,1\,s^{-1}$

EBSD

GOS

Figure B- 2. EBSD map and GOS Map for 1100 ºC and 1 s^{-1}.

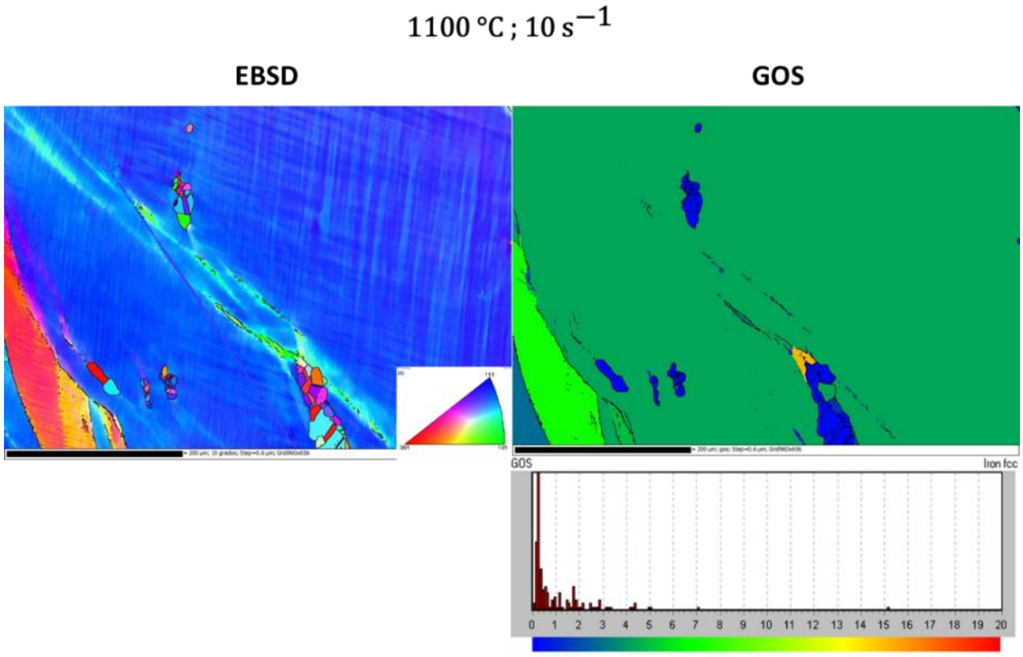

Figure B- 3. EBSD map and GOS Map for 1100 ºC and 10 s^{-1}.

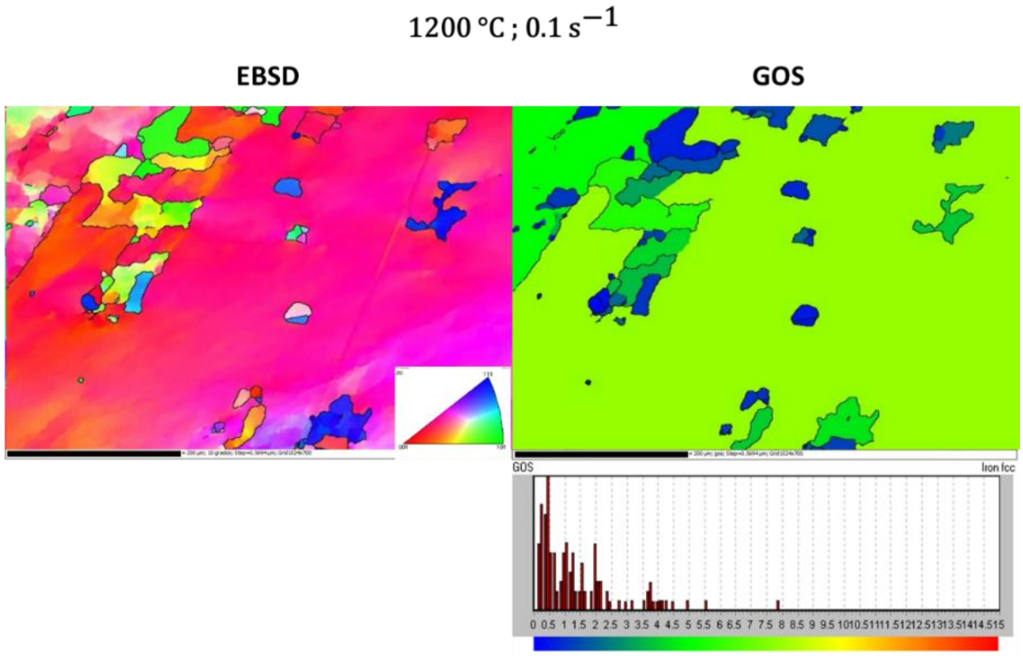

Figure B- 4. EBSD map and GOS Map for 1200 ºC and 0.1 s^{-1}.

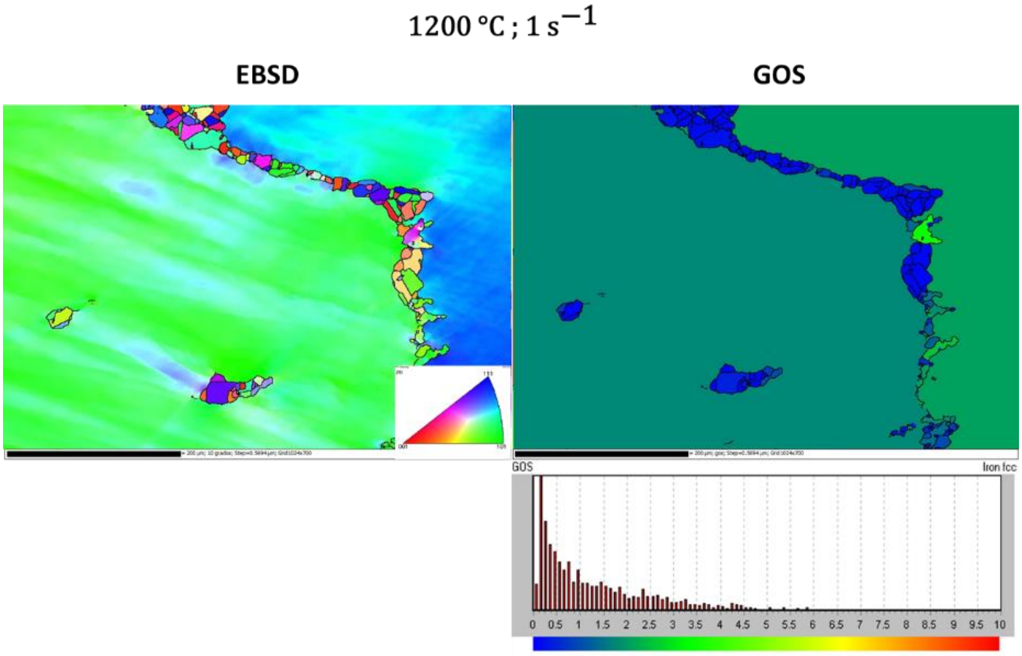

Figure B- 5. EBSD map and GOS Map for 1200 °C and 1 s^{-1}.

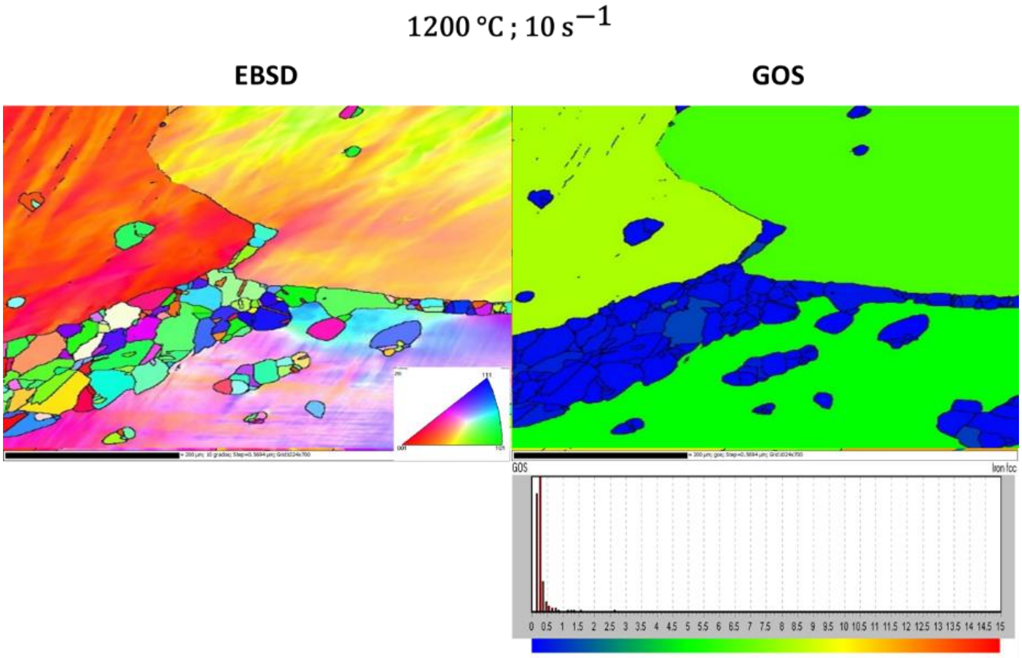

Figure B- 6. EBSD map and GOS Map for 1200 °C and 10 s^{-1}.

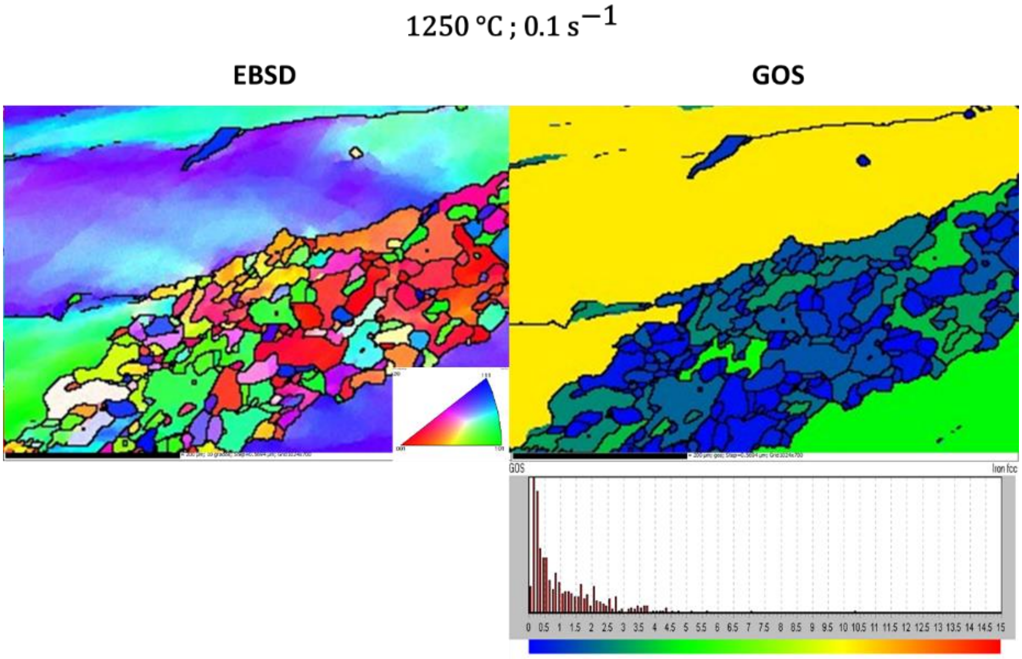

Figure B- 7. EBSD map and GOS Map for 1250 °C and 0.1 s^{-1}.

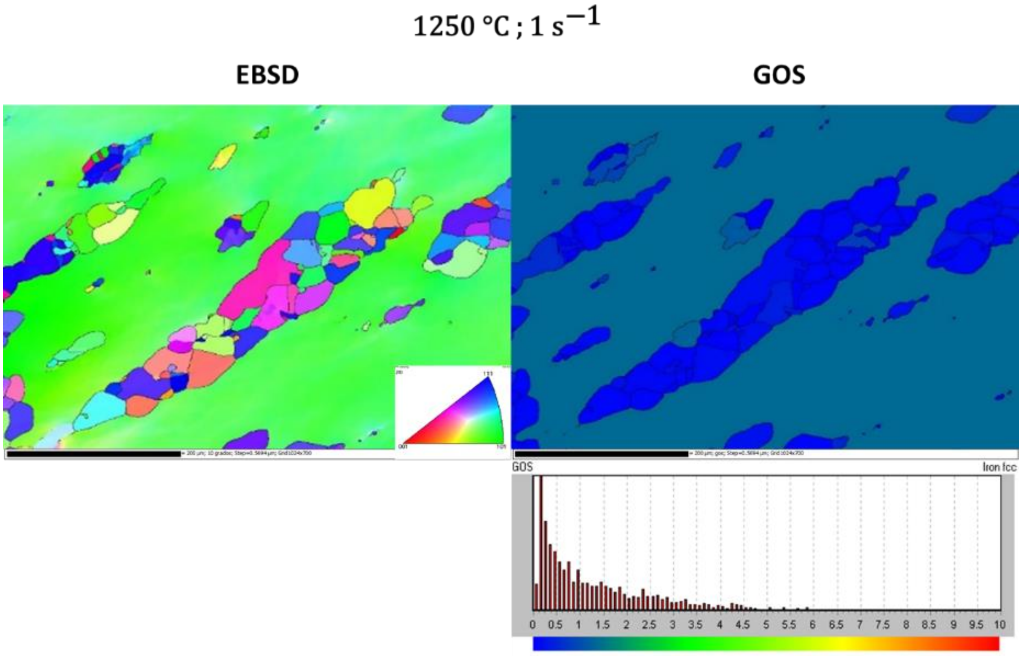

Figure B- 8. EBSD map and GOS Map for 1250 °C and 1 s^{-1}.

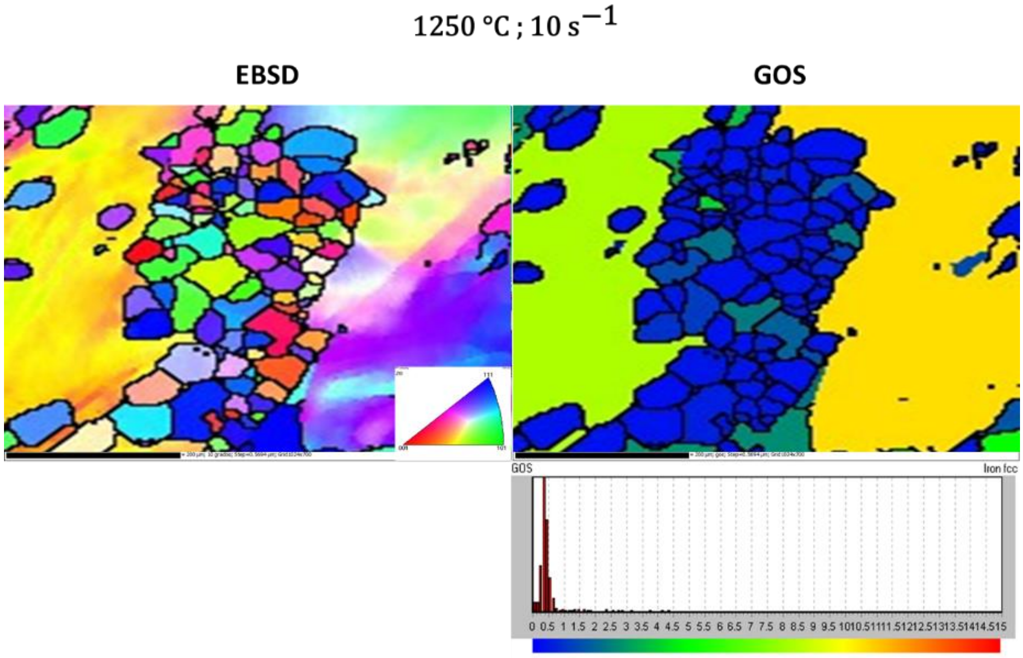

Figure B- 9. EBSD map and GOS Map for 1250 ºC and 10 s^{-1}.

APPENDIX C: HANSEL-SPITTEL APPROACH

The hansel-Spittel model for the initiation of recrystallization is obtained in the following graphics.

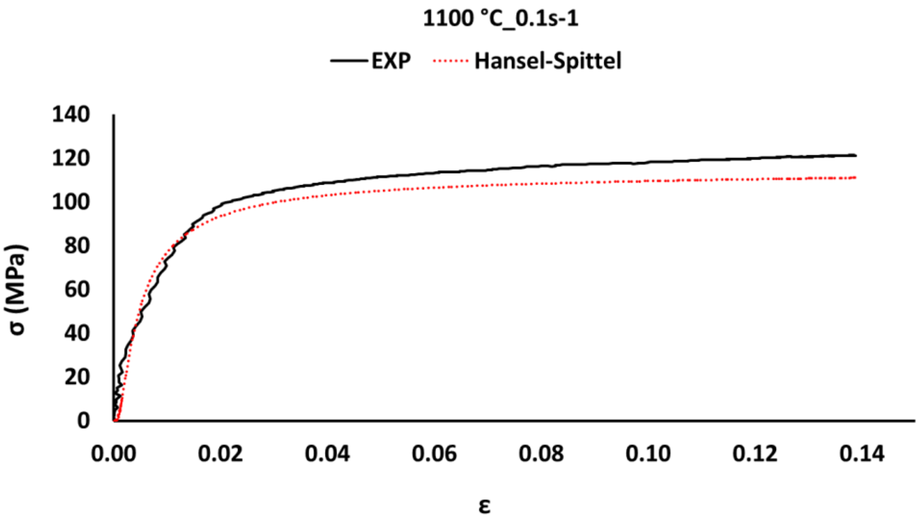

Figure C- 1. H-S approach for the initiation of DRX Stress-Strain curve for 1100 ºC and 0.1 s^{-1}.

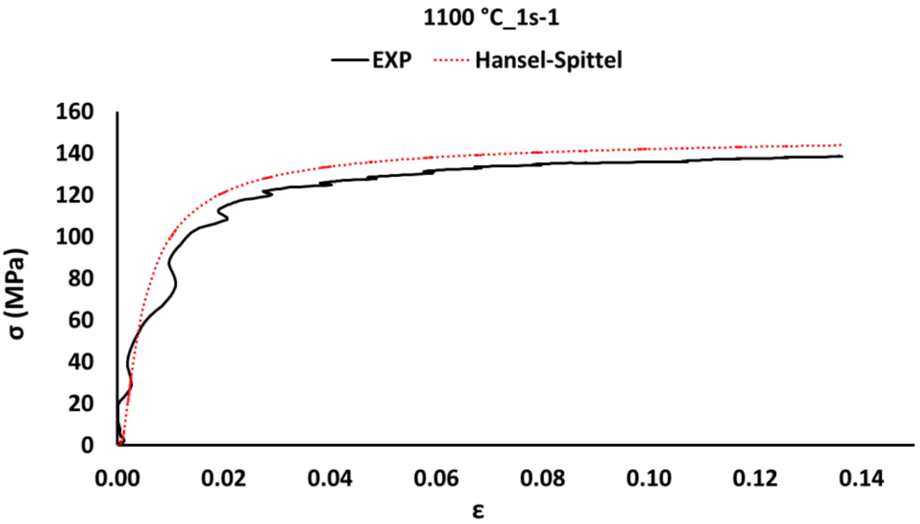

Figure C- 2. H-S approach for the initiation of DRX Stress-Strain curve for 1100 ºC and 1 s^{-1}.

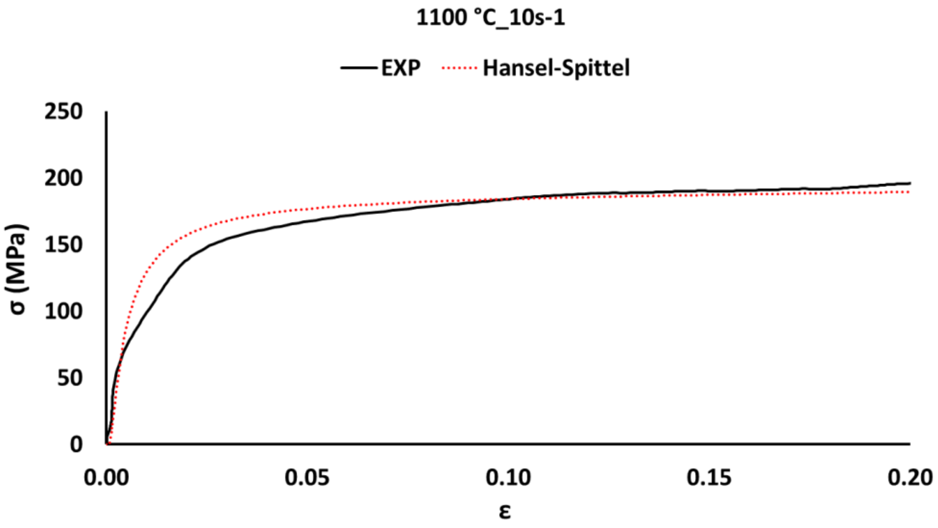

Figure C- 3. H-S approach for the initiation of DRX Stress-Strain curve for 1100 °C and 10 s^{-1}.

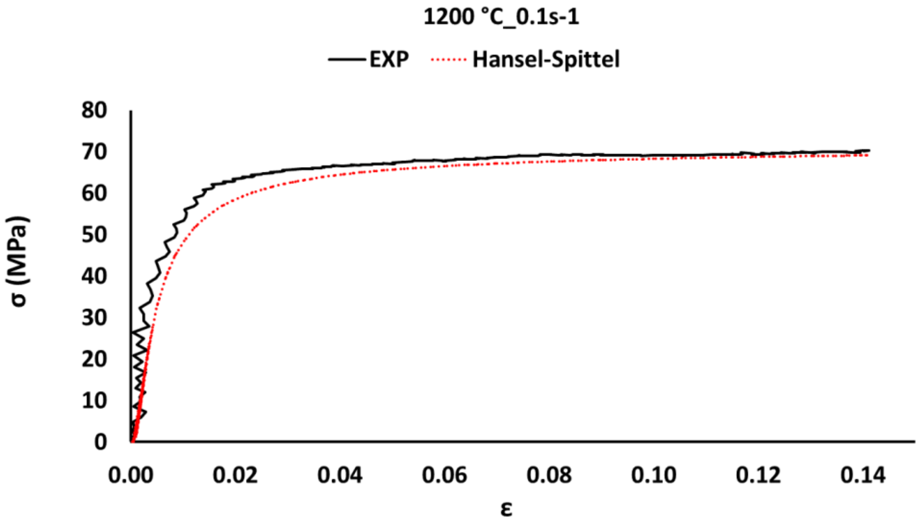

Figure C- 4. H-S approach for the initiation of DRX Stress-Strain curve for 1200 °C and 0.1 s^{-1}.

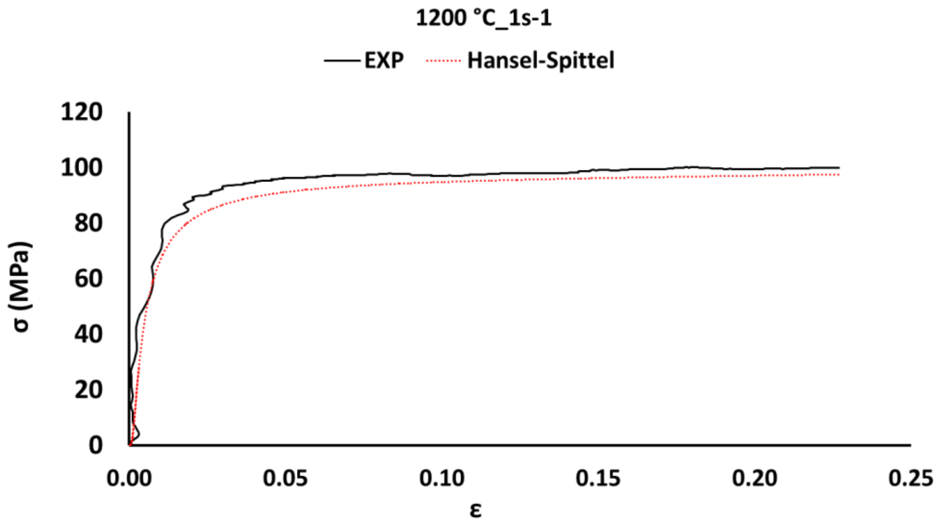

Figure C- 5. H-S approach for the initiation of DRX Stress-Strain curve for 1200 °C and 1 s^{-1}.

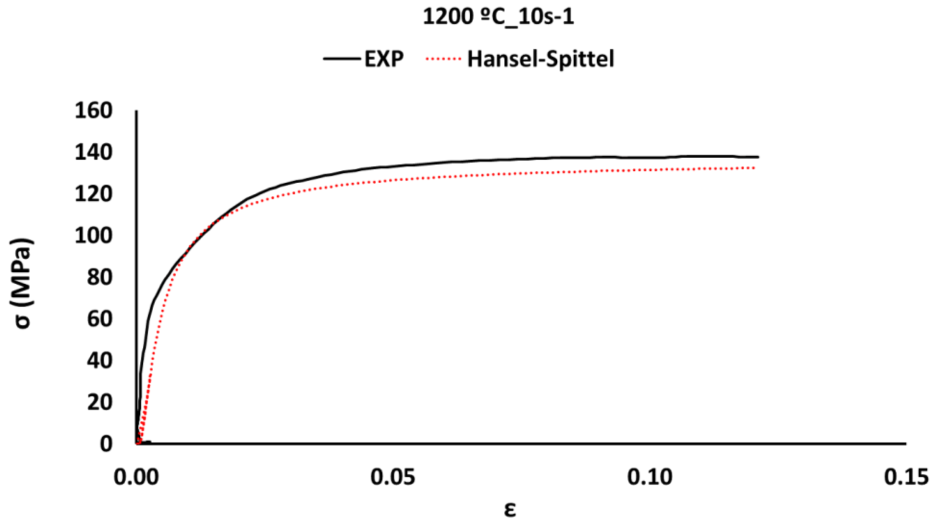

Figure C- 6. H-S approach for the initiation of DRX Stress-Strain curve for 1200 °C and 1 s^{-1}.

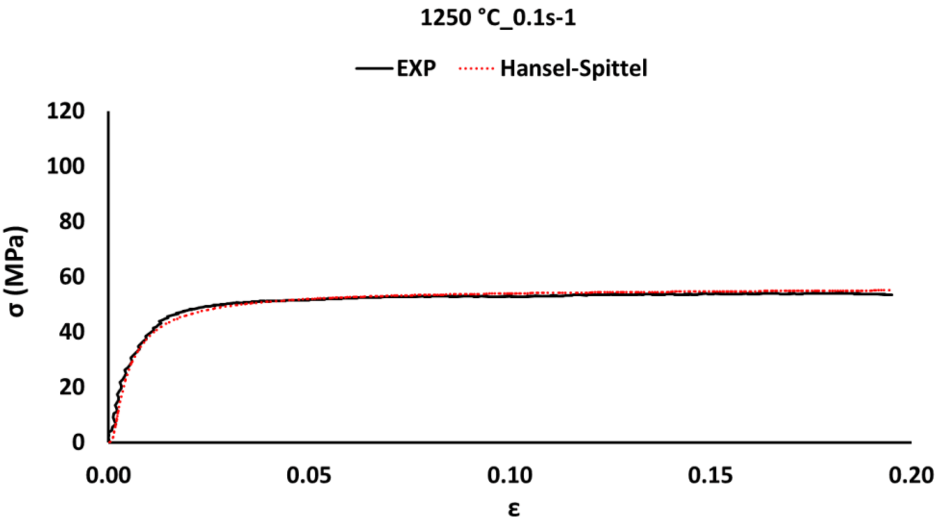

Figure C- 7. H-S approach for the initiation of DRX Stress-Strain curve for 1200 °C and 1 s^{-1}.

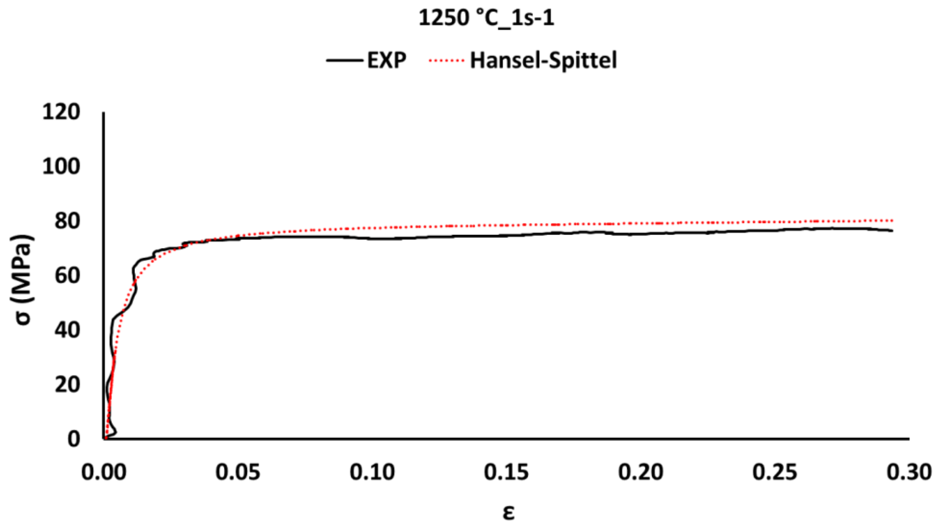

Figure C- 8. H-S approach for the initiation of DRX Stress-Strain curve for 1200 °C and 1 s^{-1}.

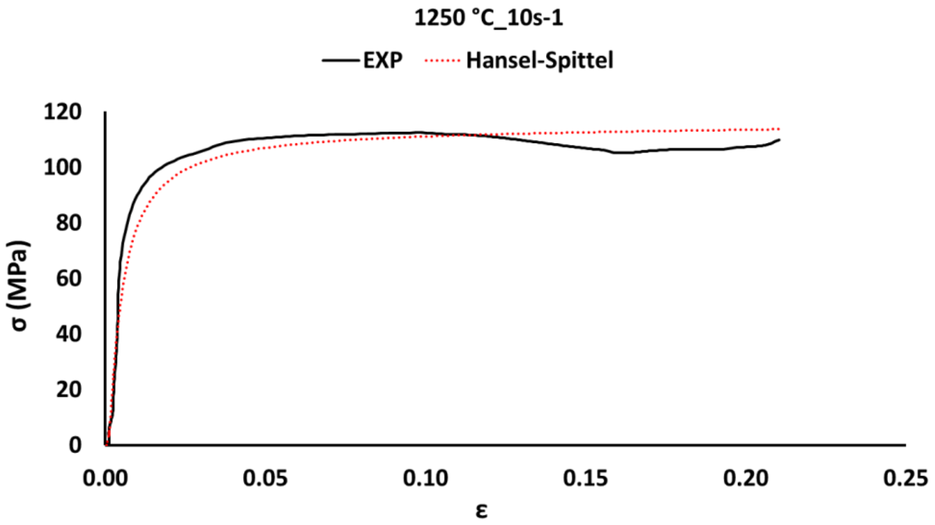

Figure C- 9. H-S approach for the initiation of DRX Stress-Strain curve for 1200 ºC and 1 s^{-1}.